**Title**
Methods for Human Brain Metabolic Imaging using Hyperpolarized [2-13C]Pyruvate

**Author**
Chung, Brian Thomas

**Publication Date**
2021

Peer reviewed|Thesis/dissertation

# Methods for Human Brain Metabolic Imaging using Hyperpolarized [2-13C]Pyruvate

by
Brian Chung

DISSERTATION
Submitted in partial satisfaction of the requirements for degree of
DOCTOR OF PHILOSOPHY

in

Bioengineering

in the

GRADUATE DIVISION

of the

UNIVERSITY OF CALIFORNIA, SAN FRANCISCO
AND
UNIVERSITY OF CALIFORNIA, BERKELEY

Approved:

DocuSigned by:
Daniel B. Vi
DA5485F9C42341E...
Daniel Vigneron
Chair

DocuSigned by:
John Kurhanewicz
[illegible]498...
John Kurhanewicz

DocuSigned by:
Robert Bok
[illegible]481...
Robert Bok

DocuSigned by:
1644A2CD853841E...
Peder Larson

Committee Members

For my brother Spencer

# Acknowledgements

Thanks with all my brain to every human without whom this accomplishment would not exist. First I would like to thank my advisor, mentor, and friend Professor Daniel B. Vigneron, and lab researchers: Drs. Jeremy Gordon, Hsin-Yu Chen, Eugene Milshteyn, Zihan Zhu, Yaewon Kim, Adam Autry, Dave Korenchan, Natalie Korn, Jinny Sun, and graduate students Philip Lee and Jasmine Graham. I would also like to thank Dr. John Kurhanewicz, Dr. Robert Bok, Dr. Peder Larson, Dr. Dwight Nishimura, Dr. Craig Levin, and Dr. Adam de la Zerda. To friends and colleagues while at the University of California San Francisco and Stanford University whom I am fortunate to know many, personal thank yous to Matthew Chapin, Daniel Bankman, James Lee, Adam Rossi, Huy Vu, Aaron Apsey, Joshua Fireman, Aisha Espey, Andrew Leynes, Natasha Holiday, Daniel Smolkin, Pavel Chvykov, and William Craigmile II. Thank you for support both in and out of the world that is California.

To all family who make my life. To my grandmother and grandfather Shirley and Paul Dunbar, thank you for shining the brightest on my path. I've been blessed by your guidance. My father Moon Sup Chung, thank you for your spirit, with or without intention as you elevated expectations I had of myself and always encouraged me to learn. To my mother Kimberly Dunbar, I am so thankful for all your brilliant, devoted, and inspiring ambitions and interests. Finally to my younger brother and sister James and Emily Chung: I am proud of all you are, all you do, and all you can and will be. There is no happier world than the one I live in with you. Lastly from the bottom of my heart, my love and thanks to Dr. Yeji Park. You truly amaze me.

*Brian Thomas Chung*

*December 2021*

# Abstract

Methods for Human Brain Metabolic Imaging using Hyperpolarized [2-$^{13}$C]Pyruvate

Brian Chung

Hyperpolarized (HP) $^{13}$C magnetic resonance imaging (MRI) has demonstrated the powerful potential for investigating and assessing tissue metabolism and microenvironmental alterations in diseases. Monitoring the distribution and biochemical conversion of injected HP $^{13}$C probes has recently enabled first-in-man clinical trials using novel quantitative imaging markers and shown an ability for noninvasive diagnosis and evaluation of many unmet clinical needs including cancer aggressiveness, response to therapy, and also for cardiac, kidney and liver disease. The modality has shown safety and feasibility for *in vivo* quantitative detection of metabolites in organs including the liver, brain, kidney, prostate and heart. This dissertation focuses on the development and application of the novel HP $^{13}$C molecular probe [2-$^{13}$C]pyruvate, to measure its metabolism for the first time in the brain of healthy human volunteers. MR spectroscopic data acquired from the first HP [2-$^{13}$C]pyruvate studies of human brain metabolism are presented with kinetic models estimating rates showing similar but not identical inter-subject values, culminating in the first MRI experiments using HP [2-$^{13}$C]pyruvate with a spectral spatial excitation pulse spotlighting spatial localization of its conversion to [5-$^{13}$C]glutamate and [2-$^{13}$C]lactate. Methods for introducing new parameters to improve quantification of HP [2-$^{13}$C]pyruvate to [5-$^{13}$C]glutamate using a two-site exchange model, and experimental designs to investigate the effects of unhealthy sleep for early detection of neurodisorders are also presented. The success of these first HP [2-$^{13}$C]pyruvate studies of human brain metabolism enables the design of further investigations and clinical trials to quantify human disease and disorders in new ways.

# Table of Contents

# List of Figures

# List of Tables

# Chapter 1

# Introduction

Magnetic resonance imaging (MRI) is a widely used, non-invasive and non-radioactive medical imaging modality. Frequently employed in hospitals, MRI enables clinicians and researchers to scientifically investigate a wide range of patient information, including anatomy, fluid perfusion, diffusion and metabolism. While a majority of clinical MRI studies acquire signal resulting from the magnetic field relaxation of the most abundant element in the human body hydrogen ($^{1}H$), isotopes of other elements such as carbon, sodium, fluorine and phosphorus can also be measured. This has granted an ability to acquire real-time differences in the rates of independent metabolic processes to characterize and differentiate degenerate from healthy organ tissue. In the following studies, Carbon-13 ($^{13}C$), a stable isotope of naturally abundant carbon, is the primary target for detection in Hyperpolarized (HP) $^{13}C$ MR.

HP $^{13}$C MR refers to imaging the HP $^{13}$C-labeled compound introduced into the subject and its downstream metabolites. While $^{13}$C is the only stable isotope of carbon detectable by traditional MRI, its low natural abundance in most living organisms, and its fundamental nonpolar characteristics, are two primary limitations for this technique's sensitivity. To enhance total signal from $^{13}$C-labeled compounds, a process called hyperpolarization (HP) may be performed, drastically increasing the polarization while simultaneously maintaining neutral chemistry and stability for safe injection. The resulting HP $^{13}$C solution is then injected *in vivo* and measured and identified by unique resonant frequencies as it undergoes chemical transformations within the subject. If the $^{13}$C-labeled compound is an active metabolite, then rates of metabolic processes may be modeled and quantified.

An active and significant challenge for the translation of HP $^{13}$C is the non-renewable and quick decay of the HP state, also unique to individual molecular probes and dependent on chemical structure. The most widely studied compound at the time of this dissertation is [1-$^{13}$C]pyruvate due to its favorable polarization properties and crucial role in a number of significant metabolic pathways. Monitoring metabolic changes using [1-$^{13}$C]pyruvate has enabled researchers to explore and investigate a number of pathologies, including cancer, heart disease, inflammatory arthritis, and traumatic brain injury in new ways. However the pathway detectable by [2-$^{13}$C]pyruvate commonly known as the TCA cycle cannot be measured by [1-$^{13}$C]pyruvate *in vivo* in humans. This metabolite-specific imaging requires development and optimization of the RF pulse design, width, time-bandwidth, repetition time, and other parameters, resulting in techniques which achieve spectral suppression and ultimately highlight metabolites of interest, which for this work includes [2-$^{13}$C]pyruvate, [2-$^{13}$C]lactate and [5-$^{13}$C]glutamate.

The first chapter introduces fundamental concepts of MR and dissolution dynamic nuclear polarization (dDNP), providing the reader with a scientific and technical background to HP $^{13}$C MRI and further outlining theory, principles, and technical challenges. Chapter 3 then explains biological significance of [2-$^{13}$C]pyruvate and translation of the technology from animal to human studies and clinical applications. Chapter 4 describes and presents the first-in-human initial HP $^{13}$C studies of [2-$^{13}$C]pyruvate metabolism in the human brain. This approach was then significantly advanced as described in Chapter 5 to enable first-ever HP [2-$^{13}$C]pyruvate imaging with whole brain coverage critical for impactful human studies. Chapter 6 describes signal and post-processing techniques on acquired data to improve quantification of [2-$^{13}$C]pyruvate to [5-$^{13}$C]glutamate conversion. Finally, Chapter 7 contains additional material on the design of novel sleep studies and early-stage clinical research on neurodisorders for the reader, outlining potential steps for future direction and application.

# Chapter 2

# Scientific and Technical Background

The following contains background information regarding scientific principles that enable MRI and HP $^{13}$C MRI, necessary to accomplish and comprehensively understand the experimental methods in this dissertation.

## 2.1 Fundamentals of Magnetic Resonance Imaging

### 2.1.1 Spin, Magnetic Resonance, Polarization

Nuclear spin is a concept interpreted and transcribed by physicists and engineers as a quantum mechanical angular momentum, physically manifesting in a phenomenon known as nuclear magnetic resonance (NMR)[1]. In attempts to visualize intrinsic physical properties, subatomic particles deemed nucleons considered to be charged spheres embody a magnetic moment, or “spin.” On Earth, many atoms with odd numbers of protons and neutrons possess this quantum property known as spin, and as protons ($^1$H) are the most abundant nuclei, they exhibit the simplest and easiest to acquire case of NMR from ubiquitous natural abundance. In humans and other known forms of life, $^1$H is also the most abundant and easiest NMR visible nucleus and it comprises a majority of living tissue[1,2].

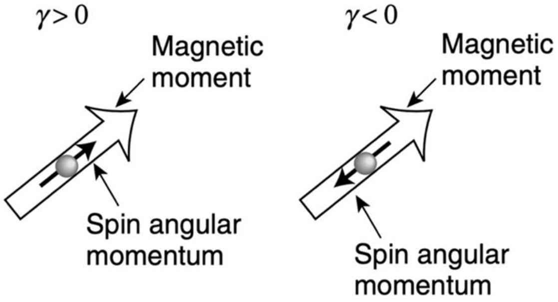

**Figure 2.1:** Spin angular momentum, magnetic moment and gyromagnetic ratio. Adapted from Levitt [3].

Spin can be written as a vector **S** with directionality aligned along its axis of rotation[1]. The magnetic dipole moment $\boldsymbol{\mu}$ is related by an approximate experimental real constant unique to the material, defined as the gyromagnetic ratio ($\gamma$)[3]:

$$\boldsymbol{\mu} = \gamma \boldsymbol{S} \tag{2.1}$$

The sign of $\gamma$ describes whether the net effect is parallel or antiparallel to the direction of **S**. The bulk magnetization vector **M** can be used to represent a macroscopic summation of magnetic moments:

$$\boldsymbol{M} = \sum \boldsymbol{\mu} \tag{2.2}$$

In quantum mechanics the spin angular momentum may also be written as a fundamental vector quantity where h is Planck's constant (h = 6.62606957 x $10^{-34}$ $m^2$ kg / sec) and **I** is the fundamental spin operator[1]:

$$\boldsymbol{S} = \frac{h}{2\pi}\boldsymbol{I} \tag{2.3}$$

At thermal equilibrium (no heat or work entering or leaving the system) and with no applied external magnetic field ($B_o$), spins orient in random directions resulting in net zero magnetization[3]. These spins align with the direction of an applied external magnetic field leading to a net difference in charge carrier populations and a nonzero magnetization vector. In this case the total magnetization at equilibrium is the net difference when the nuclei spins are aligned and anti-aligned with the applied field[3]:

$$M_o = \frac{N\mu(I+1)B_o}{3kT} \tag{2.4}$$

The potential energy E of a magnetic moment ($\mu$) in the presence of a B field aligned along the z-direction is[1]:

$$E = -\mu \cdot \boldsymbol{B} = -\mu_z B_o = -\gamma S_z B_o \tag{2.5}$$

For hydrogen and other particles with spin = ½, we can write the difference in the two energy states as[1]:

$$\Delta E = h\frac{\gamma}{2\pi}B_o \tag{2.6}$$

Where the ratio of these populations follows the Boltzmann distribution equation and k is Boltzmann's constant (k = 1.3806488 x $10^{-23}$ $m^2$ kg $s^{-2}$ $K^{-1}$)[1]:

$$\frac{n_+}{n_-} = e^{\Delta E/kT} \tag{2.7}$$

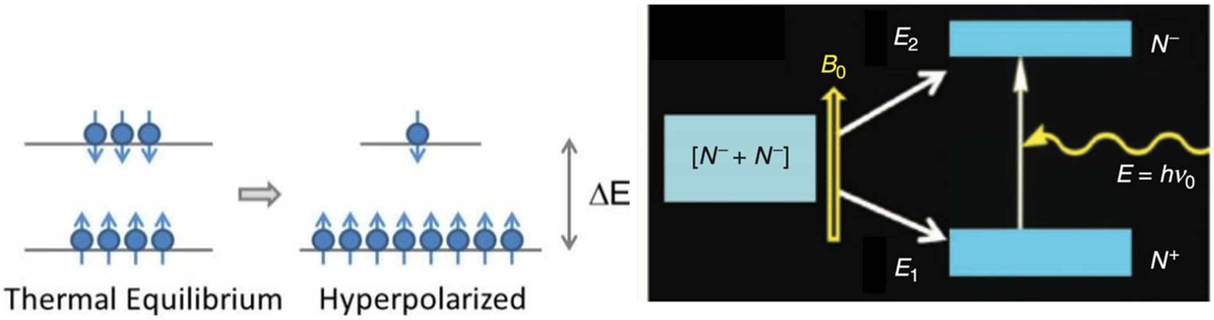

**Figure 2.2:** Splitting of energy levels in the presence of a magnetic field. Energy absorbed by the system creates two distinct energy levels when pulse frequency approximately matches $\Delta E$. Adapted from Bottomley et al. [2].

When there is an excess of spins in one energy state than another, uneven distribution of spins forms the basis of NMR signal. Polarization is defined similarly to optoelectronic charge carriers in semiconducting metals considering the ratio of spins aligned with $B_0$ over total spin population[2]:

$$P = \frac{n_+ - n_-}{n_+ + n_-} = \frac{e^{\Delta E/kT} - 1}{e^{\Delta E/kT} + 1} = \tanh(\frac{h\gamma B_o}{2kT}) \tag{2.8}$$

## 2.1.2 RF Excitation

NMR signal arises from precession of the net magnetization **M** originally aligned with a main magnetic field $\mathbf{B_o}$[1]. When **M** is tipped away from $\mathbf{B_o}$, namely by another external magnetic field $\mathbf{B_1}$, **M** precesses about $\mathbf{B_o}$, described by the following equation[1]:

$$\frac{d\boldsymbol{M}}{dt} = \boldsymbol{M} \times \gamma \boldsymbol{B_o} \tag{2.9}$$

Particular solutions for the above equation oscillate at the Larmor frequency ($\gamma$) defined by:

$$\omega = \gamma B_o \tag{2.10}$$

Nuclei have a specific gyromagnetic ratio inherent to the isotope at a given field strength $B_o$ as shown in Table 2.1[1].

**Table 2.1:** Natural abundance, gyromagnetic ratio (γ) and Larmor frequency (ω) at field strength $B_o$ = 3 T for selected nuclei. Adapted from Nishimura [1].

| Nuclei | Natural Abundance | $\gamma$ (MHz/Tesla) | $\omega$ (MHz at $B_o$ = 3 T) |
|---|---|---|---|
| $^{1}$H | 99.99% | 42.58 | 127.7 |
| $^{13}$C | 1.1% | 10.71 | 32.13 |
| $^{31}$P | ≈ 100% | 17.24 | 51.72 |
| $^{19}$F | ≈ 100% | 40.05 | 120.2 |
| $^{23}$Na | ≈ 100% | 11.26 | 33.78 |

We define the z-direction of $B_0$ as longitudinal and corresponding orthogonal xy-plane as transverse such that at M aligns with Bo at equilibrium and no external field $B_1$. When we apply $B_1$ as an RF pulse, it induces a torque on M away from equilibrium along the z-axis$^4$.

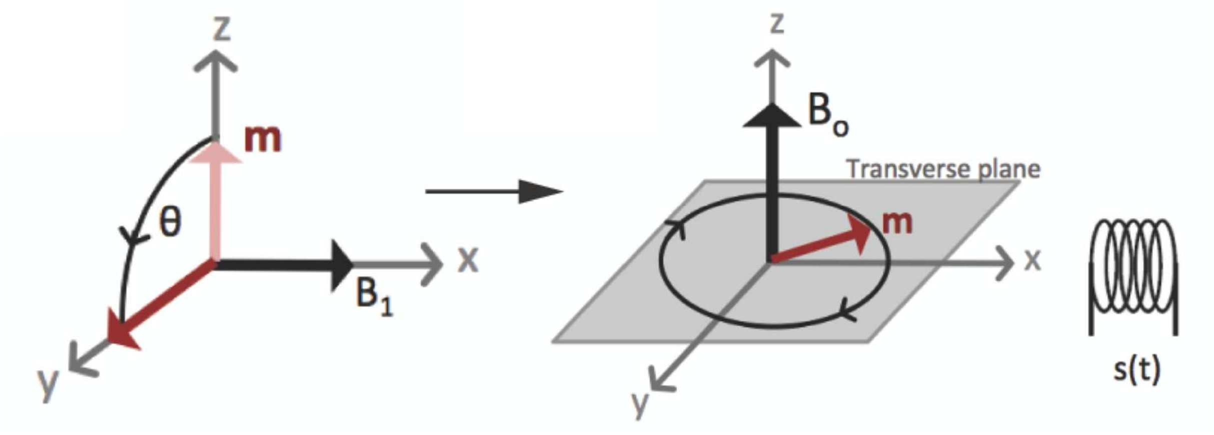

**Figure 2.3**: Following an RF pulse, the magnetization vector is tipped by a flip angle θ into the transverse plane (left), and then precesses and decays about Bo inducing an electromotive force in receiver coil (right). The force may be recorded as free induction decay (FID), translated to NMR or MRI signal s(t), and Fourier transformed to recover desired spectra. Adapted from Swisher et al. [5].

Following excitation, the resulting Free Induction Decay (FID) signal as the tilted M precesses around the z-axis at the Larmor frequency may be detected using RF coils according to Faraday's law of induction. The actual flip angle rotation (θ) of M as a result of $B_1$ may be determined considering its behavior where T is total experiment time[1,2]:

$$\theta = \omega_1 T \qquad \text{for constant } B_1$$

$$\theta = \gamma \int_0^T B_1(t)dt \qquad \text{for time-varying } B_1(t) \tag{2.11}$$

Hence a 90° ($\pi/2$) RF pulse flips M onto the transverse plane comprising the highest transverse signal. However if this $B_1$ pulse is removed or changed in time, the magnetization vector will incline to relax along its predilected orientation along $B_0$ and the flip angle (θ) will vary accordingly[4]. Similarly, a 180° ($\pi$) RF pulse will invert M to have no transverse components and no signal.

Non-selective excitation is another name for the first case of a $B_1$ field with constant amplitude and angle of excitation without a slice-selection gradient on[2]. After the magnetization vector is tipped from its original alignment with $B_0$, transverse components in the orthogonal plane can be calculated from trigonometric identities: the transverse $m_{xy}$ is the traditional sine of the flip angle and longitudinal $m_z$ is the cosine of the flip angle. For HP experiments involving dynamics and imaging where magnetization is non-recoverable, the flip angle employed is often much less than 90° to optimally preserve target magnetization[6].

For the cases of time-varying $B_1$ fields, the shape of the applied $B_1(t)$ pulse is determined through relative timings and strengths of directional gradients[4]. Slice selection can be achieved using a sinc-shaped $B_1(t)$ pulse and a constant gradient that imposes a linear variation on frequencies in space such that[7]:

$$f(z) = \frac{\gamma}{2\pi}(B_o + G_z) \tag{2.12}$$

Thereby limiting the cases to such that only an RF excitation pulse of Larmor frequencies that match the frequencies of the oscillating magnetic field is excited. Adjusting the bandwidth of the selective pulse and the amplitude of the slice selective gradient are additional parameters that modify overall slice thickness[4]. While optimizing the shape of the RF pulse this way in time can improve overall spatial selectivity, in practice there are limitations as an infinitely long sinc pulse is unreachable and a windowed sinc is often employed for imperfect and approximate slice selection[4].

The excitation profile of a $B_1(f)$ is the Fourier transform of $B_1(t)$ for small flip angles less than 90°. The RF excitation results in the magnetic moment being tipped away from the direction of the static field, with the duration of the RF pulse at the Larmor frequency often affecting and determining the angle between the static field and net magnetization axes[1]. Excited nuclei, considered to be in a higher energy state due to the absorption of energy, eventually return to a lower energy state emitting at the Larmor frequency through free induction decay (FID)[2]. This precession and decay about the static magnetic field is the recordable phenomena known as relaxation[1].

### 2.1.3 Relaxation

The resulting signal expected from RF excitation is an oscillation at the Larmor frequency bounded within a decay envelope. This decay may also be considered macroscopic relaxation of the net magnetization vector back to its original axis described using two relaxation time constants $T_1$ and $T_2$.

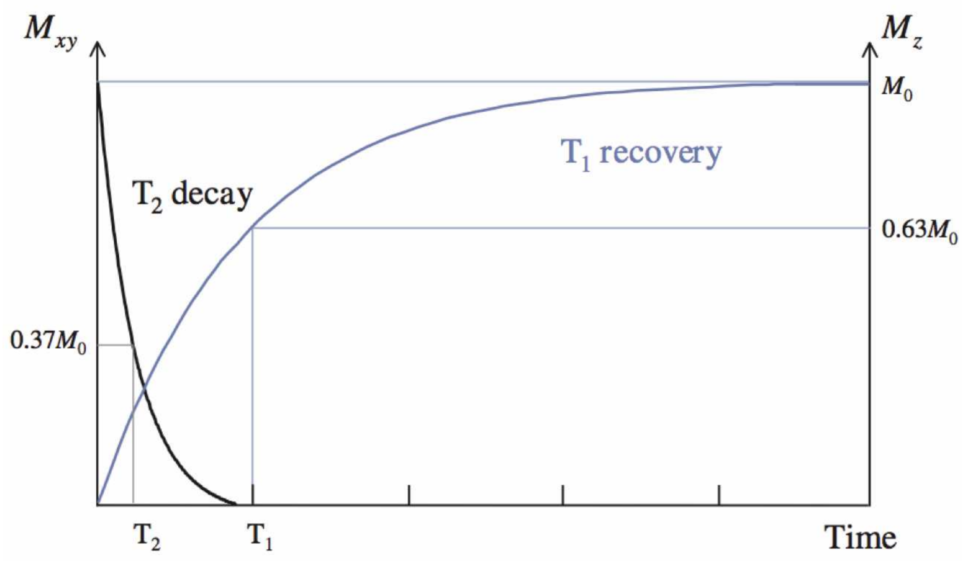

**Figure 2.4:** Magnetization decay and recovery governing $T_1$ and $T_2$ relaxation processes. Particular solutions to the differential equations are exponential, resulting in characteristic critical points from real approximations of *e*. Adapted from McRobbie et al. [7].

$T_1$ is known as the spin-lattice relaxation time, and it describes the recovery of the magnetization's longitudinal component, seeking to restore Boltzmann equilibrium[3]:

$$\frac{dM_z}{dt} = -\frac{M_z - M_0}{T_1} \tag{2.13}$$

In this first order differential equation, $M_z$ is the time-dependent longitudinal component of magnetization and $M_0$ is the magnetization at equilibrium. After M is tipped away from the longitudinal axis, the remaining $M_z$ component is always less than the original longitudinal magnetization and should eventually recover to this point[1]. Mechanisms governing spin-lattice relaxation result from induced field fluctuations due to molecular motion and include dipolar coupling, quadrupolar coupling, spin rotation, paramagnetics, and chemical shift anisotropy (CSA)[8]. To summarize, local fields experienced by nuclei change with molecular reorientation, however in HP $^{13}C$ studies it has been shown as $B_0$ increases, $T_1$ decreases due to dominant CSA relaxation mechanisms at higher fields, resulting in unintuitive faster HP

$^{13}C$ MR signal decay[2,4].

$T_2$ is known as the spin-spin relaxation time, and it relates to the decay of the magnetization's transverse component, resulting from interactions within a large number of microscopic magnetic dipoles[1,3]:

$$\frac{dM_{xy}}{dt} = -\frac{-M_{xy}}{T_2} \tag{2.14}$$

$T_2$ relaxation following an excitation pulse occurs in the transverse plane. After all dipoles are initially in phase, the spins almost immediately lose coherence and generate magnetic fields affecting other nuclei in tissue, on the local order of approximately 1 mT[5,9]. These varying local magnetic fields embody a transfer of energy from dipole to dipole, with the rate of transfer related to the rotation, translation and proximity of dipoles, increasing as the frequency of the variation of local magnetic fields approaches Larmor frequency[1,4]. As an example, pure $H_2O$ has a longer $T_2$ than when found in tissues and macromolecules, because nuclei can move considerably more unabatedly than at Larmor frequency, and hence $T_2$ is longer.

The actual decay of the transverse magnetization is a combination of the native decay constant $T_2$ and another term which depends on the homogeneity of the sample[1]. This is a similar constant $T_2^*$ that is specific to the material and defined as[3]:

$$\frac{1}{T_2^*} = \frac{1}{T_2} + \frac{1}{T_2'} = \frac{1}{T_2} + \gamma \Delta B_o \tag{2.15}$$

when considering a theoretical uniform magnetic field and no susceptibility effects, $T_2^*$ is equivalent to $T_2$. In clinical settings, $T_2^*$ is more practical as an experimental value due to imperfections in the static magnetic field $B_0$ and possible susceptibility effects in the patient and sample, as it is proportional to the inhomogeneity of the field strength.

Solutions to these differential equations yield[1]:

$$m_z(t) = M_o + (m_z(0) - M_o)e^{-t/T_1} \tag{2.16}$$

$$m_{xy}(t) = M_o e^{-t/T_2^*} \tag{2.17}$$

$T_1$ and $T_2$ relaxation are independent processes, and $T_1$ is often much longer than $T_2$. Reformulation of these equations into a singular combination known as the Bloch Equation provides a more complete and generalizable form[10]. For HP experiments, a long $T_1$ is desirable as a short $T_1$ can limit the acquisition time of the experiment and hence both the resolution and acquired temporal specificity. A long $T_2$ and minimization of $\Delta B_o$ is similarly optimal to increase SNR and enable acquisition at increased spatial resolution[5].

### 2.1.4 Bloch Equations and Chemical Exchange

When precession and relaxation are combined simultaneously considering both transverse and longitudinal components[10]:

$$\frac{d\boldsymbol{M}}{dt} = \boldsymbol{M} \times \gamma \boldsymbol{B} - \frac{m_x\hat{\imath} + m_y\hat{\jmath}}{T_2^*} - \frac{(m_z - M_o)\hat{k}}{T_1} \tag{2.18}$$

This phenomenological description of magnetization vector dynamics are known as the Bloch equations. The Bloch equations are a powerful set of coupled differential equations used to describe the behavior of a magnetization vector under any conditions. When integrated, the Bloch equations yield dimensional components of magnetization as functions of time[10].

$$\begin{aligned}\frac{d}{dt}M_x &= -\gamma(B_yM_z - B_zM_y)\\ \frac{d}{dt}M_y &= -\gamma(B_zM_x - B_xM_z)\\ \frac{d}{dt}M_z &= -\gamma(B_xM_y - B_yM_x)\end{aligned} \xrightarrow{\vec{B}=\left[B_1, 0, B_0 - \frac{\omega}{\gamma}\right]} \begin{aligned}\frac{d}{dt}M_x &= (\omega_0 - \omega)M_y - \frac{1}{T_2}M_x\\ \frac{d}{dt}M_y &= -(\omega_0 - \omega)M_x - \frac{1}{T_2}M_y + \omega_1 M_z\\ \frac{d}{dt}M_z &= -\omega_1 M_y - \frac{1}{T_1}(M_z - M_0)\end{aligned}$$

**Figure 2.5:** Bloch equations in component form evaluated and solved using a variety of mathematical software.

The Bloch equations are particularly useful when introducing additional experimental parameters such as chemical exchange[1,2]. In this form, the Bloch equations can be modified considering relaxation as a result of chemical reactivity, defined as chemical exchange. Chemical exchange is any process where a nucleus exchanges energy between two or more environments affecting its measurable NMR parameters including chemical shift, dipolar coupling, and relaxation rate. Examples include intracellular phenomena such as protein folding or enzyme catalyzed reactions, binding, and protonation[5].

The Bloch equations for a spin that can be in state A or $B$ in the absence of exchange:

$$\frac{d\boldsymbol{M_1}}{dt} = \boldsymbol{M_1} \times \gamma \boldsymbol{B_1} - R_1(\boldsymbol{M_1} - \boldsymbol{M_{10}}) \tag{2.19}$$

$$\frac{d\boldsymbol{M_2}}{dt} = \boldsymbol{M_2} \times \gamma \boldsymbol{B_2} - R_2(\boldsymbol{M_2} - \boldsymbol{M_{20}}) \tag{2.20}$$

where $R_1$ and $R_2$ are matrices containing relaxation parameters for state A and B respectively and M are longitudinal and transverse magnetization vectors as functions of time or initial conditions[11,12].

Assuming exchange from state A to B and its reverse are instantaneous, the equations modified to include exchange with the addition of a first order kinetics term[5,12]:

$$\frac{d\boldsymbol{M_1}}{dt} = \boldsymbol{M_1} \times \gamma \boldsymbol{B_1} - R_1(\boldsymbol{M_1} - \boldsymbol{M_{10}}) + \boldsymbol{k}(\boldsymbol{M_2} - \boldsymbol{M_1}) \tag{2.21}$$

$$\frac{d\boldsymbol{M_2}}{dt} = \boldsymbol{M_2} \times \gamma \boldsymbol{B_2} - R_2(\boldsymbol{M_2} - \boldsymbol{M_{20}}) + \boldsymbol{k}(\boldsymbol{M_1} - \boldsymbol{M_2}) \tag{2.22}$$

The differences in J-coupling constants primarily characterize exchange regimes. Fast exchange ($k \ll |\delta_1 - \delta_2|$) results in a single resonance shifted by a weighted average of two independent chemical shifts. Intermediate exchange ($k \approx |\delta_1 - \delta_2|$) results in coalescence observed through line broadening. Slow exchange ($k \gg |\delta_1 - \delta_2|$) results in separate lines observable for each state, with theoretical line broadening = $\mathrm{k}/\pi$.

In NMR spectroscopy a rotating coordinate frame is used, the rotation frequency of which equals the Larmor frequency of the nuclei. The Bloch equations conveniently consider all nuclei rotating with the Larmor frequency fixed in this coordinate frame[1,10].

Comparable with the 21st century's rise of linear algebra engineering applications resulting from the popularity of software algorithms and transistor logic over other rigorous forms of mathematics including multivariate calculus and topology, an ingenuity underlying the Bloch equations is in the succinct form which allows it to represent imaging concepts.

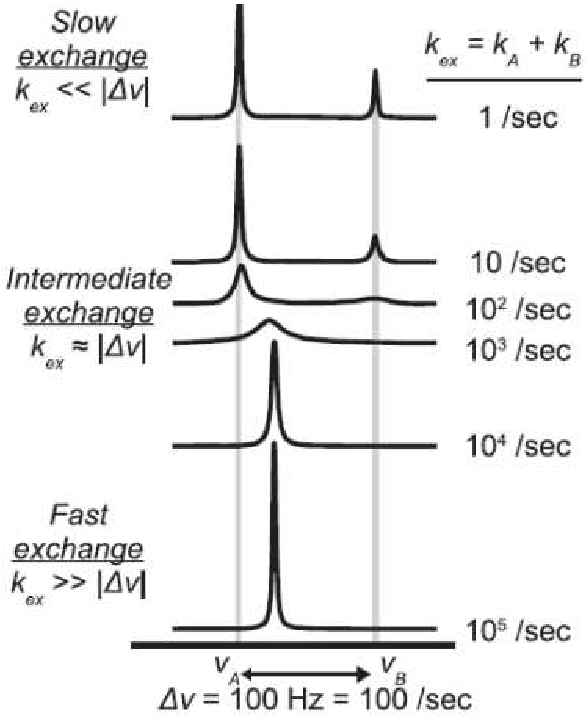

**Figure 2.6:** Characteristic exchange regimes with approximate scale. Slow exchange is ideal for rigorous models to determine kinetic rates. Adapted from Swisher et al. [5].

### 2.1.5 Chemical Shift

In practice a particle's spin resonance at a given field strength is only approximated by the Larmor frequency. At theoretical equilibrium, orbiting electrons can shield nuclei from a primary magnetic field $B_0$ resulting in actual spins experiencing a slightly lower field than applied[1]. The difference in the chemical environment and nature of electron densities is recorded as a frequency deviation known as chemical shift. The following comprises the fundamentals of magnetic resonance spectroscopy[3].

Factors influencing chemical shift include the previously mentioned nuclei and electron density interactions, as well as the electronegativity of nearby groups, and anisotropic induced magnetic field effects. If a particle is in the vicinity of an electronegative atom, it may experience a reduction in its own electron density, also resulting in deshielding of its nuclei. Anisotropic induced magnetization field effects can result from the appearance of locally induced magnetic fields and can be paramagnetic when parallel to the applied field or diamagnetic when opposed. This phenomenon corresponds with another change in the local magnetic field resulting in a chemical shift of the recorded Larmor frequency[1,3].

When orbiting electrons shield nuclei from the primary magnetic field $B_o$, the spins experience a slightly lower field. The change in frequency can be written as[1]:

$$\omega = \gamma B_o(1-\sigma) \tag{2.23}$$

The varying peak locations across an acquired NMR spectrum are the primary result of chemical shift. In practice, varying Bo and taking multiple measurements with respect to a reference characterizes and measures chemical shift.

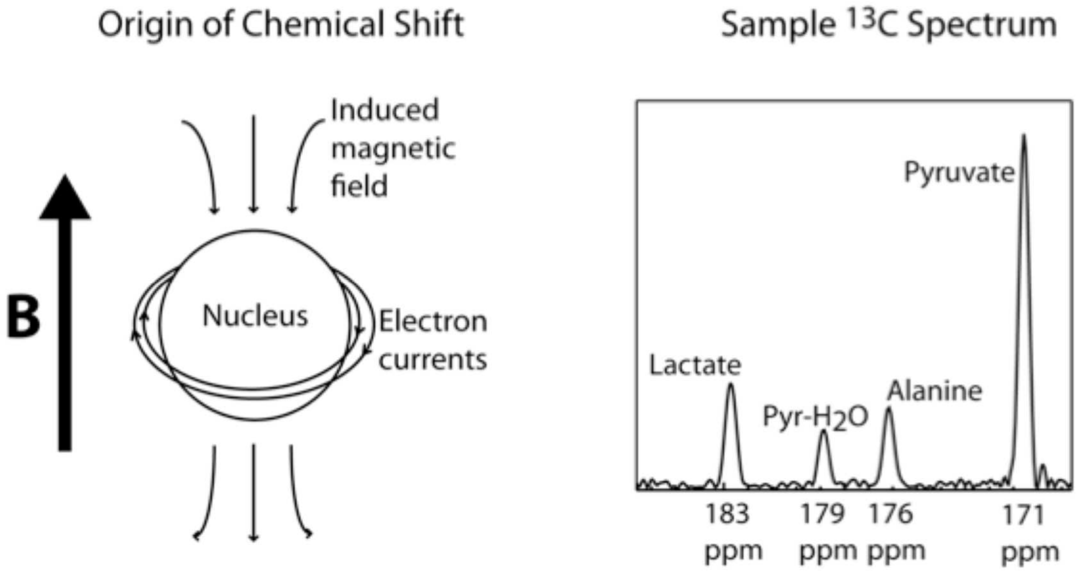

**Figure 2.7:** Chemical shift from an induced magnetic field in addition to the main field, resulting in a molecular dependent shift of the Larmor frequency. Sample HP $^{13}$C spectrum with chemical shifts. Adapted from Swisher et al. [5].

In one-dimensional NMR, the signal is recorded as a function of time and then Fourier transformed to yield a spectrum as a function of frequency. This may be extended to further dimensions when recorded as a function of additional independent time variables from the linearity superposition principle of the Fourier transform[13]. The horizontal axis of a traditional NMR spectra ranges in reverse from left to right, with 0 ppm shift representing the reference sample with greatest electron shielding and least frequency change[1].

### 2.1.6 Magnetic Resonance Imaging Principles

MRI is a standard medical imaging diagnostic modality that can provide excellent contrast for investigating soft tissue in regions such as the brain, abdomen and pelvis. It employs three primary types of magnetic fields: $B_0$ (main static field), $B_1(t)$ (RF excitation), and G(t) (gradients for spatial and temporal localization)[1]. The general solution to the Bloch equations in 3-dimensions can be written as a signal equation of the form[10]:

$$s(t) = \iint m(x,y) e^{-i2\pi[k_x(t)x + k_y(t)y]}\, dxdy \tag{2.24}$$

$$\vec{k}(t) = \frac{\gamma}{2\pi} \int_0^t \vec{G}(\tau)\, d\tau \tag{2.25}$$

Here s(t) is recognized as the 2D transform of m(x,y) at spatial frequency k(t). In practice, sampling across a range of spatial frequency "space," also known as k-space, and subsequently applying a 2D Fourier Transform (2DFT) on the resulting signal yields magnetization information contrast as an image[13]. Adequate k-space coverage and sufficient sampling by strategically varying the magnitudes and durations of gradient fields as well as acquisition timing determines the overall quality of the image[1].

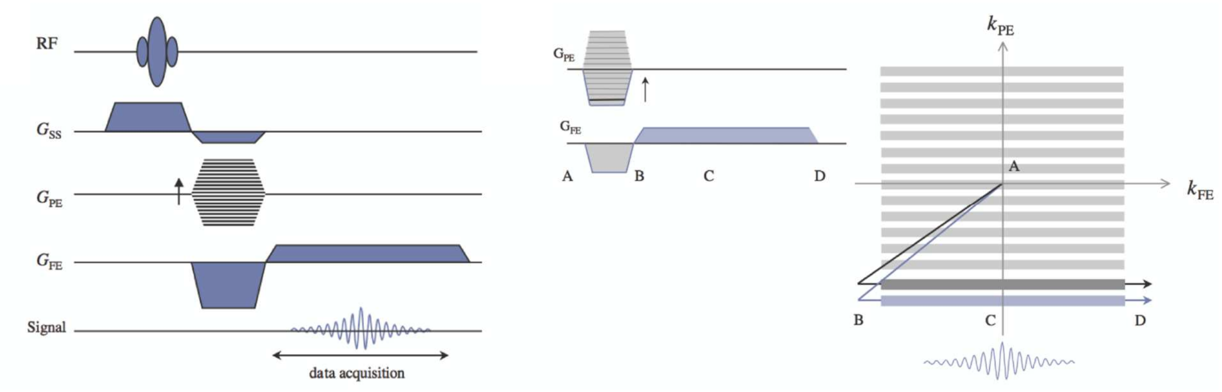

**Figure 2.8:** A 2D FT imaging sequence. Adapted from McRobbie et al. [7].

$G_x(t)$ and $G_y(t)$ are defined as standard readout and phase encoding gradients respectively. A standard 2DFT imaging sequence and the subsequent traversal through k-space, where $G_x(t)$ encodes along $k_x$ and $G_y(t)$ moves along $k_y$ is shown[14]. Considering the linearity of the Fourier transform, these concepts and equations can be extended to additional imaging dimensions, by adding $k_z$ and $G_z(t)$ or likewise terms. Magnetic resonance spectroscopic imaging (MRSI), also known as chemical shift imaging (CSI), is one example and an extension of MR spectroscopy where the distribution of multiple metabolites in an excited region is detected by introducing a spectroscopic dimension[15]. In this case, $k_f$ is not traversed across a range of frequencies with the application of gradients but rather in an absence of gradients as with traditional NMR[4].

Spectroscopic imaging techniques acquire spectral information in each spatial voxel, reducing need for prior knowledge about spectral resonances of HP compounds, with amplitudes and shapes of acquired peaks illustrating information about the chemical behavior and spin coupling of each compound[15].

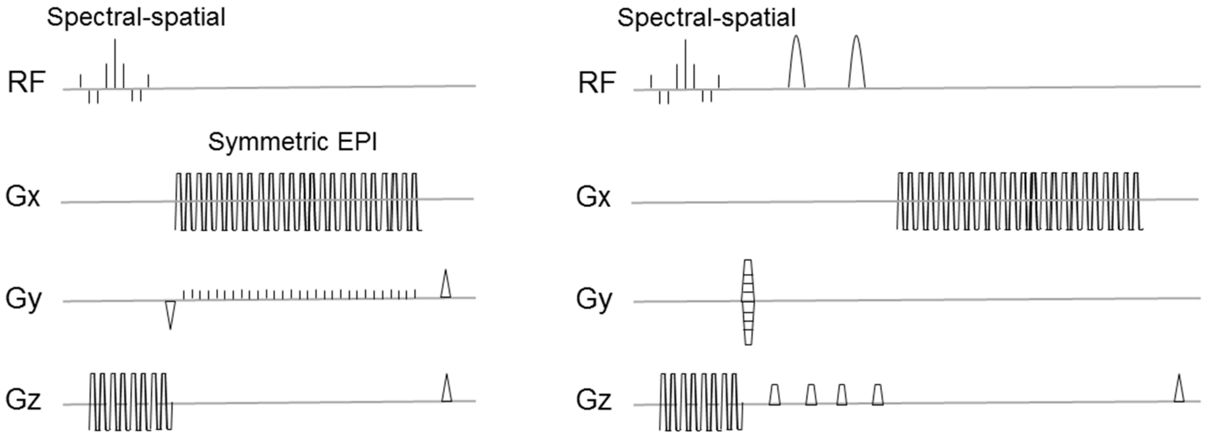

**Figure 2.9:** Pulse sequences for rapid HP $^{13}C$ acquisitions: 2D multislice EPI and 2D EPSI. Adapted from Chen et al. [16].

While narrow-band excitation pulses with multifrequency shifts in series can sufficiently superimpose over the $^{13}C$ spectrum of interest, this strategy is not ideal for slice-selective imaging applications due to spatial mis-registrations in the presence of chemical shift[17]. For broadband spectral excitations, spectral-spatial pulses can offer advantage through simultaneous control of frequencies, locations, and flip angles for HP $^{13}C$ acquisitions[19].

Traditional acquisition techniques enable detection of all $^{13}C$ resonances across the spectral bandwidth by encoding for each spatial k-space location, however requiring numerous phase encodes that can be time costly. To accelerate this, one simple strategy is to interleave spectral and spatial encoding using techniques such as Echo Planar Spectroscopic Imaging (EPSI), and spiral CSI[20]. These types of sequences feature shorter bandwidths due to shortened echo-spacing, a phenomenon where the symmetry of free induction decay is taken advantage of by recording the readout of successive RF pulses separated with a predetermined echo time (TE)[16,18]. Fast readout trajectories such as echo planar, spiral, and concentric ring reduce overall sampling speeds and improve spatial resolution and coverage[18-20].

The following inverse relationships apply to real image and k-space in the readout direction[16]:

$$FOV = \frac{1}{\Delta k} \tag{2.26}$$

$$\delta = \frac{1}{K_{max}} = \frac{1}{n\Delta k} \tag{2.27}$$

Where FOV is the real image field of view, $\Delta k$ is the k-space sampling rate, $K_{max}$ is the total window width determined by the product of number of samples $n$ and sampling rate, and $\delta$ is resolution. The relationships also apply to phase-encoding directions if the gradient is activated prior to data sampling[18].

Total SNR is directly correlated with resolution in each dimension, and also the square root of total acquisition time, which itself is a product of acquisition time for a single TR (repetition time, often related to echo time TE) unit, number of phase encodes, and number of signal averages ignoring transverse decay effects[1]. Hence to maintain equivalent SNR for a twice-fold resolution improvement in each dimension, the total scan time should be increased by at least a factor of sixteen[5].

## 2.2 Introduction to Hyperpolarized $^{13}$C Magnetic Resonance for Molecular Imaging

### 2.2.1 Dissolution Dynamic Nuclear Polarization

The relatively low polarization of nuclear spins of low concentration metabolites at thermal equilibrium and nuclei with rare natural abundance results in low sensitivity for MR molecular imaging. Even using high concentrations, large sample volumes and acquisition strategies with time intensive signal averaging, the applications of NMR are limited to detect some nuclei with small gyromagnetic ratios in the clinical setting. For carbon, approximately 99% of its natural abundance is $^{12}$C and not NMR detectable; however 1% is $^{13}$C and NMR detectable[14,16].

Dissolution Dynamic Nuclear Polarization (dDNP) is a technique that overcomes this challenge by providing over $10^4$ times signal enhancement for HP $^{13}$C MR resulting in great increases in SNR[21]. The transfer of spin polarization from electrons to nearby nuclei is performed by microwave irradiation at a cryogenically low temperature in a sustained magnetic field; the nuclei and electrons are in close proximity while a free radical is introduced in the dissolution process. The irreversible processes that govern the transfer of electron polarization in close proximity to the $^{13}$C nucleus include solid effects, cross effects, and thermal mixing from electron-neutron spin interactions[18,21]. Nuclear spins can also homogenously distribute polarization to and through neighboring nuclear spins via spin diffusion[3].

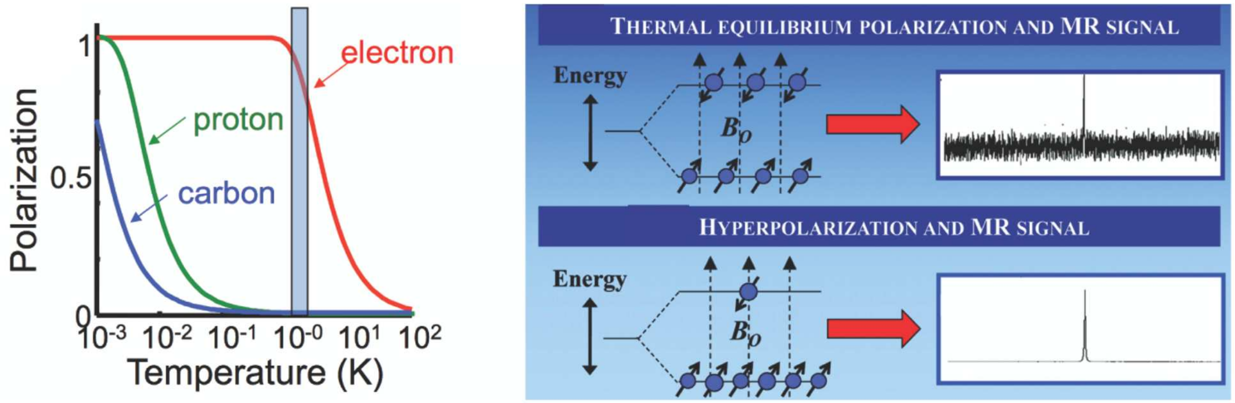

**Figure 2.10:** Polarization vs. temperature (K) for subatomic particles. Electron polarization at 1 K is nearly saturated and 1000x greater than $^1$H and $^{13}$C nuclei. DNP enables the transfer of polarization by biasing a considerable redistribution of spins compared to thermal equilibrium and increasing SNR by > $10^4$. Adapted from Milshteyn et al. [14].

Oscillating microwave irradiation transmitted via RF coils at a frequency that is the sum or difference of the electron and nuclear Larmor resonant frequencies induces the coupled interaction of spins. The magnetic field frequency matches the nuclei's resonant frequency energy and the sample's magnetic moment changes direction resulting in RF excitation and a net change in magnetization[14,16]. The HP MR signal is irreversible and temporary as the sample immediately begins to relax to thermal equilibrium when no longer irradiated[21].

**Figure 2.11:** HyperSense (left) commercially available preclinical polarizer. 5T GE SPINlab (right) clinical polarizer for up to 4 sample vials in parallel with sterile fluid paths and a QC system for safe human injection. Standard operational steps of the HyperSense include: (1) the buffer is heated and pressurized, (2) the sample space is pressurized, (3) the sample is raised out of the liquid Helium, (4) the dissolution stick is lowered docking with the sample holder, (5) the solvent is injected dissolving the sample while preserving enhanced polarization.

### 2.2.2 Hyperpolarized $^{13}$C Magnetic Resonance Imaging with [1-$^{13}$C]Pyruvate

[1-$^{13}$C]Pyruvate features excellent properties for DNP with a long $T_1$, a high polarization ceiling enabling high SNR and an important role in cellular metabolism[5]. Following preclinical studies monitoring tumor progression, formation, and response to therapy, the probe was rapidly translated for use in clinical trials in prostate cancer patients, demonstrating great promise for HP $^{13}$C technology[22].

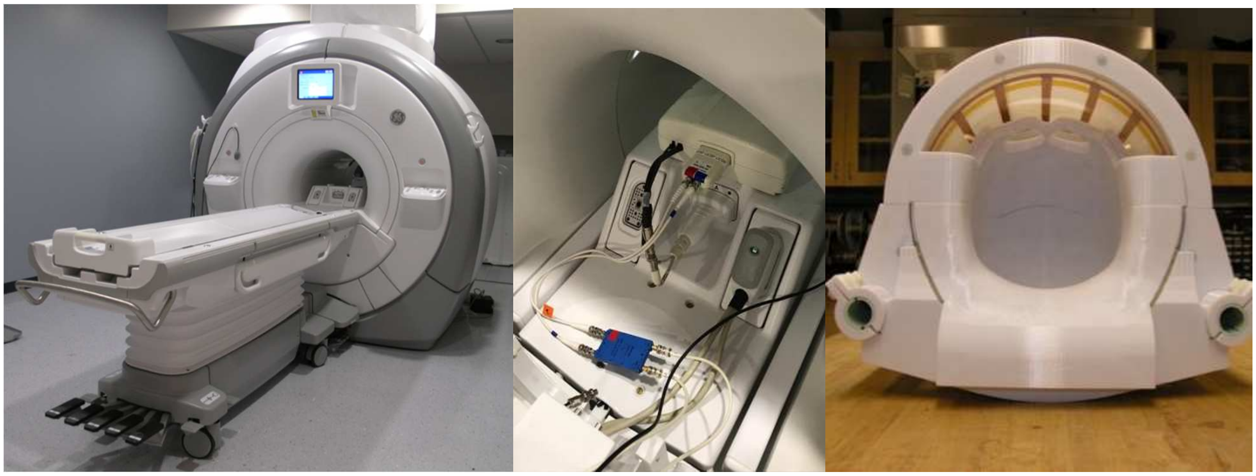

**Figure 2.12:** Clinical 3T GE MR Scanner at the UCSF Surbeck Laboratory for Advanced Imaging, 32-channel head coil with de-tunable transmission birdcage and receiver array used for human volunteer studies.

Metabolite-specific broadband EPI pulse sequences designed for rapid and robust volumetric imaging of HP [1-$^{13}$C]pyruvate and other molecules have employed built-in spectral-spatial RF pulses and flip angle schemes optimized for pyruvate and other metabolites, and enabled specific patient studies with capabilities to integrate customized pulses and flip angles[16,17,20]. Commonly used techniques include ramp-sampling, partial-Fourier, and Nyquist ghost corrections, and sequences are compatible with clinical MR scanners and reconstruction and analysis software[18].

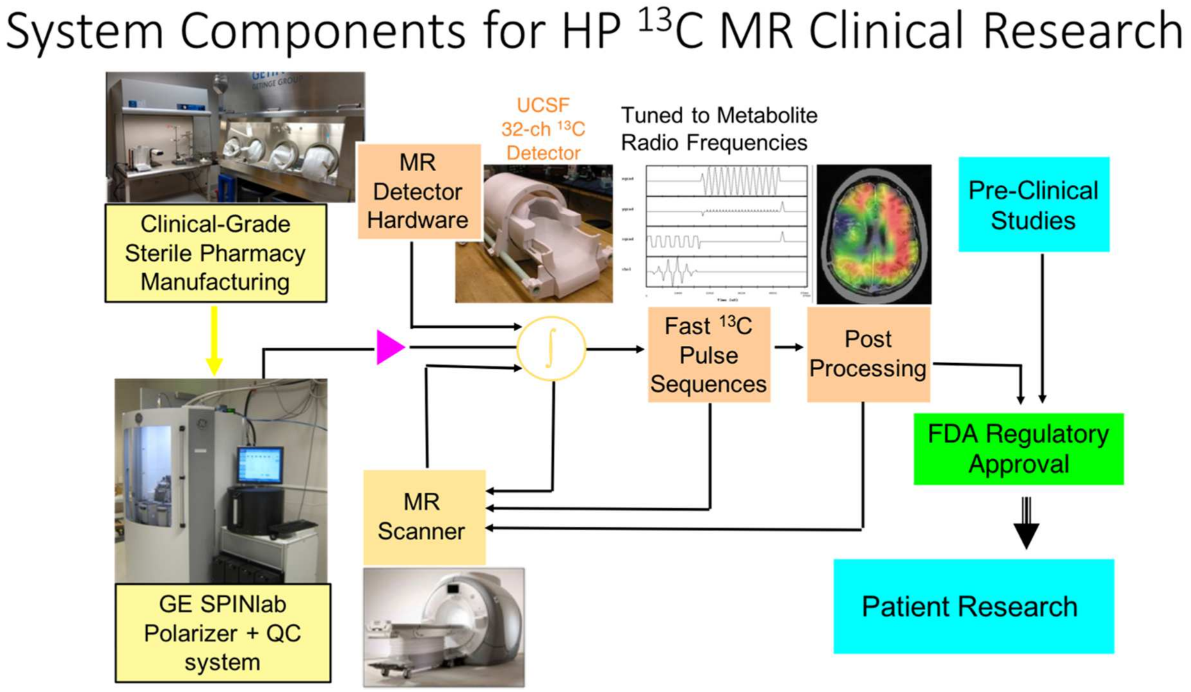

**Figure 2.13:** Schematic illustrating system components for Hyperpolarized $^{13}C$ MR clinical research. A clinical-grade sterile pharmacy manufacturing and GE SPINlab with built-in QC system are used for sample preparation. Experiments are conducted with specifically engineered MR detector hardware, a traditional MR scanner and fast $^{13}C$ pulse sequence designs. Following post-processing steps, and combined with pre-clinical studies, FDA regulatory approval requirements are met to translate experimental methods to patient research. Adapted from Wang et al. [23].

To date [1-$^{13}C$]pyruvate is the most widely studied and used HP $^{13}C$ probe[22]. Pyruvate is an important product of the glycolytic pathway with an ability to report on the Warburg effect observed in many cancer cells. HP [1-$^{13}C$]pyruvate MR metabolic imaging has been applied to identify tumor metabolism[22,24], assess aggressiveness[25], evaluate treatment response[26], and probe organ function[24,27]. It is therefore hypothesized HP [2-$^{13}C$]pyruvate with the $^{13}C$ isotope enriched in the 2-position can provide novel metabolic information for human brain studies[28] considering its unique position atop multiple anaplerotic and cataplerotic cascades in the tricarboxylic acid (TCA) cycle.

The power of metabolic imaging HP $^{13}$C-labeled cell substrates is the information it provides on dynamic processes. However, one weakness is it provides no information on the concentrates of the labeled substrates and therefore quantitative information on flux cannot directly be determined or expressed[5].

Regarding practical requirements for HP $^{13}$C MRI, the high costs of a dedicated polarizer in the million-dollar range and a state-of-the-art MR scanner currently limit the feasibility of performing the high-end imaging modality primarily to non-academic institutions, where the interprofessional collaborations among many physicists, scientists, engineers, pharmacists, technologists, and nurses contributes significantly to its competitive success. Finally the evidence of clinical utility in Phase II and III clinical trials has yet to be demonstrated for the FDA to approve the HP $^{13}$C imaging modality for routine clinical use[18,22].

# References

[1] Nishimura DG. Principles of Magnetic Resonance Imaging. Stanford University, 2010.

[2] Bottomley PA, Griffiths JR, et al. Handbook of magnetic resonance spectroscopy in vivo: MRS theory, practice and applications. John Wiley & Sons, 2016.

[3] Levitt MH. Spin Dynamics: Basics of Nuclear Magnetic Resonance. John Wiley & Sons, 2013.

[4] Haacke M, Brown R, et al. Magnetic Resonance Imaging: Physical Principles And Sequence Design, Wiley-Liss, 1999.

[5] Swisher CL. Hyperpolarized $^{13}$C Magnetic Resonance Spectroscopy: Probing Enzymatic Activity, Cellular Transport, and Oncogene Activation, 2014.

[6] Maidens J, Gordon JW, Arcak M, Larson PEZ. Optimizing Flip Angles for Metabolic Rate Estimation in Hyperpolarized Carbon-13 MRI. IEEE Trans Med Imaging. 2016;35(11):2403-2412. doi:10.1109/TMI.2016.2574240.

[7] McRobbie DW, Moore EA, et al. MRI From Picture to Proton, 3rd ed., Cambridge University Press, New York, 2007.

[8] Goldman M. Formal theory of spin--lattice relaxation. J Magn Reson. 2001 Apr; 149(2):160-87. doi: 10.1006/jmre.2000.2239. PMID: 11318616.

[9] Hu S. Hyperpolarized 13C Magnetic Resonance Spectroscopic Imaging: Pulse Sequence Development for Compressed Sensing Rapid Imaging and Preclinical Liver Studies, 2009.

[10] Bloch F. The Principle of Nuclear Induction. Science. 1953;118(3068):425-430. doi:10.1126/science.118.3068.425.

[11] McConnell HM. Reaction Rates by Nuclear Magnetic Resonance. J. Chem. Phys. 1958; 28, 430–431.

[12] Abergel D, Palmer AG. Approximate solutions of the Bloch-McConnell equations for two-site chemical exchange. Chemphyschem. 2004;5(6):787-793. doi:10.1002/cphc.200301051.

[13] Bracewell R. The Fourier Transform and Its Applications. McGraw-Hill, 2000.

[14] Milshteyn E. Development of High Spatiotemporal Resolution Imaging of Hyperpolarized C-13 Compounds using the Balanced Steady-State Free Precession Sequence, 2017.

[15] Kohler SJ, Yen Y, Wolber J, Chen AP, Albers MJ, Bok R, et al. In vivo 13 carbon metabolic imaging at 3T with hyperpolarized 13C-1-pyruvate. Magn Reson Med 2007;58:65-9.

[16] Chen HY. Development and Translation of 3D Dynamic Hyperpolarized 13C-MR Metabolic and Perfusion Imaging – From Mice to Patients, 2017.

[17] Marco-Rius I, Cao P, von Morze C, et al. Multiband spectral-spatial RF excitation for hyperpolarized [2-13 C]dihydroxyacetone 13 C-MR metabolism studies. Magn Reson Med. 2017;77(4):1419-1428. doi:10.1002/mrm.26226.

[18] H. Qin, Hyperpolarized C-13 Magnetic Resonance Imaging for Assessing Tissue Metabolism and Microenvironment: Technical Development, Preclinical Validation, and Clinical Translation, 2021.

[19] Bernstein M, King K, Zhou X. Handbook of MRI Pulse Sequences. Elsevier Academic Press, 2004.

[20] Hu S, Lustig M, Balakrishnan A, et al. 3D compressed sensing for highly accelerated hyperpolarized (13)C MRSI with in vivo applications to transgenic mouse models of

cancer. Magn Reson Med. 2010;63(2):312-321. doi:10.1002/mrm.22233.

[21] Ardenkjaer-Larsen JH, Fridlund B, Gram A, et al. Increase in signal-to-noise ratio of > 10,000 times in liquid-state NMR. Proc Natl Acad Sci U S A. 2003;100(18):10158-10163. doi:10.1073/pnas.1733835100.

[22] Kurhanewicz J, Vigneron DB, Ardenkjaer-Larsen JH, et al. Hyperpolarized 13C MRI: Path to Clinical Translation in Oncology. Neoplasia. 2019;21(1):1-16. doi:10.1016/j.neo.2018.09.006.

[23] Wang ZJ, Ohliger MA, et al. Hyperpolarized 13C MRI: State of the Art and Future Directions. Radiology. 2019 May;291(2):273-284. doi: 10.1148/radiol.2019182391. Epub 2019 Mar 5. PMID: 30835184; PMCID: PMC6490043.

[24] Golman K, Zandt RI, Lerche M, Pehrson R, Ardenkjaer-Larsen JH. Metabolic imaging by hyperpolarized 13C magnetic resonance imaging for in vivo tumor diagnosis. Cancer Res. 2006;66(22):10855-10860. doi:10.1158/0008-5472.CAN-06-2564.

[25] Chen HY, Larson PEZ, Bok RA, et al. Assessing Prostate Cancer Aggressiveness with Hyperpolarized Dual-Agent 3D Dynamic Imaging of Metabolism and Perfusion. Cancer Res. 2017;77(12):3207-3216. doi:10.1158/0008-5472.CAN-16-2083.

[26] Aggarwal R, Vigneron DB, Kurhanewicz J. Hyperpolarized 1-[13C]-Pyruvate Magnetic Resonance Imaging Detects an Early Metabolic Response to Androgen Ablation Therapy in Prostate Cancer. Eur Urol. 2017;72(6):1028-1029. doi:10.1016/j.eururo.2017.07.022.

[27] Cunningham CH, Lau JY, Chen AP, et al. Hyperpolarized 13C Metabolic MRI of the Human Heart: Initial Experience. Circ Res. 2016;119(11):1177-1182. doi:10.1161/CIRCRESAHA.116.309769.

[28] Park I, Larson PEZ, Gordon JW, et al. Development of methods and feasibility of using hyperpolarized carbon-13 imaging data for evaluating brain metabolism in patient studies. Magn Reson Med. 2018;80(3):864-873. doi:10.1002/mrm.27077.

# Chapter 3

# Translation of HP $^{13}$C MR for [2-$^{13}$C]Pyruvate Human Brain Research

## 3.1 Motivation for Hyperpolarized $^{13}$C Magnetic Resonance Imaging with [2-$^{13}$C]Pyruvate

HP $^{13}$C MR molecular imaging provides a unique ability to image and measure human metabolic processes in novel ways to acquire insight about how cellular bioenergetic pathways are organized and function. The modality utilizes the engineered phenomenon of dissolution dynamic nuclear polarization (dDNP) where nuclear spins in the solid state are hyperpolarized through coupling with unpaired electrons added via an organic free radical[1,2]. Dissolution DNP provides over 10,000 fold signal enhancement for HP $^{13}$C MRI, enabling a novel stable-isotope molecular imaging approach for preclinical and recently clinical research studies demonstrating both safety and translational potential for human HP $^{13}$C molecular imaging[1-5].

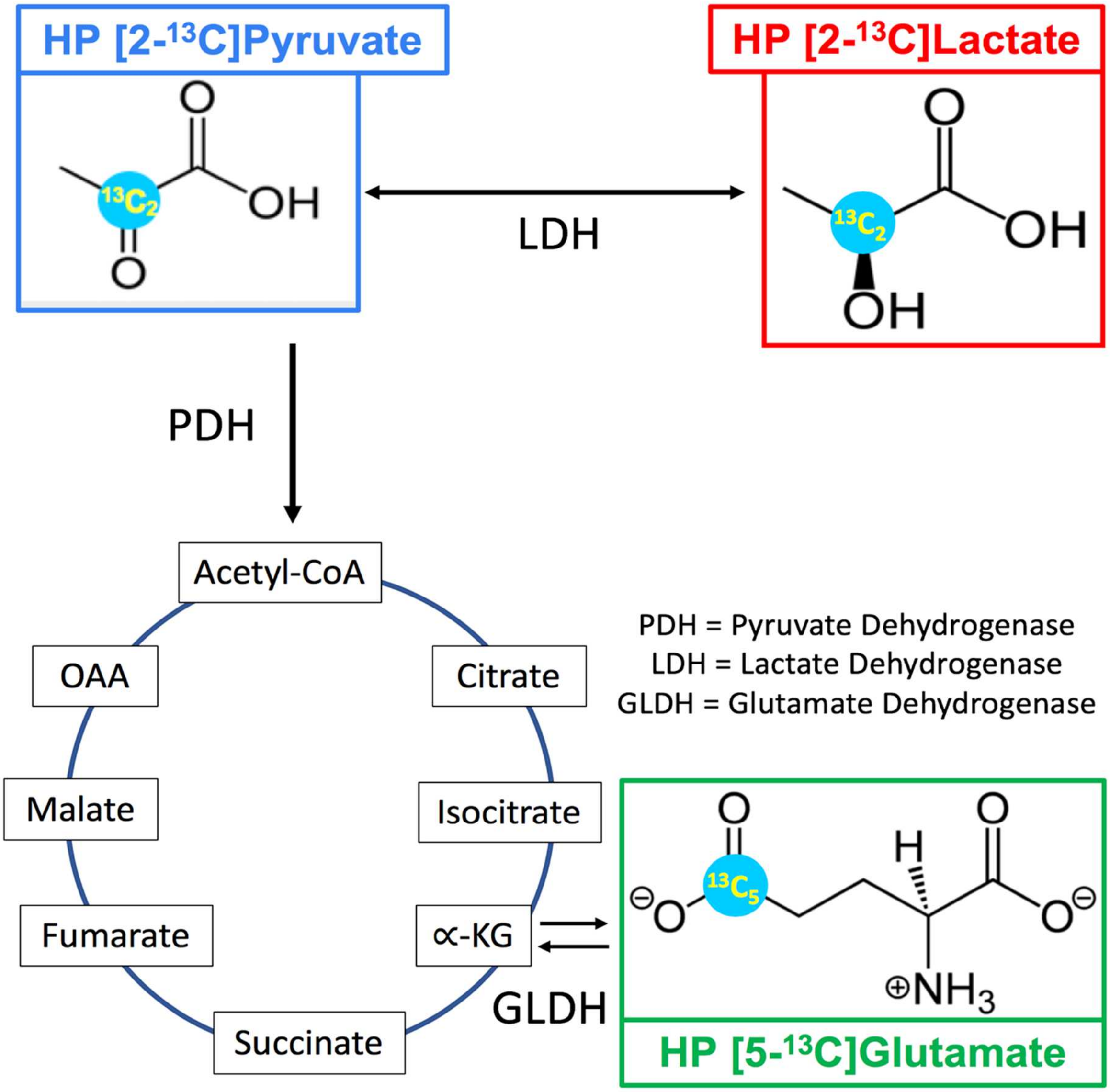

**Figure 3.1:** Diagram illustrating [2-$^{13}$C]pyruvate metabolism investigated by this HP $^{13}$C MR study of the human brain. HP pyruvate with the $^{13}$C isotope enriched in the 2-position ([2-$^{13}$C]pyruvate) have successfully shown direct detection of downstream metabolites such as [5-$^{13}$C]glutamate following its conversion to acetyl-CoA.

Although HP [1-$^{13}$C]pyruvate is the most widely utilized molecular contrast agent for MR metabolic imaging, there may be similar strong diagnostic potential for HP [2-$^{13}$C]pyruvate in particular investigating human brain metabolism. In a [1-$^{13}$C]pyruvate study bicarbonate signal, indicating flux of [1-$^{13}$C]pyruvate through pyruvate dehydrogenase (PDH) resulting in $CO_2$ and its rapid conversion to bicarbonate, had a similar consistent spatial distribution and was also highest in many similar regions such as the occipital lobe as [1-$^{13}$C]lactate, a metabolic byproduct of [1-$^{13}$C]pyruvate[5].

MR detection of the conversion of HP [1-$^{13}$C]pyruvate to [1-$^{13}$C]lactate catalyzed by lactate dehydrogenase (LDH) has demonstrated research value and clinical potential in Phase I trials of cancer patients spotlighting the Warburg Effect[3] with greatly upregulated LDH activity[6,7]. In approaching the TCA cycle however, [1-$^{13}$C]pyruvate is enzymatically metabolized via PDH and the HP $^{13}$C label is transferred to $^{13}CO_2$, preventing direct detection of downstream TCA cycle metabolites. Prior animal studies using HP pyruvate with the $^{13}$C isotope enriched in the 2-position ([2-$^{13}$C]pyruvate) have successfully shown direct detection as the HP $^{13}$C labeled atoms are carried over into acetyl-CoA, a precursor to the TCA cycle, and then on to [5-$^{13}$C]glutamate (a key neurotransmitter), acetyl-carnitine and other metabolites as shown in Figure 3.1[8,9].

Motivation for this chapter included identification of novel metabolic imaging biomarkers and translation of previous protocols for molecular probes. Additional quality control experiments ensured a manufacturer of [2-$^{13}$C]pyruvate met processing qualifications in accordance with its Good Manufacturing Process (GMP) certification.

## 3.2 Biological Significance of [2-$^{13}$C]Pyruvate and TCA Cycle Metabolism

The TCA cycle is the major metabolic cellular bioenergetic pathway performing a central role in the breakdown of large organic fuel molecules such as pyruvate, glucose, and some amino acids, enabling fuel oxidation and cataplerosis for biosynthetic pathways of lipids and proteins[10].

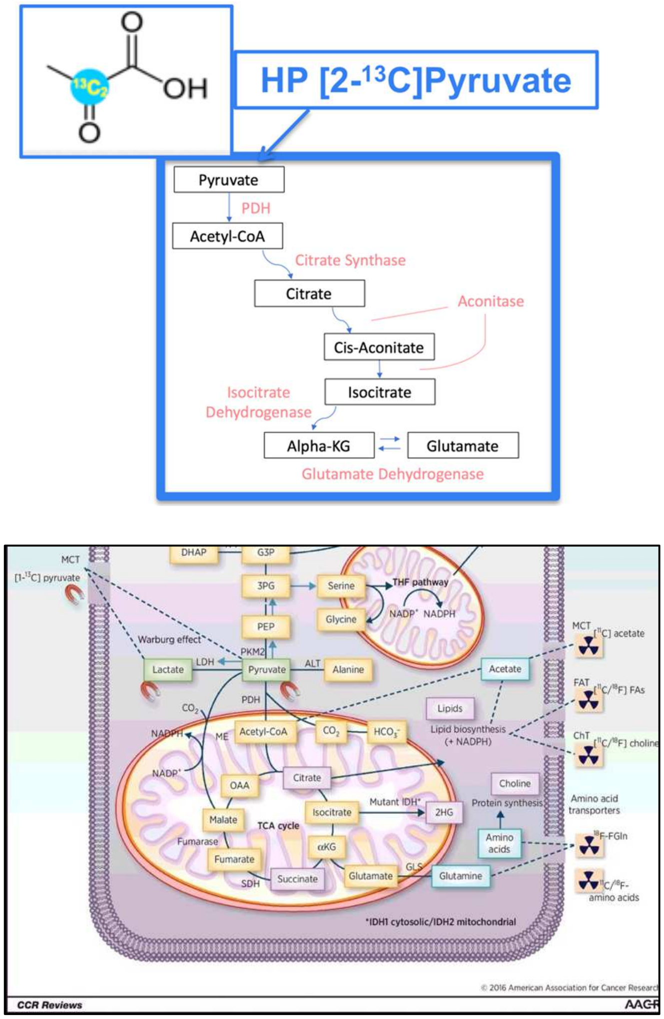

**Figure 3.2:** Diagrams highlighting intracellular [2-$^{13}$C]pyruvate metabolism. TCA cycle metabolism is detectable by HP [2-$^{13}$C]pyruvate in its conversion to [5-$^{13}$C]glutamate, but is not directly detectable with [1-$^{13}$C]pyruvate. Enzymes including pyruvate dehydrogenase (PDH) catalyzing biochemical reactions are noted. Adapted from Timm et al. [11].

Figure 3.2 illustrates [2-$^{13}$C]pyruvate metabolism along the bifurcated pathway to the TCA cycle[11]. Pyruvate is first metabolized via PDH and converted to Acetyl-CoA. This principal molecule undergoes multiple reactions in the TCA cycle as enzymes catalyze specific biochemical reactions and a single reaction would potentially release much less energy in usable form[12-14]. Acetyl-CoA is catalyzed via citrate synthase to citrate, and then to cis-aconitate and isocitrate via aconitase. Finally isocitrate dehydrogenase (IDH) is responsible for conversion to alpha-ketoglutarate (α-KG), which is converted to glutamate via glutamate dehydrogenase (GLDH) in a reversible reaction shown in Figure 3.3[12].

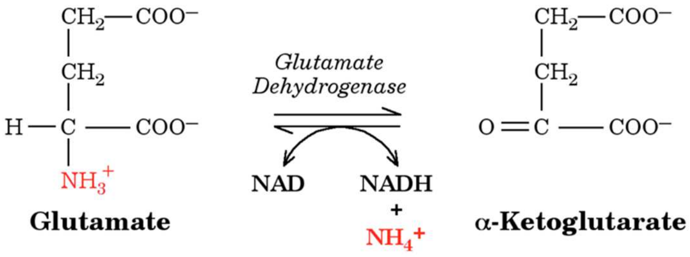

**Figure 3.3:** An essential reaction in the TCA cycle intermediate production catalyzed by GLDH. The conversion of glutamate to α-ketoglutarate and ammonia is reversible and vital in amino acid synthesis. Adapted from Brandt [12].

For this study [2-$^{13}$C]pyruvate, [2-$^{13}$C]lactate (product of anaerobic glycolytic metabolism) and [5-$^{13}$C]glutamate (neurotransmitter generated through oxidative TCA metabolism) were selected as metabolites of interest due to biological relevance and hypothesized presence of signal[14-16]. Pyruvate is the end-product of glycolysis and derived from additional sources in cellular cytoplasm. It is transported to the mitochondria where it drives ATP production by oxidative phosphorylation and multiple biosynthetic pathways. Mitochondrial pyruvate metabolism is regulated by many enzymes including PDH and pyruvate carboxylase that modulate overall pyruvate carbon flux[17].

Mono-carboxylate transporters (MCTs) are primarily responsible for transferring pyruvate and lactate from cell to cell with defining electrochemical affinities[14,15,17,20]. MCT4 is one type that regulates excretion of lactate produced by glycolysis, and it has recently been shown in cancer cells that MCT4 is upregulated and is involved in tumor growth and infiltration, and its expression is indicative of an aggressive phenotype in a number of cancers[15,18,20,21]. Lactate is a crucial indicator of cancer development, regulation, and metastasis with high MCT4 export performing a major role in creating the high lactate levels in the tumor microenvironment and is correlated with increased metastasis, tumor recurrence, and poor outcomes[21].

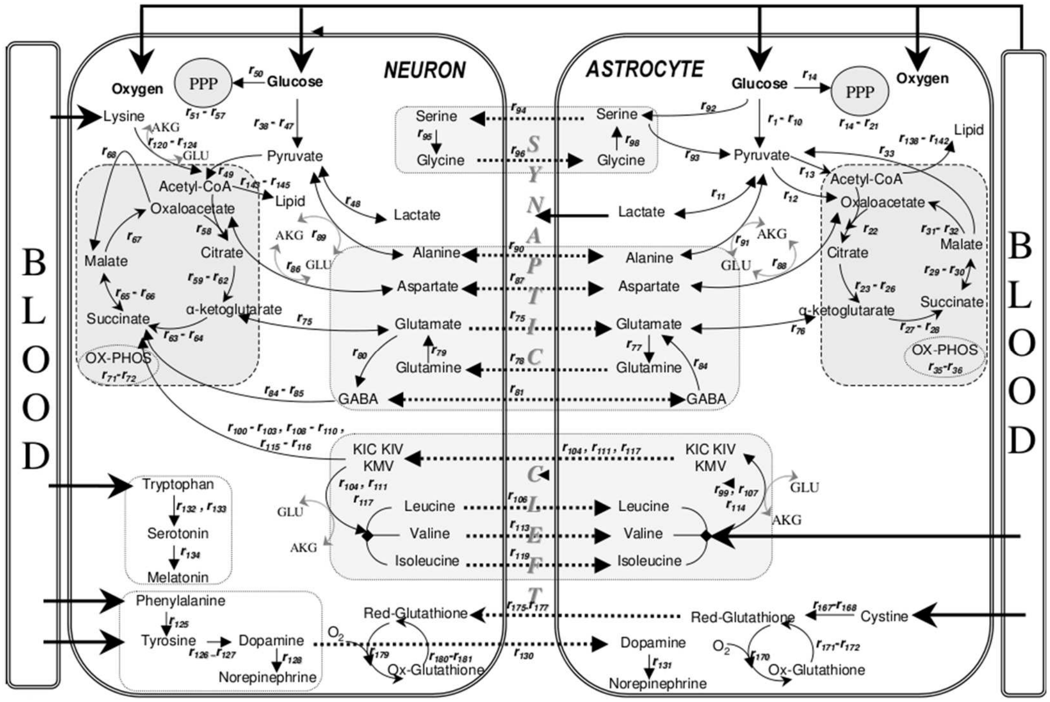

**Figure 3.4:** Metabolic interactions between astrocytes and neurons showing major reactions including glutamate (GLU) and α-ketoglutarate (α-KG). Adapted from Cakir et al. [22].

In the human brain, glutamate is the most abundant excitatory neurotransmitter with powerful transporters (GLUT) helping prevent excess activation of receptors through continuous removal from extracellular fluid[23]. Neuronal uptake of lactate makes use of MCT2 with high affinities whereas astrocyte uptake primarily functions through MCT1 and MCT4 with low affinities[24]. For *de novo* glutamate synthesis in astrocytes, oxaloacetate formed by pyruvate carboxylation condenses with acetyl-CoA and is converted to α-ketoglutarate as part of the TCA cycle and further to glutamate[25]. Depicted in Figure 3.4, astrocytes are a type of glial cell that maintain homeostasis of synapses, regulate neuronal signaling, structurally support and insulate neurons, supply nutrients and oxygen, and in aging, destroy pathogens and remove dead neurons, as well as clear neurotransmitters from the synaptic cleft and provide distinction between arrival of action potentials[13,14,22,26].

Glutamate performs a crucial role in brain development, learning and memory, with cells featuring sensitive receptors reactive to the right amount of glutamate at the right times[23]. Hence, glutamate dehydrogenase (GLDH) is a significant enzyme as it occupies a pivotal position between carbon and nitrogen metabolism[10,15,23]. The three basic types of GLDH enzymes include those cofactor-specific for NAD, for NADP, or dual co-enzyme specific for either cofactor[14].

$Na^+$-dependent excitatory amino acid transporters (EAATs) maintain low extracellular glutamate levels in the central nervous system against the concentration gradient as secondary active transporters. Several plasma membrane glutamate transporters are known to exist with varying electrochemical affinities, with high-affinity transporters including five EAATs that have been identified and cloned to date[23,27].

Glutamate can enter various metabolic pathways in accordance with cellular demand and tissue-specific function requirements[14]. In skeletal muscles, glutamate is an anaplerotic precursor of the TCA cycle for enhancing oxidative metabolism[28]. Growing tumor cells have also been found to increase the uptake and synthesis of glutamate as an alternative carbon source[14,15,24].

Data acquired in a rat brain following an injection of HP [1-$^{13}$C]ethyl pyruvate, a lipophilic probe known to cross the blood brain barrier (BBB), showed a comparable average lactate level as injecting [1-$^{13}$C]pyruvate[29]. However, toxicity was a factor limiting this HP agent. Alternatively, [2-$^{13}$C]pyruvate is non-toxic and has a strong likelihood to provide more information, due to the functional significance and biological relevance of its conversion to [2-$^{13}$C]lactate, [5-$^{13}$C]glutamate and other TCA cycle metabolites.

## 3.3 Preclinical Quality Control

**Table 3.1:** Chemical shift, *in vivo* $T_1$ and upper limit polarization values for metabolites of interest calculated in theory and taken from literature. Two chemical shift values correspond with the downfield and upfield peaks for a doublet. $T_1$ values at field strength $B_o$ = 3 T. Adapted from Bottomley et al. [16].

| Metabolite of Interest | Chemical shift (ppm) | $T_1$ (sec) | Polarization |
|---|---|---|---|
| [2-$^{13}$C]Pyruvate | 206.00 | 40 | 27% |
| [5-$^{13}$C]Glutamate | 181.8 | 10 | 25% |
| [5-$^{13}$C]Glutamine | 179.56 | - | 28% |
| [1,2-$^{13}$C]Pyruvate | 172.28 \| 170.30 | - | - |
| [2-$^{13}$C]Lactate | 72.39 \| 67.90 | 25-30 | 20% |
| [2-$^{13}$C]Pyruvate-Hydrate | 95.44 | - | - |

**Figure 3.5:** [2-$^{13}$C]Pyruvate received from Isotec Stable Isotopes of Millipore Sigma, recently approved under a GMP for human studies.

Prior to use in human studies, [2-$^{13}$C]pyruvate received from Isotec Stable Isotopes of Millipore Sigma was tested measuring $T_1$, polarization and purity to ensure it matched expectations[16]. In addition *in vivo* spectroscopy was performed in Sprague-Dawley rats to observe successful detection of metabolites[30]. Table 3.1 contains relevant expected and calculated chemical shift, $T_1$ and polarization values for reference[16].

### 3.3.1 $T_1$ and Polarization

$T_1$ and polarization were tested first. Table 3.2 summarizes QC HP experiments conducted using a HyperSense measuring $T_1$ and polarization of [2-$^{13}$C]pyruvate. $T_1$ relaxation times and liquid-state polarization levels of [2-$^{13}$C]pyruvate measured with independent characterization experiments reaffirmed literature values[16]. Total polarization over the thermal signal was determined by back-calculating from the time of injection to the start of signal acquisition. *In vivo* $T_1$ values are expected to be approximately half as measured *ex vivo*.

**Table 3.2:** Summary of QC HP experiments recording $T_1$ and polarization of [2-$^{13}$C]pyruvate with most values slightly lower yet close to expected values shown in Table 3.1. Polarization values were back-calculated using transfer time.

| Date | $T_1$ | Transfer Time | Polarization | pH |
|---|---|---|---|---|
| 05.15.2016 | 52 sec | 42.94 sec | 17.80% | 7 |
| 02.21.2017 | 51 sec | 47.63 sec | 16.36% | 5.5 |
| 03.16.2017 | 48 sec | 50.53 sec | 20.70% | 6.5 |
| 03.20.2017 | 42 sec | 45.85 sec | 10.20% | 5 |
| 05.15.2017 | 47 sec | 45.25 sec | 15.61% | 7 |

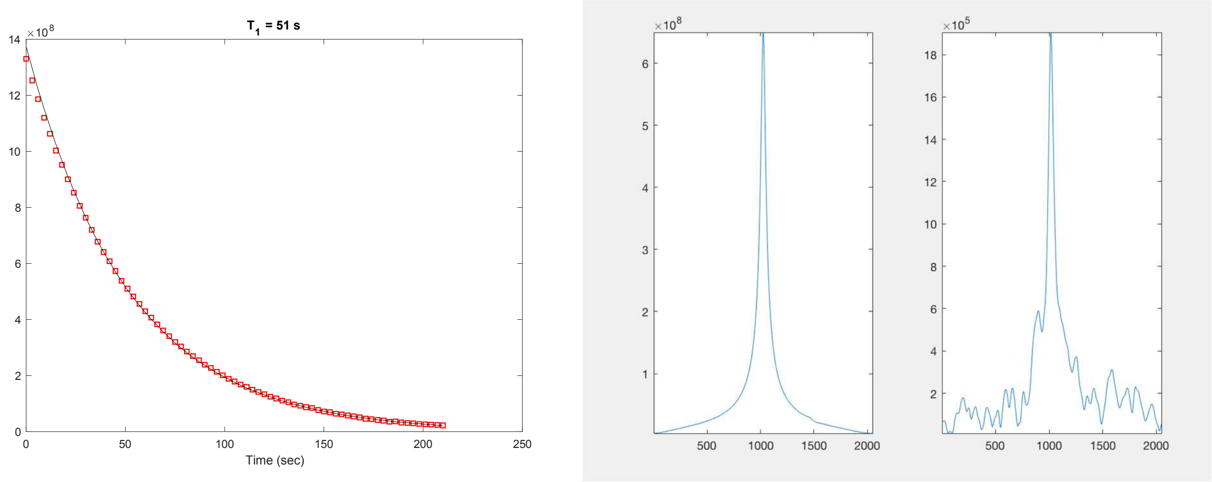

**Figure 3.6**: $T_1$ exponentially fit curve for 05.15.2016 in MATLAB (left). Polarization measurements for 05.15.2016 in MATLAB (right) using transfer times from injection to acquisition. The polarized signal is orders of magnitude higher than the thermal signal noting intensity scales verifying successful hyperpolarization.

A $^{13}C$ pulse sequence with a nonselective 500 μsec hard pulses and a flip angle $\theta = 5°$ was implemented for RF excitation. $T_1$ values were determined following exponential fitting using MATLAB. $T_1$ and polarization values were found to be in relative agreement although slightly lower than anticipated. For reference, typical polarization values for [1-$^{13}$C]pyruvate are expected about 25%[16]. Experiment #3 was found to be a primary outlier – a slightly lower pH measurement immediately following the experiment indicated a compound imbalance presumably in the dissolution process.

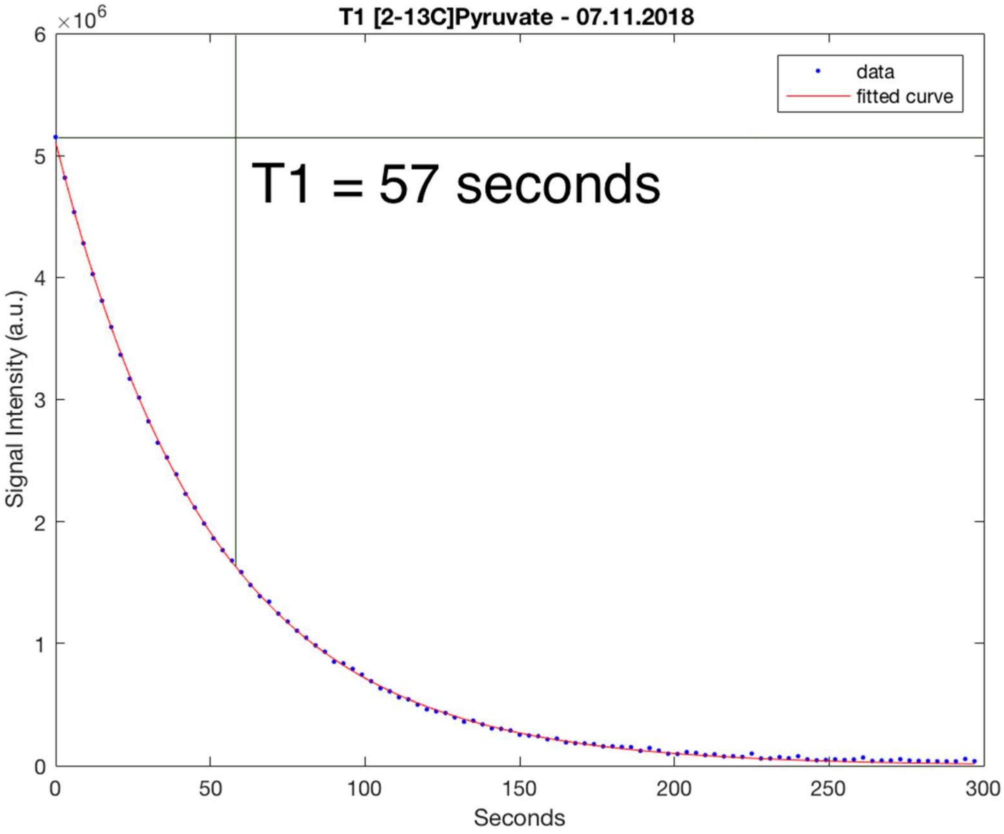

| Date | $T_1$ | Transfer Time | Polarization | pH |
|---|---|---|---|---|
| 07.11.2018 | 57 sec | 40.55 sec | 19.05% | 7 |

**Figure 3.7:** [2-$^{13}$C]pyruvate QC HP experiment measuring $T_1$ and polarization of [2-$^{13}$C]pyruvate representing a sample with reduced formic acid. The fit $T_1$ curves yielded values roughly on the order of 50 seconds, with polarization values about 17%. This is in agreement with literature values where the $T_1$ of [2-$^{13}$C]pyruvate is known to be about 10 seconds shorter than [1-$^{13}$C]pyruvate[16].

The HyperSense has a lower field of 3.35 T and operates at a higher temperature of 1.3 K than the SPINlab at 5 T and 0.77 K which may potentially contribute to slightly lower polarization values preclinically than for human studies (Eqn. 2.8).

### 3.3.2 Purity

An emerging health concern in the clinic is the potential toxicity of the gadolinium contrast agent used in traditional MRI[31]. Safety precautions similarly require $^{13}$C organic contrast agents, including C2-labeled pyruvate, to meet purity qualifications to be approved under a Good Manufacturing Process (GMP) for human studies with sterility and endotoxin testing[21].

Pyruvic acid solution NMR testing was performed using a Varian VNMRS 500 MHz (Varian Medical Systems, Palo Alto, CA) to confirm the absence of impurities. Formic acid, a naturally occurring simple carboxyl acid, and alpha-ketoglutarate (α-KG), a TCA cycle intermediate metabolite, were two peaks recorded, to which reduced amounts were confirmed in subsequent samples. Formate was measured to be reduced from 0.2967% to 0.0946% and α-KG from 0.2655% to 0.0940%.

While HP [2-$^{13}$C]pyruvate differs from the widely used HP [1-$^{13}$C]pyruvate by the position of the $^{13}$C label, many protocols for its use are identical[15].

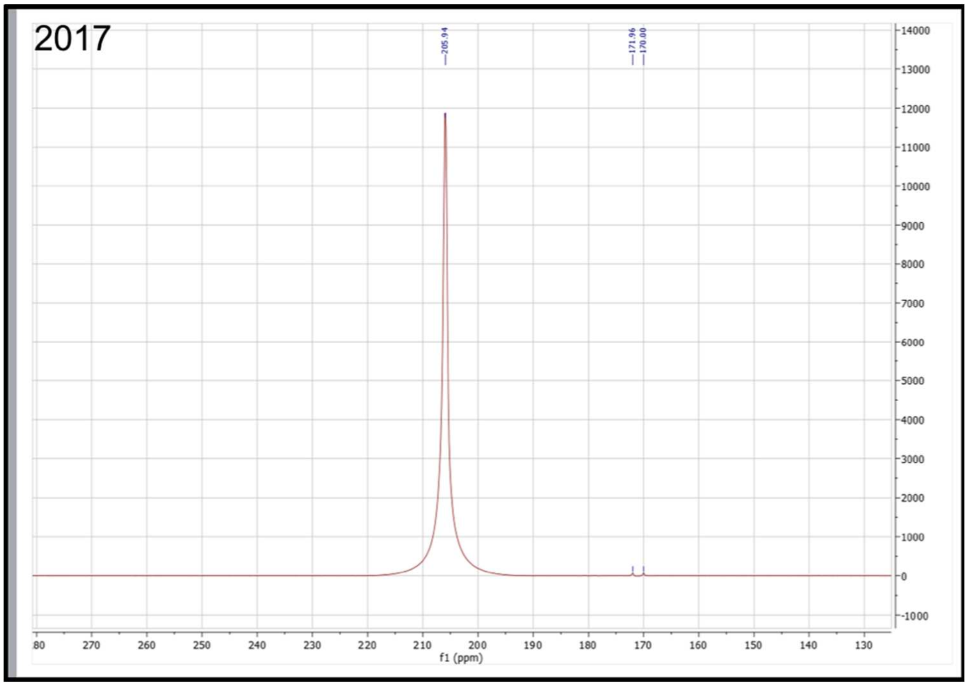

**Figure 3.8:** Pyruvic acid solution (205.94 ppm) NMR testing using a Varian VNMRS 500 MHz confirming reduced amounts of formic acid (172 ppm) and α-KG (170.0 ppm) further verifying absence of impurities.

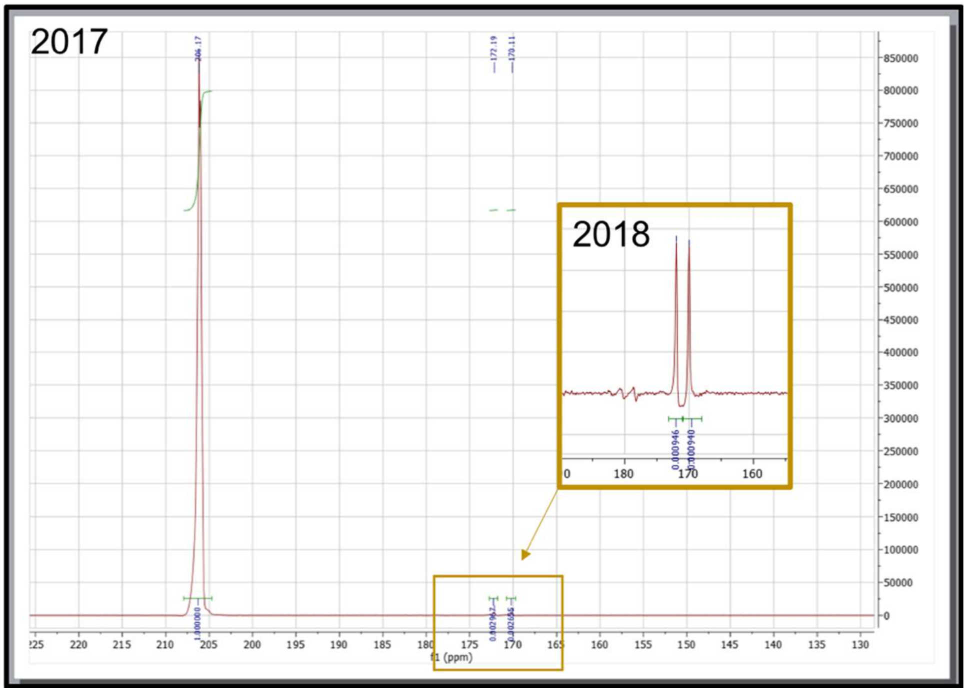

**Figure 3.9:** Subsequent 2018 samples featuring reduced impurities of formic acid (172.2 ppm) and α-KG (170.1 ppm).

### 3.3.3 *in vivo* Spectroscopy

*In vivo* spectroscopic animal studies were performed prior to human volunteer studies following Institutional Animal Care and Use Committee (IACUC) approval. Non-localized dynamic $^{13}$C NMR spectra were acquired in slabs with hard-pulsed excitation (TR/TE = 3 sec/35 msec, bandwidth = 10kHz, pulse width = 248 μsecs) on a 3T GE MR clinical scanner. Following injection, two Sprague-Dawley rats were scanned for a total of 10 scans each using a variable flip angle scheme. 4,096 total timepoints were acquired at center frequency = 32,135,355 Hz with a fixed urea phantom as reference signal. Animal breathing rates were recorded at approximately 40 breaths per minute indicating that animal vital signs remained stable. Data was processed using the UCSF software package SAGE.

[5-$^{13}$C]glutamate and [2-$^{13}$C]lactate, in addition to other possible metabolite resonances such as acetylcarnitine and acetoacetate were detected. Figure 3.8 shows characteristic peaks assigned by Park et al. from studies of HP [2-$^{13}$C]pyruvate in the murine brain[30]. The spectrum is normalized to the [2-$^{13}$C]pyruvate peak and the pyruvate doublet at 172.9 ppm is from naturally abundant $^{13}$C in the C1 position of the HP substrate.

Metabolic products of [2-$^{13}$C]pyruvate were successfully measured *in vivo* in two rats using NMR spectroscopy prior to human studies[32-34]. Figure 3.10 depict acquired spectra using SAGE following phase corrections focusing on the chemical shift range pertaining to TCA cycle metabolites. The resulting signal is believed to primarily originate from the abdomen and intestines, evidenced by the presence of glutamate, acetoacetate and acetylcarnitine. The splitting of the urea reference is potentially due to the presence of bubbles and imperfect shim corrections.

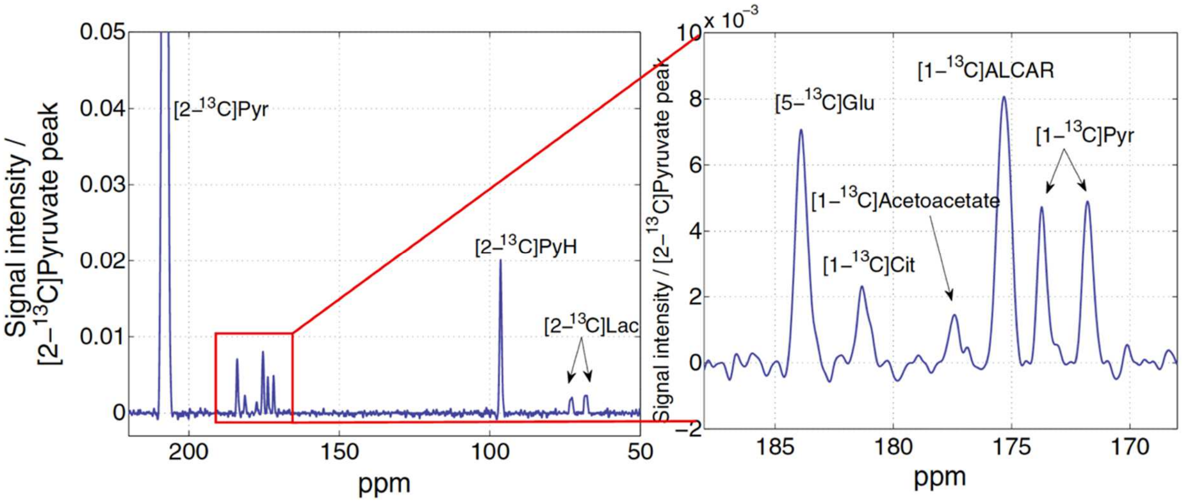

**Figure 3.10:** [2-$^{13}$C]Pyruvate NMR spectrum acquired in a murine brain with labeled characteristic peaks of [5-$^{13}$C]glutamate, [1-$^{13}$C]citrate, [1-$^{13}$C]acetoacetate, [1-$^{13}$C]acetylcarnitine and [1-$^{13}$C]pyruvate. Liquid state polarization = 25.5%, $T_1$ = 50 sec, FID spectroscopy sequence with spectral width = 10 kHz, nominal flip angle = 11.25°, TR = 3 seconds, slice thickness = 8 mm, signal time-averaged over first 20 timepoints. Adapted from Park et al. [30].

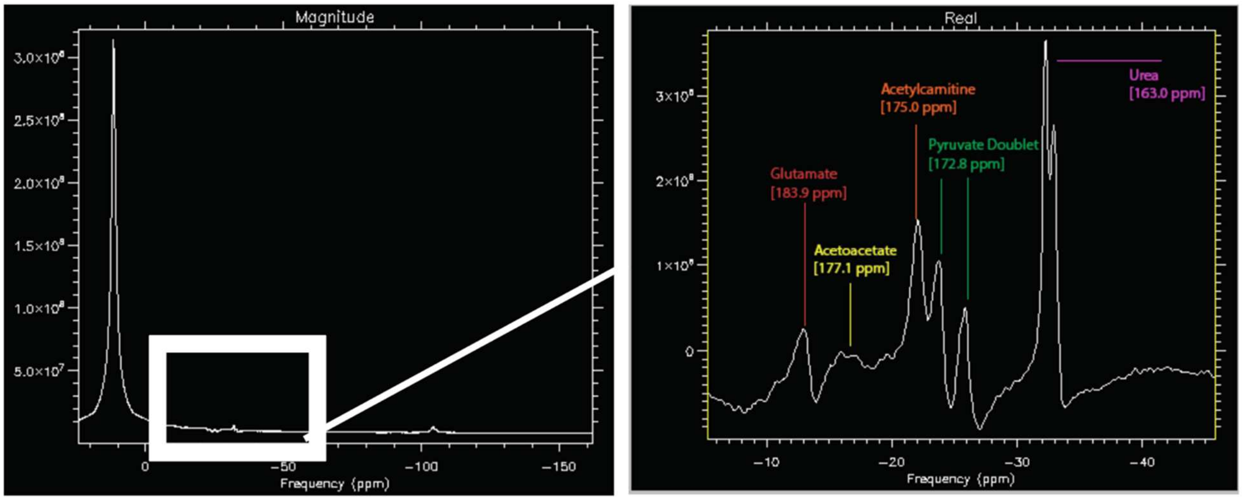

**Figure 3.11:** Non-localized test spectrum after injection of [2-$^{13}$C]pyruvate in a rat study. Peak assignments and chemical shifts were calibrated and labeled denoting approximate values with respect to [2-$^{13}$C]pyruvate's chemical shift of 207.8 ppm.

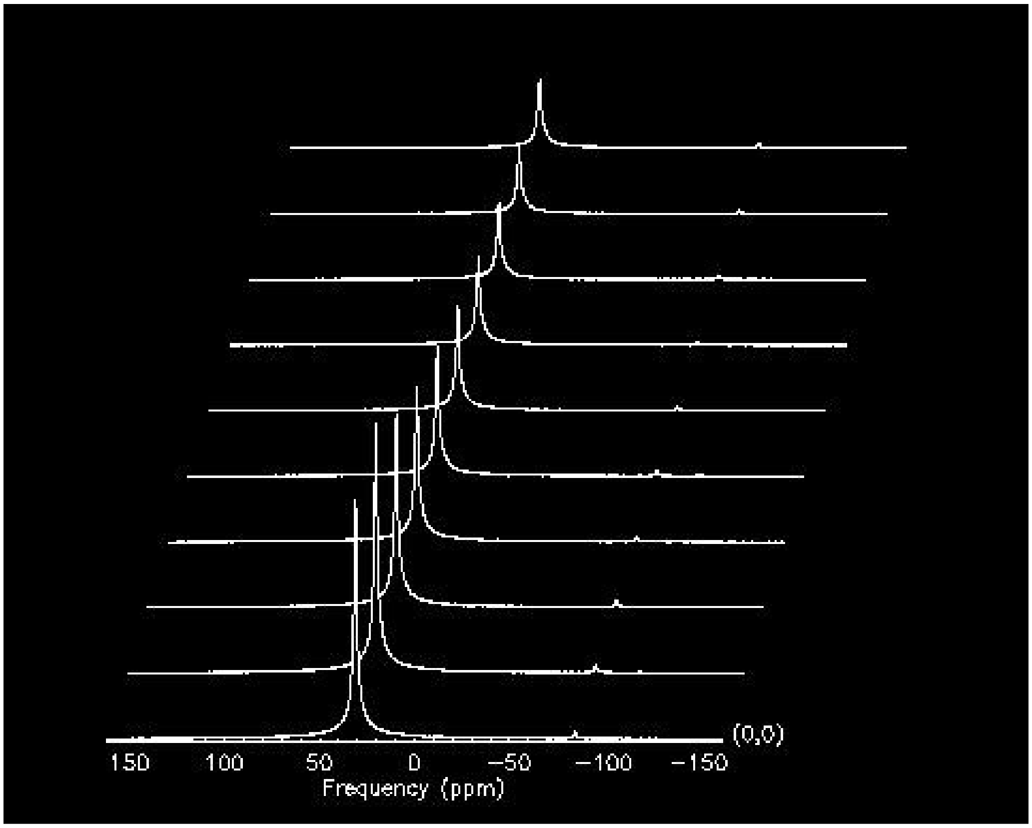

**Figure 3.12:** Polarization buildup curves. Timepoints extend into the page with frequency units (ppm) along the x-axis. Signal decay from HP compounds is unrecoverable.

In summary HP [2-$^{13}$C]pyruvate from a new specialized manufacturing process was investigated and *in vivo* metabolism was observed, demonstrating significant progress and potential for future clinical translation of this molecular probe. $T_1$ and polarization data were in accordance with expected values and [5-$^{13}$C]glutamate and other TCA cycle metabolic products were measured using NMR spectroscopy.

# References

[1] Ardenkjaer-Larsen JH, Fridlund B, Gram A, et al. Increase in signal-to-noise ratio of > 10,000 times in liquid-state NMR. Proc Natl Acad Sci U S A. 2003;100(18):10158-10163. doi:10.1073/pnas.1733835100.

[2] Ardenkjaer-Larsen JH. On the present and future of dissolution-DNP. J Magn Reson. 2016;264:3-12. doi:10.1016/j.jmr.2016.01.015.

[3] Nelson SJ, Kurhanewicz J, Vigneron DB, et al. Metabolic imaging of patients with prostate cancer using hyperpolarized [1-$^{13}$C]pyruvate. Sci Transl Med. 2013;5(198):198ra108. doi:10.1126/scitranslmed.3006070.

[4] Park I, Larson PEZ, Gordon JW, et al. Development of methods and feasibility of using hyperpolarized carbon-13 imaging data for evaluating brain metabolism in patient studies. Magn Reson Med. 2018;80(3):864-873. doi:10.1002/mrm.27077.

[5] Grist JT, McLean MA, Riemer F, et al. Quantifying normal human brain metabolism using hyperpolarized [1-13C]pyruvate and magnetic resonance imaging. Neuroimage. 2019;189:171-179. doi:10.1016/j.neuroimage.2019.01.027.

[6] Schroeder MA, Atherton HJ, Dodd MS, et al. The cycling of acetyl-coenzyme A through acetylcarnitine buffers cardiac substrate supply: a hyperpolarized 13C magnetic resonance study. Circ Cardiovasc Imaging. 2012;5(2):201-209. doi:10.1161/CIRCIMAGING.111.969451.

[7] Schroeder MA, Atherton HJ, Ball DR, et al. Real-time assessment of Krebs cycle metabolism using hyperpolarized 13C magnetic resonance spectroscopy. FASEB J. 2009;23(8):2529-2538. doi:10.1096/fj.09-129171.

[8] Albers MJ, Bok R, Chen AP, et al. Hyperpolarized 13C lactate, pyruvate, and alanine: noninvasive biomarkers for prostate cancer detection and grading. Cancer Res. 2008;68(20):8607-8615. doi:10.1158/0008-5472.CAN-08-0749.

[9] Brindle KM, Bohndiek SE, Gallagher FA, Kettunen MI. Tumor imaging using hyperpolarized 13C magnetic resonance spectroscopy. Magn Reson Med. 2011;66(2):505-519. doi:10.1002/mrm.22999.

[10] Owen OE, Kalhan SC, Hanson RW. The key role of anaplerosis and cataplerosis for citric acid cycle function. J Biol Chem. 2002;277(34):30409-30412. doi:10.1074/jbc.R200006200.

[11] Timm KN, Kennedy BW, et al. Imaging Tumor Metabolism to Assess Disease Progression and Treatment Response. Clin Cancer Res. 2016;22(21):5196-5203. doi:10.1158/1078-0432.CCR-16-0159.

[12] Brandt M. Overview of Pyruvate Metabolism. Rose-Hulman Institute of Technology. 2000.

[13] Sadock BJ, Sadock VA, Ruiz P. Kaplan & Sadock's synopsis of psychiatry: Behavioral sciences/clinical psychiatry (Eleventh edition.). Wolters Kluwer, Philadelphia, 2019.

[14] Frigerio F, Casimir M, Carobbio S, Maechler P. Tissue specificity of mitochondrial glutamate pathways and the control of metabolic homeostasis. Biochim Biophys Acta. 2008;1777(7-8):965-972. doi:10.1016/j.bbabio.2008.04.031.

[15] Le Page LM, Guglielmetti C, Taglang C, Chaumeil MM. Imaging Brain Metabolism Using Hyperpolarized 13C Magnetic Resonance Spectroscopy. Trends Neurosci. 2020;43(5):343-354. doi:10.1016/j.tins.2020.03.006.

[16] Bottomley PA, Griffiths JR, et al. Handbook of magnetic resonance spectroscopy in vivo: MRS theory, practice and applications. John Wiley & Sons, 2016.

[17] Gray LR, Tompkins SC, Taylor EB. Regulation of pyruvate metabolism and human disease. Cell Mol Life Sci. 2014;71(14):2577-2604. doi:10.1007/s00018-013-1539-2.

[18] Lim KS, Lim KJ, Price AC, Orr BA, Eberhart CG, Bar EE. Inhibition of monocarboxylate transporter-4 depletes stem-like glioblastoma cells and inhibits HIF transcriptional response in a lactate-independent manner. Oncogene. 2014;33(35):4433-4441. doi:10.1038/onc.2013.390.

[19] Birsoy K, Wang T, Possemato R, et al. MCT1-mediated transport of a toxic molecule is an effective strategy for targeting glycolytic tumors. Nat Genet. 2013;45(1):104-108. doi:10.1038/ng.2471.

[20] Park SJ, Smith CP, Wilbur RR, et al. An overview of MCT1 and MCT4 in GBM: small molecule transporters with large implications. Am J Cancer Res. 2018;8(10):1967-1976. Published 2018 Oct 1.

[21] Kurhanewicz J, Vigneron DB, Ardenkjaer-Larsen JH, et al. Hyperpolarized 13C MRI: Path to Clinical Translation in Oncology. Neoplasia. 2019;21(1):1-16. doi:10.1016/j.neo.2018.09.006.

[22] Cakir T, Alsan S, Saybaşili H, Akin A, Ulgen KO. Reconstruction and flux analysis of coupling between metabolic pathways of astrocytes and neurons: application to cerebral hypoxia. Theor Biol Med Model. 2007;4:48. Published 2007 Dec 10. doi:10.1186/1742-4682-4-48.

[23] Zhou Y, Danbolt NC. Glutamate as a neurotransmitter in the healthy brain. J Neural Transm (Vienna). 2014;121(8):799-817. doi:10.1007/s00702-014-1180-8.

[24] Falkowska A, Gutowska I, Goschorska M, Nowacki P, Chlubek D, Baranowska-Bosiacka I. Energy Metabolism of the Brain, Including the Cooperation between Astrocytes and Neurons, Especially in the Context of Glycogen Metabolism. Int J Mol Sci. 2015;16(11):25959-25981. Published 2015 Oct 29. doi:10.3390/ijms161125939.

[25] Shen J, Tomar JS. Elevated Brain Glutamate Levels in Bipolar Disorder and Pyruvate Carboxylase-Mediated Anaplerosis. Front Psychiatry. 2021;12:640977. Published 2021 Feb 23. doi:10.3389/fpsyt.2021.640977.

[26] Siracusa R, Fusco R, Cuzzocrea S. Astrocytes: Role and Functions in Brain Pathologies. Front Pharmacol. 2019;10:1114. Published 2019 Sep 27. doi:10.3389/fphar.2019.01114.

[27] Magi S, Piccirillo S, Amoroso S, Lariccia V. Excitatory Amino Acid Transporters (EAATs): Glutamate Transport and Beyond. Int J Mol Sci. 2019;20(22):5674. Published 2019 Nov 13. doi:10.3390/ijms20225674.

[28] Rennie MJ, Bowtell JL, Bruce M, Khogali SE. Interaction between glutamine availability and metabolism of glycogen, tricarboxylic acid cycle intermediates and glutathione. J Nutr. 2001;131(9 Suppl):2488S-7S. doi:10.1093/jn/131.9.2488S.

[29] Hurd RE, Yen YF, Mayer D, et al. Metabolic imaging in the anesthetized rat brain using hyperpolarized [1-13C] pyruvate and [1-13C] ethyl pyruvate. Magn Reson Med. 2010;63(5):1137-1143. doi:10.1002/mrm.22364.

[30] Park JM, Josan S, Grafendorfer T, et al. Measuring mitochondrial metabolism in rat brain in vivo using MR Spectroscopy of hyperpolarized [2-$^{13}$C]pyruvate. NMR Biomed. 2013;26(10):1197-1203. doi:10.1002/nbm.2935.

[31] Rogosnitzky M, Branch S. Gadolinium-based contrast agent toxicity: a review of known and proposed mechanisms. Biometals. 2016;29(3):365-376. doi:10.1007/s10534-016-9931-7.

[32] Hu S, Yoshihara HA, Bok R, et al. Use of hyperpolarized [1-13C]pyruvate and [2-13C]pyruvate to probe the effects of the anticancer agent dichloroacetate on mitochondrial metabolism in vivo in the normal rat. Magn Reson Imaging. 2012;30(10):1367-1372. doi:10.1016/j.mri.2012.05.012.

[33] Von Morze C, Larson PE, Hu S, et al. Investigating tumor perfusion and metabolism using multiple hyperpolarized (13)C compounds: HP001, pyruvate and urea. Magn Reson Imaging. 2012;30(3):305-311. doi:10.1016/j.mri.2011.09.026.

[34] Milshteyn E, von Morze C, Reed GD, et al. Development of high resolution 3D hyperpolarized carbon-13 MR molecular imaging techniques. Magn Reson Imaging. 2017;38:152-162. doi:10.1016/j.mri.2017.01.003.

# Chapter 4

# First HP [2-$^{13}$C]Pyruvate MR Studies of Human Brain Metabolism

*Chung BT, Chen HY, Gordon J, Mammoli D, Sriram R, Autry AW, Le Page LM, Chaumeil MM, Shin P, Slater J, Tan CT, Suszczynski C, Chang S, Li Y, Bok RA, Ronen SM, Larson PEZ, Kurhanewicz J, Vigneron DB. First hyperpolarized [2-13C]pyruvate MR studies of human brain metabolism. J Magn Reson. Dec 2019. doi: 10.1016/j.jmr.2019.106617.*

## 4.1 Abstract & Introduction

Methods for the preparation of hyperpolarized (HP) sterile [2-$^{13}$C]pyruvate were developed to test its feasibility in first-ever human NMR studies following FDA-IND & IRB approval. Spectral results using this MR stable-isotope imaging approach demonstrated the feasibility of investigating human cerebral energy metabolism by measuring the dynamic conversion of HP [2-$^{13}$C]pyruvate to [2-$^{13}$C]lactate and [5-$^{13}$C]glutamate in the brain of four healthy volunteers. Metabolite kinetics, signal-to-noise (SNR) and area-under-curve (AUC) ratios, and calculated [2-$^{13}$C]pyruvate to [2-$^{13}$C]lactate conversion rates ($k_{PL}$) were measured and showed similar but not identical inter-subject values. The $k_{PL}$ measurements were equivalent with prior human HP [1-$^{13}$C]pyruvate measurements.

HP [2-$^{13}$C]pyruvate provides novel metabolic information different from HP [1-$^{13}$C]pyruvate due to its unique positioning atop multiple anaplerotic and cataplerotic metabolic cascades in the TCA cycle with known fast conversions[1]. Prior preclinical studies have shown differences in [2-$^{13}$C]pyruvate to [5-$^{13}$C]glutamate metabolism with isocitrate dehydrogenase (IDH) mutations in brain tumor models not detected by HP [1-$^{13}$C]pyruvate MR[2].

The goal of this study was to develop methods for the hyperpolarization and preparation of sterile [2-$^{13}$C]pyruvate with FDA-IND and IRB approval for first-ever human studies[3]. We sought to investigate HP [2-$^{13}$C]pyruvate conversion to [2-$^{13}$C]lactate and [5-$^{13}$C]glutamate in the normal brain in four volunteers, demonstrating a significant first step for HP metabolic imaging to diagnose neurological disorders potentially at an early stage and monitor treatment response. Unlike animal studies, the human experiments were performed without anesthesia that significantly reduces brain pyruvate metabolism[4].

## 4.2 Experimental Methods

### 4.2.1 [2-$^{13}$C]Pyruvate: FDA-IND, IRB, Human Volunteers

[2-$^{13}$C]pyruvate was produced by MilliporeSigma Isotec Stable Isotopes (Miamisburg, OH) following GMP for first-ever use in human HP MR studies. All human studies followed an IRB and FDA IND-approved protocol with informed consent. Proton T2-FLAIR anatomical reference imaging scans showed volunteers had no acute abnormalities.

### 4.2.2 Clinical Preparation: Hyperpolarization, SPINlab

A 1.46 g sample of 14 M 99% enriched [2-$^{13}$C]-labeled pyruvic acid (Millipore-Sigma, Miamisburg, OH) mixed with 15 mM trityl radical[5] (GE Healthcare, Oslo, Norway) was pre-filled in a single-use, pharma-kit polymer fluid pathway and polarized for over 2 hours in a SPINlab polarizer (General Electric, Niskayuna, NY) operating at 5 Tesla and 0.77 Kelvin, with microwave irradiation frequency in the 94.0 - 94.1 GHz band.

Following the protocol approved by the University of California San Francisco IRB and the FDA IND, and after dissolution and meeting all quality control specifications and pharmacist approval, 0.43 mL/kg of the hyperpolarized pyruvate solution (250 mM) was injected intravenously at a rate of 5 mL/s using a power injector (Medrad Inc., Warrendale, PA) followed by 20 mL of sterile saline.

### 4.2.3 MR Protocol

Volunteers were measured using a 3T MR scanner (MR750, 50 mT/m gradient amplitude, 200 T/m/s slew rate; GE Healthcare, Waukesha, WI) and scanned with a volume excitation and 32-channel receive $^{13}$C array coil for brain studies[6]. A 400 μsec hard pulse excitation provided an approximately 2.5 kHz excitation bandwidth, with a nominal flip angle of 40° at the center frequency of 141 ppm calibrated using a built-in urea phantom. The [2-$^{13}$C]pyruvate, [5-$^{13}$C]glutamate, and [2-$^{13}$C]lactate doublet resonances were excited with 7°, 30°, 5° and 2.1° flip angles respectively. The acquisition used temporal and spectral resolutions of 2 sec and 2.4 Hz across 30 timepoints for a total scan time of 2 minutes.

### 4.2.4 Data Analysis

Dynamic spectroscopic data yielding kinetic rates and curves was reconstructed after zero-filling free induction decays. The 32-channel data was combined with a phase-sensitive summation followed by line broadening of 5 Hz[7].

For the pyruvate-to-lactate conversion ($k_{PL}$) kinetic model, the measured pyruvate magnetization functioned as the input for fitting the lactate magnetization. The MATLAB model was solved based on minimization of a constrained least-squares error computed across measured and estimated lactate using a trust-region-reflective algorithm. The input-less fitting was chosen over integral ratios due to improved accuracy by accounting for variability in delivery times[8]. Analytical methods are available from the Hyperpolarized MRI Toolbox via the Hyperpolarized Technology Resource Center[9].

Quantitative data processing and display were achieved using MATLAB (The MathWorks Inc., Natick, MA) and MestReNova (Mestrelab, Santiago de Compostela, Spain). Zero- and first-order phase corrections were performed, and baseline was subtracted by fitting a spline to signal-free regions of the smoothed spectrum. Metabolites of interest were quantified following prior assignments by selecting and integrating across peak boundaries[10]. Single timepoint data 16 seconds following injection was further analyzed and interpreted following singular value decomposition (SVD) signal enhancement techniques[8,11-13].

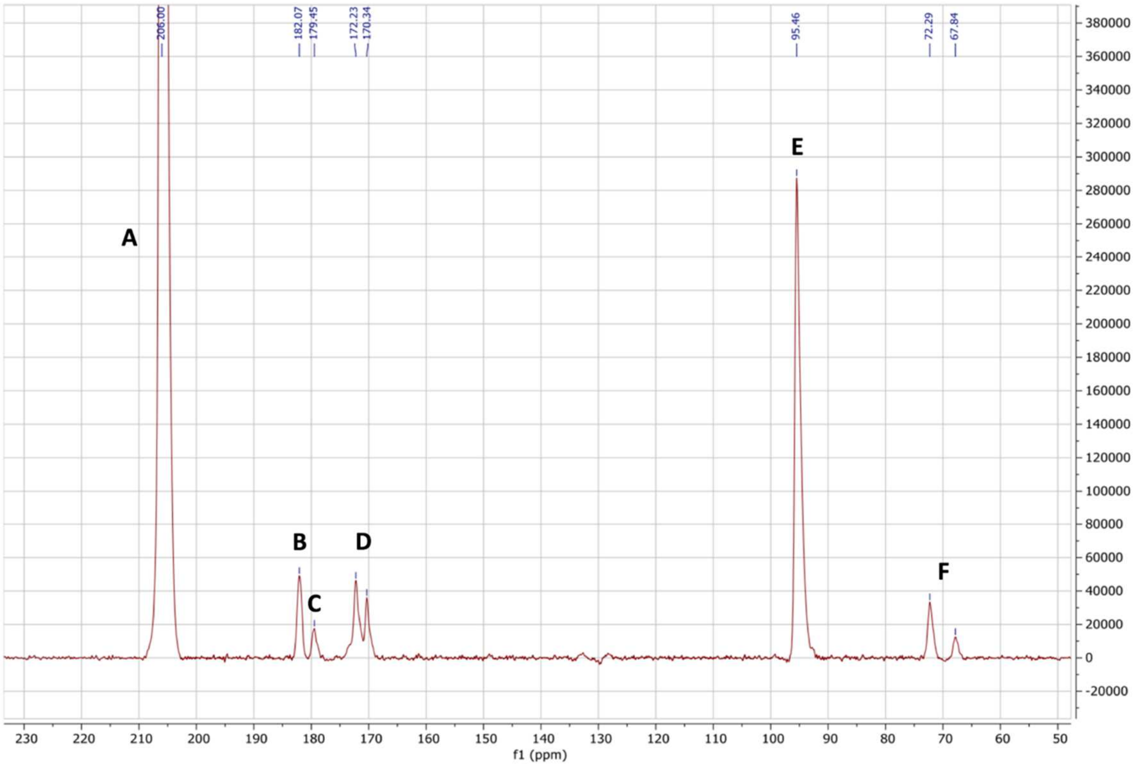

**Figure 4.1**: Representative Carbon-13 NMR summed spectrum from the brain of a healthy volunteer acquired with a 32-channel head coil following an injection of 1.43 mL/kg of 250mM [2-$^{13}$C]pyruvate. Peak identification was assigned following those by Park et al. from studies of HP [2-$^{13}$C]pyruvate in the murine brain[10]: A) [2-$^{13}$C]pyruvate, B) [5-$^{13}$C]glutamate, C) [1-$^{13}$C]citrate and/or [5-$^{13}$C]glutamine, D) [1-$^{13}$C]pyruvate (natural abundance doublet), E) [2-$^{13}$C]pyruvate-hydrate, F) [2-$^{13}$C]lactate doublet.

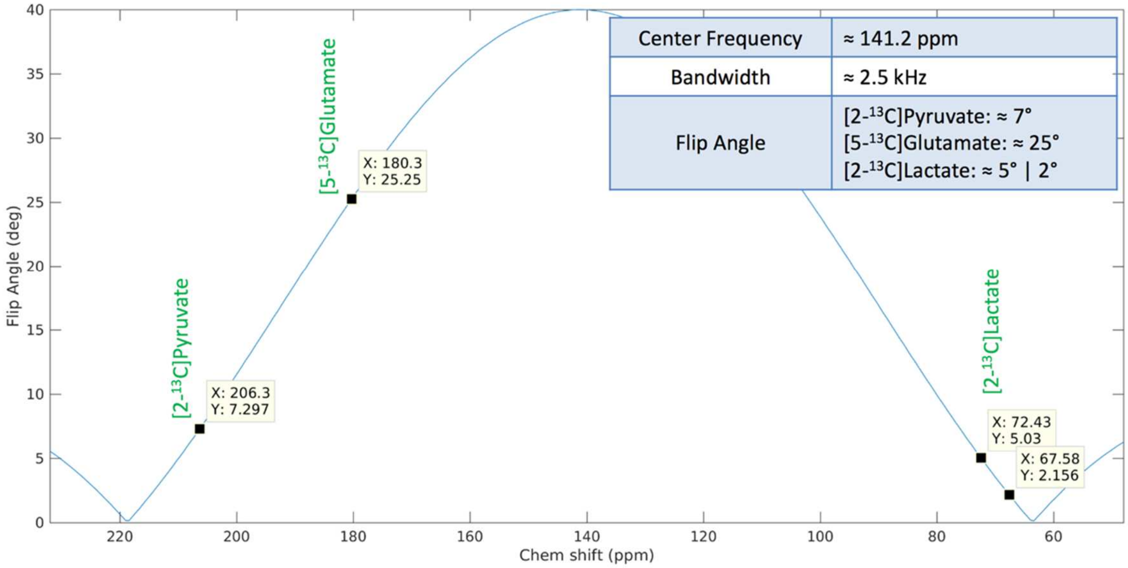

| Center Frequency | ≈ 141.2 ppm |
|---|---|
| Bandwidth | ≈ 2.5 kHz |
| Flip Angle | [2-$^{13}$C]Pyruvate: ≈ 7°<br>[5-$^{13}$C]Glutamate: ≈ 25°<br>[2-$^{13}$C]Lactate: ≈ 5° \| 2° |

**Figure 4.2**: Flip angle plot of the RF excitation pulse sequence with parameters used for this study. Note the decreased excitation of the upfield [2-$^{13}$C]lactate resonance versus the downfield by approximately one half.

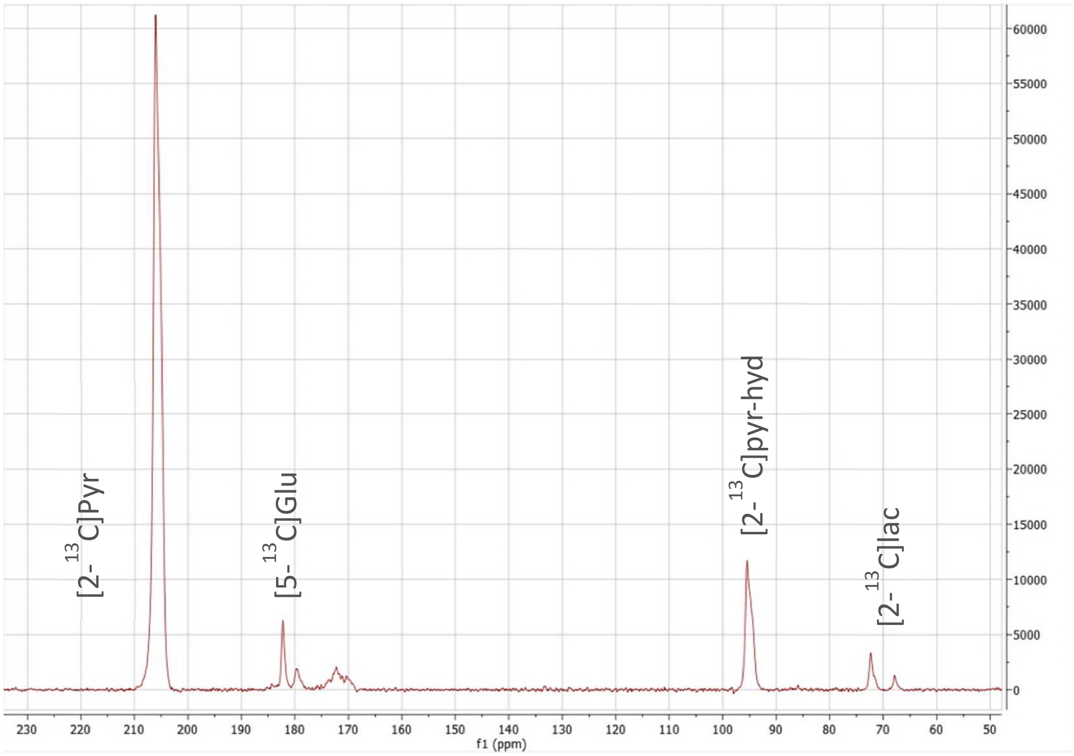
[2-$^{13}$C]Pyr
[5-$^{13}$C]Glu
[2-$^{13}$C]pyr-hyd
[2-$^{13}$C]lac
60000
55000
50000
45000
40000
35000
30000
25000
20000
15000
10000
5000
0
230
220
210
200
190
180
170
160
150
140
130
120
110
100
90
80
70
60
50
f1 (ppm)

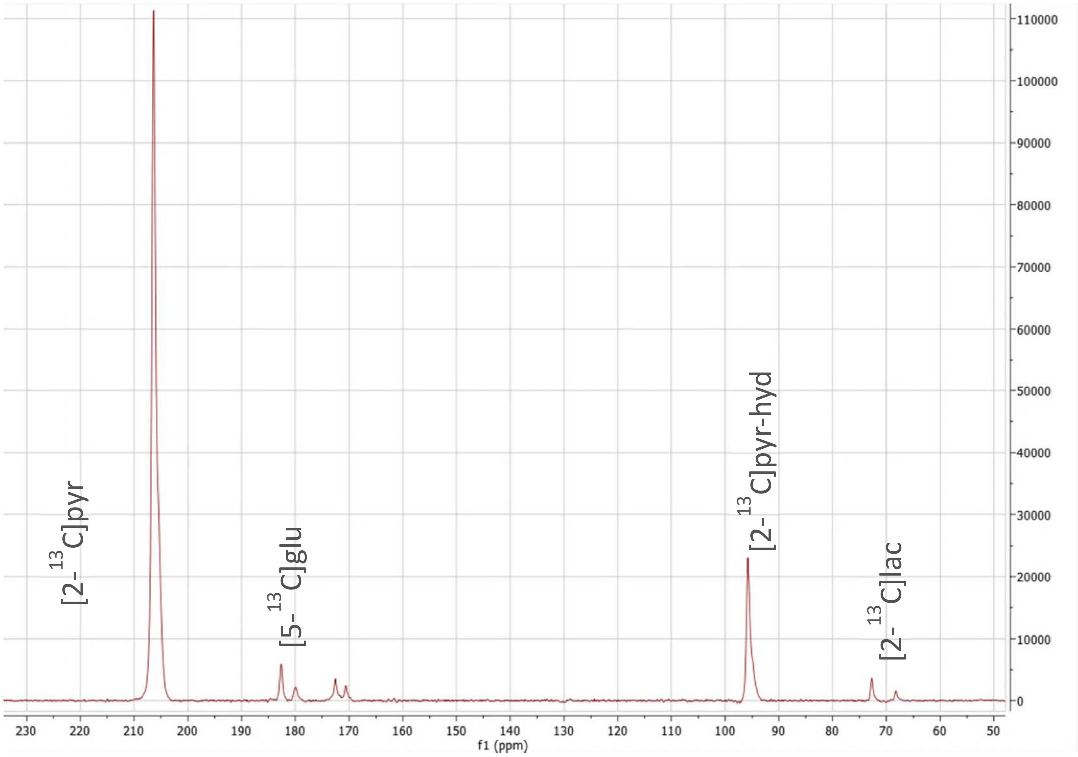
[2-$^{13}$C]pyr
[5-$^{13}$C]glu
[2-$^{13}$C]pyr-hyd
[2-$^{13}$C]lac
110000
100000
90000
80000
70000
60000
50000
40000
30000
20000
10000
0
230
220
210
200
190
180
170
160
150
140
130
120
110
100
90
80
70
60
50
f1 (ppm)

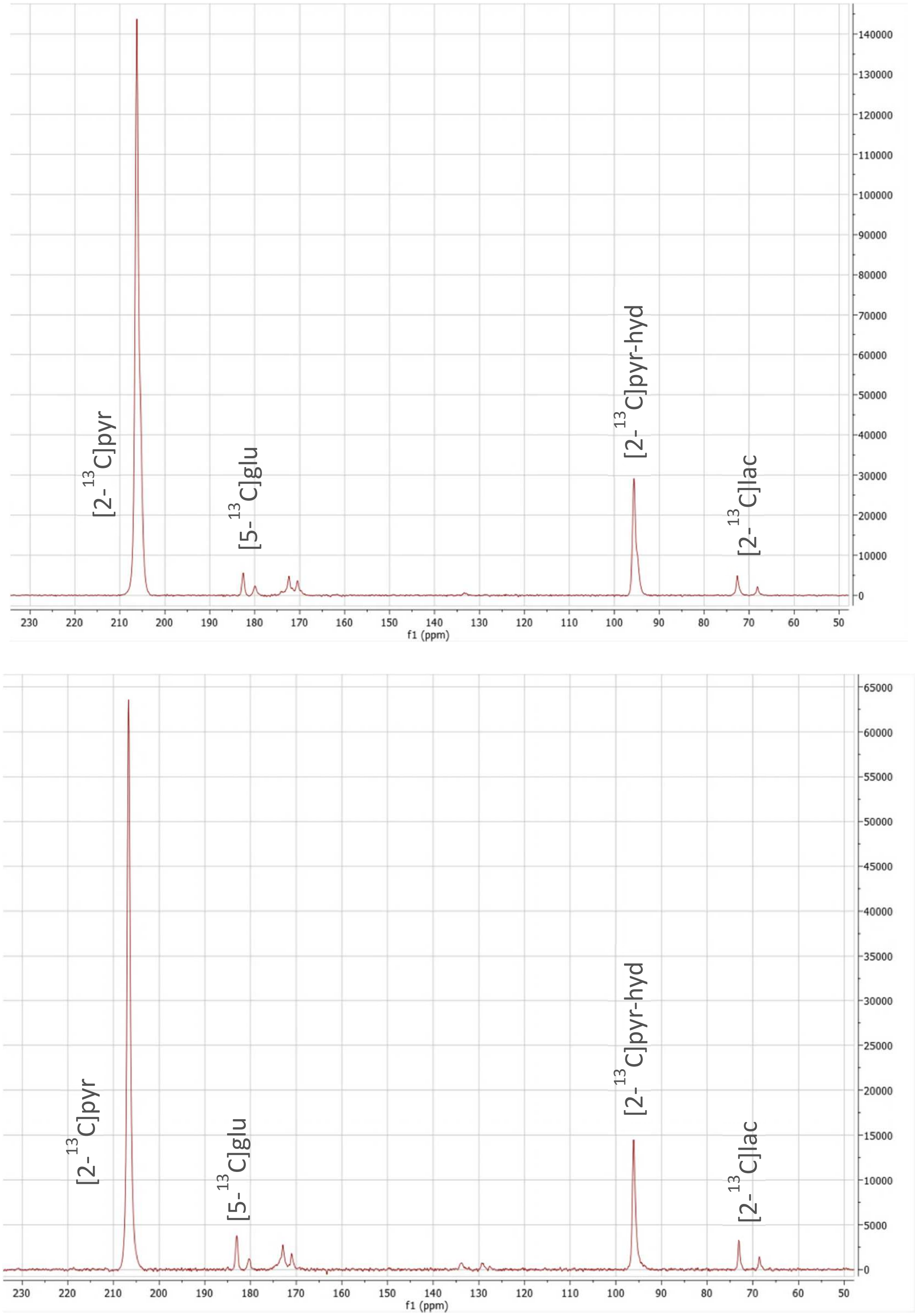

**Figure 4.3**: Spectra for four volunteers at a single timepoint 16 seconds post-injection. Similar levels of [5-$^{13}$C]glutamate and [2-$^{13}$C]lactate reflect the underlying biochemistry of the healthy human brain of similar rates of conversion of [2-$^{13}$C]pyruvate to [2-$^{13}$C]lactate catalyzed by LDH as [2-$^{13}$C]pyruvate to [5-$^{13}$C]glutamate catalyzed by PDH.

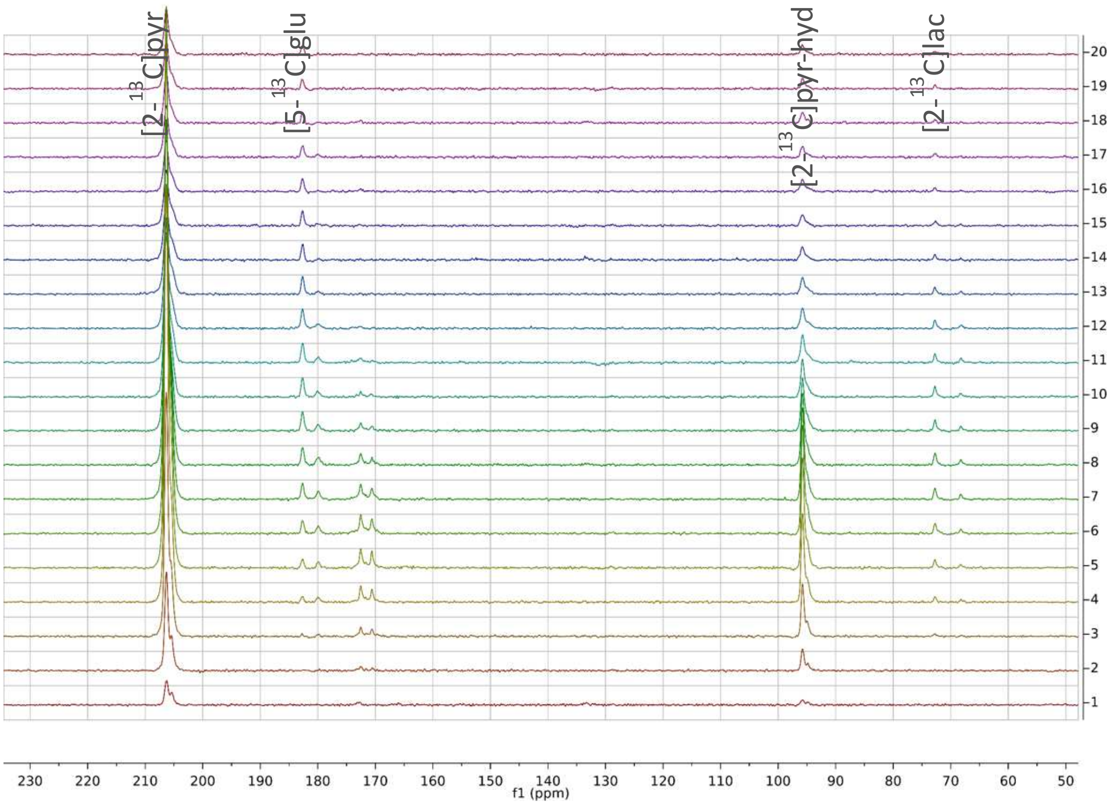

**Figure 4.4:** Time dynamics illustrating rapid conversion of metabolites. As shown in the corresponding Figure 4.3, the rates of conversion of [2-$^{13}$C]pyruvate to [5-$^{13}$C]glutamate are similar in the normal human brain.

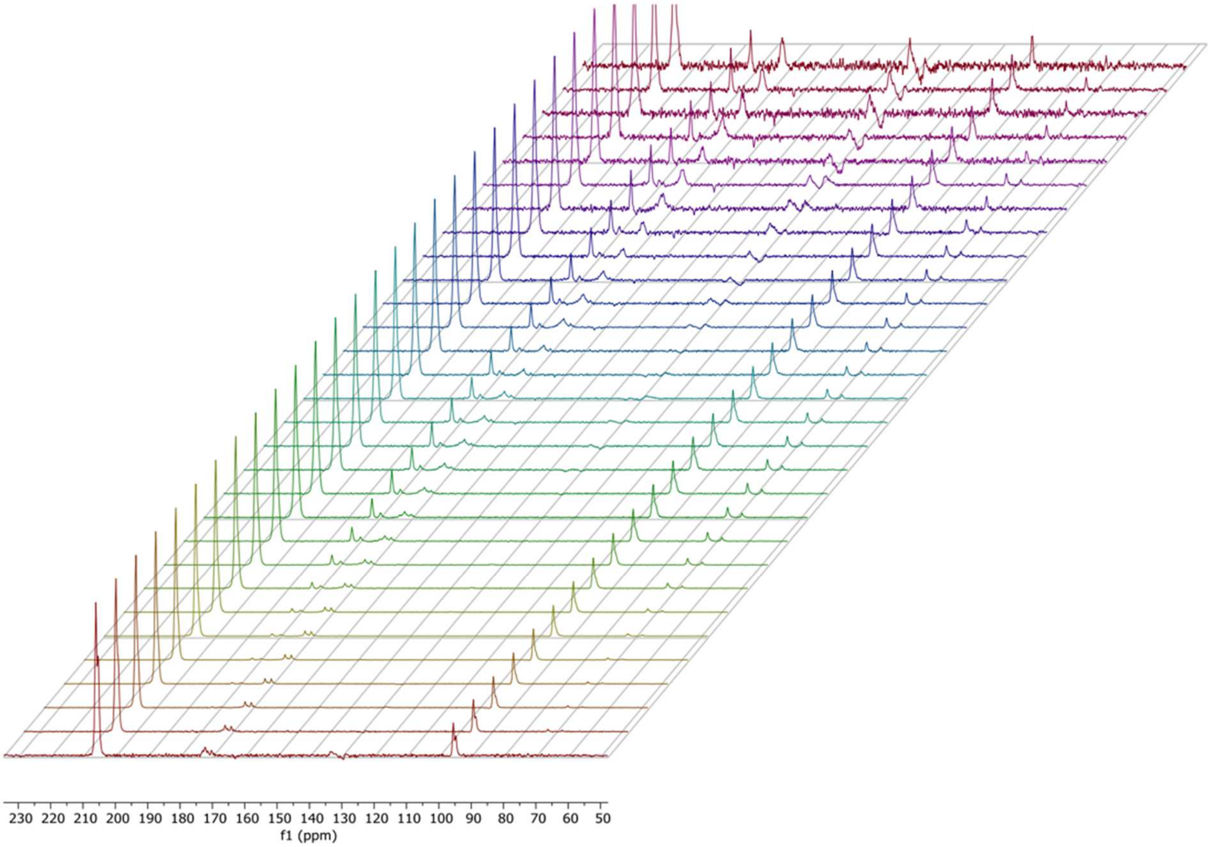

**Figure 4.5**: Time dynamics illustrating rapid conversion of metabolites. From this rotated orientation, we clearly observe the rise and decay of metabolic signals, highlighting the significant benefit hyperpolarization grants us in drastically increasing the SNR of TCA cycle intermediate metabolites to observe kinetics.

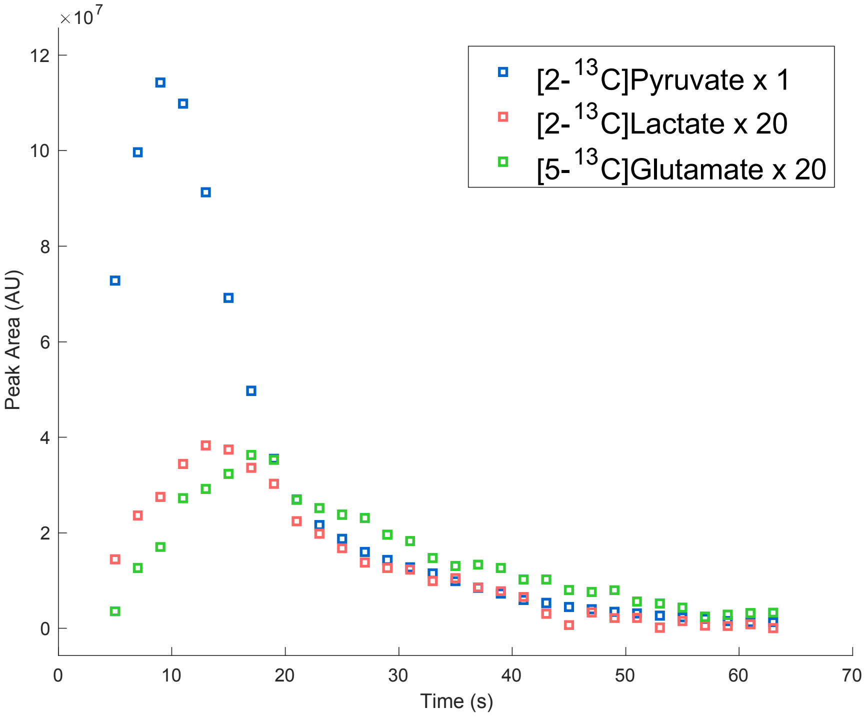
×10^7
12
10
8
6
4
2
0
Peak Area (AU)
0
10
20
30
40
50
60
70
Time (s)
[2-13C]Pyruvate x 1
[2-13C]Lactate x 20
[5-13C]Glutamate x 20

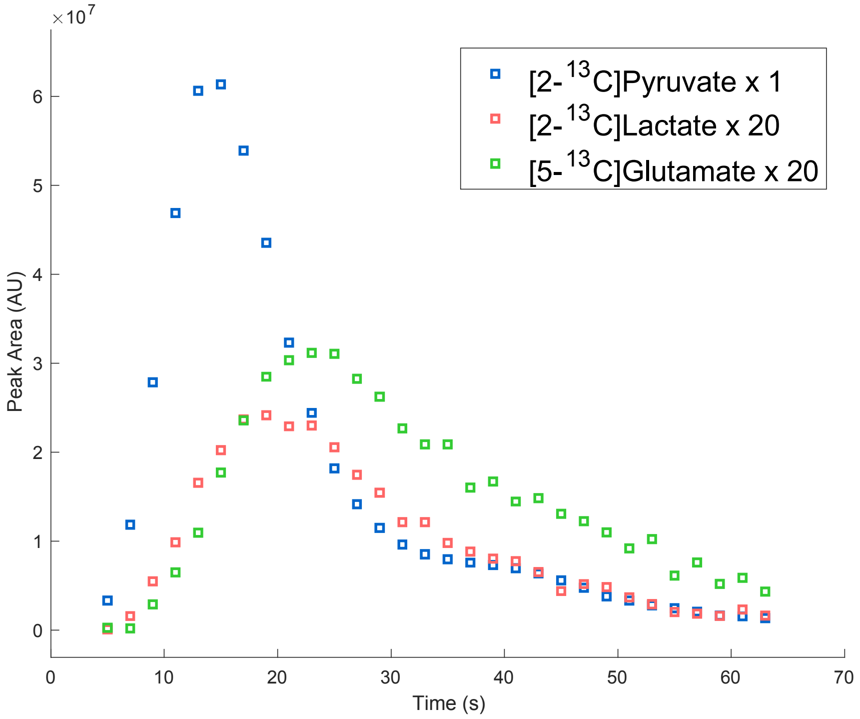
×10^7
6
5
4
3
2
1
0
Peak Area (AU)
0
10
20
30
40
50
60
70
Time (s)
[2-13C]Pyruvate x 1
[2-13C]Lactate x 20
[5-13C]Glutamate x 20

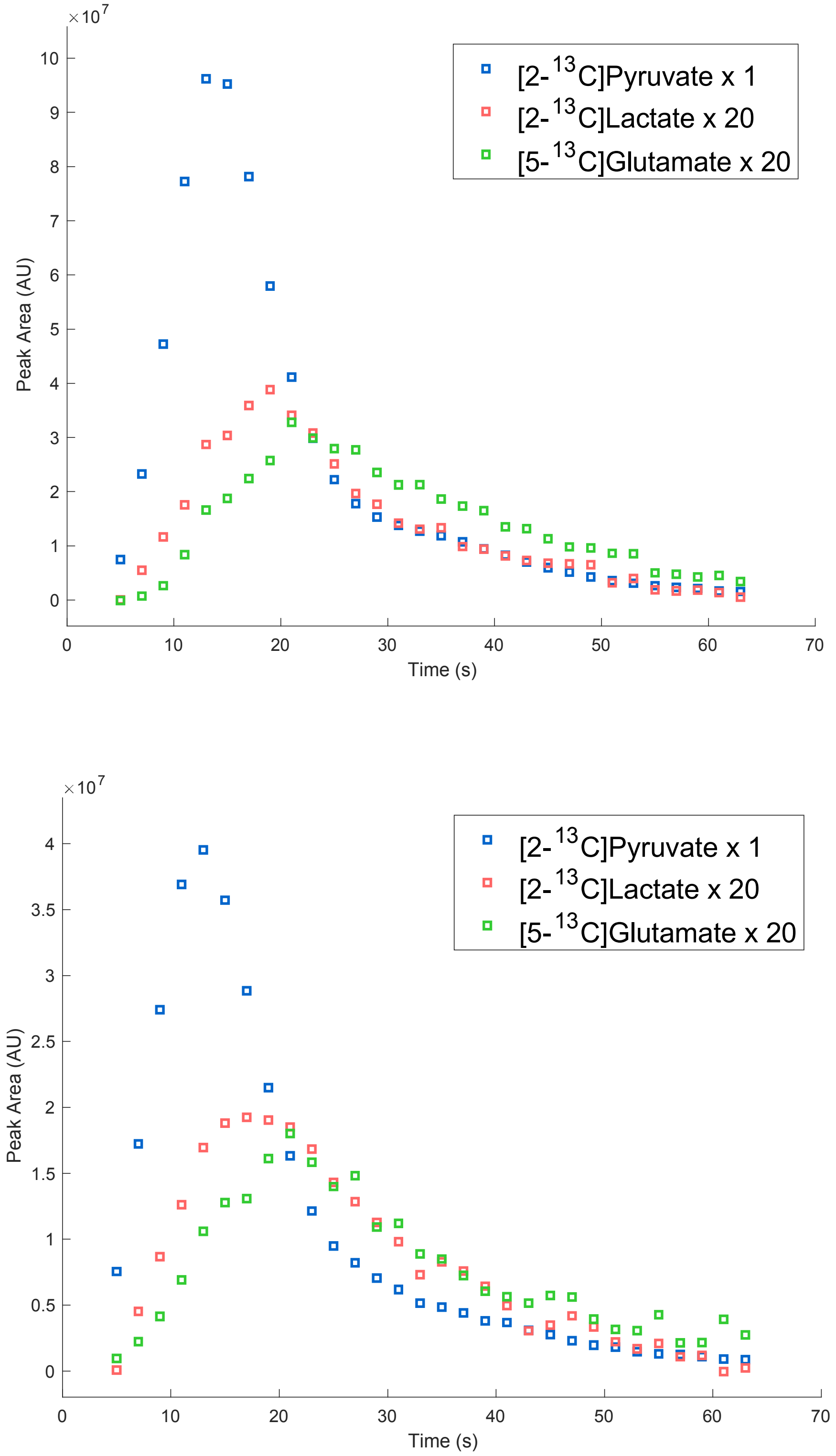

**Figure 4.6**: Dynamic plots of metabolite kinetics from four volunteers. Results were consistent noting minor differences in intensity scale.

# 4.3 Experimental Results

## 4.3.1 Volunteer Spectra

HP [2-$^{13}$C]pyruvate, [2-$^{13}$C]lactate, [5-$^{13}$C]glutamate and other metabolites were successfully observed and quantitatively measured for the first time in four volunteers. Figure 4.1 shows a representative summed spectra over the total 2 min scantime for a healthy volunteer using a pulse and acquire scheme with the RF profile shown in Figure 4.2. Figures 4.3, 4.4, 4.5 and 4.6 depict spectra and kinetics of measured metabolite resonances.

**Table 4.1:** SNR for each volunteer from a single timepoint 16 seconds post-injection with calculated mean and standard error.

| Volunteer | [2-$^{13}$C]Pyr | [5-$^{13}$C]Glu | [2-$^{13}$C]Pyr-Hyd | [2-$^{13}$C]Lac (Left Peak) | [2-$^{13}$C]Lac (Right Peak) |
|---|---|---|---|---|---|
| 1 | 885.93 | 91.18 | 169.68 | 24.63 | 9.55 |
| 2 | 1278.34 | 68.36 | 265.33 | 42.58 | 18.55 |
| 3 | 2114.06 | 83.03 | 428.07 | 72.67 | 32.95 |
| 4 | 964.09 | 57.43 | 219.63 | 50.93 | 22.05 |
| Mean | 1310.61 ± 486.57 | 75.00 ± 13.03 | 270.68 ± 96.96 | 47.70 ± 17.27 | 20.77 ± 8.38 |

**Table 4.2:** AUC metabolite ratios for each volunteer summed across all timepoints with calculated mean and standard error.

| Volunteer | Lac / Pyr | Glu / Pyr | Pyr-Hyd / Pyr | Glu / Lac |
|---|---|---|---|---|
| 1 | 0.024 | 0.027 | 0.163 | 1.125 |
| 2 | 0.030 | 0.045 | 0.178 | 1.500 |
| 3 | 0.028 | 0.030 | 0.180 | 1.071 |
| 4 | 0.038 | 0.037 | 0.191 | 0.974 |
| Mean | $0.030 \pm 0.005$ | $0.035 \pm 0.007$ | $0.178 \pm 0.010$ | $1.168 \pm 0.199$ |

## 4.3.2 SNR & Metabolite Ratios

Tables 4.1 and 4.2 summarize measured SNR from the single timepoint data and AUC metabolite ratios summed across all timepoints for the 4 volunteers. Measured values and calculated mean and standard error across volunteers were consistent within expected ranges[5]. The observed variations in SNR can be attributed to multiple factors including brain volumes, polarization values, and delivery times from the polarizer to the subject. These demonstrated however minimal effects on the ratios and kinetic values that showed tight agreement between volunteers. The third volunteer dataset showed the highest SNR with AUC ratios near median and was hence selected as the representative spectrum for peak identification in Figure 4.1. The [2-$^{13}$C]lactate (left and right peaks) correspond to the left and right resonances of the [2-$^{13}$C]lactate doublet in the $^{13}$C MRS spectra. The left (downfield) resonance is about two-fold higher due to the excitation profile shown in Figure 4.2.

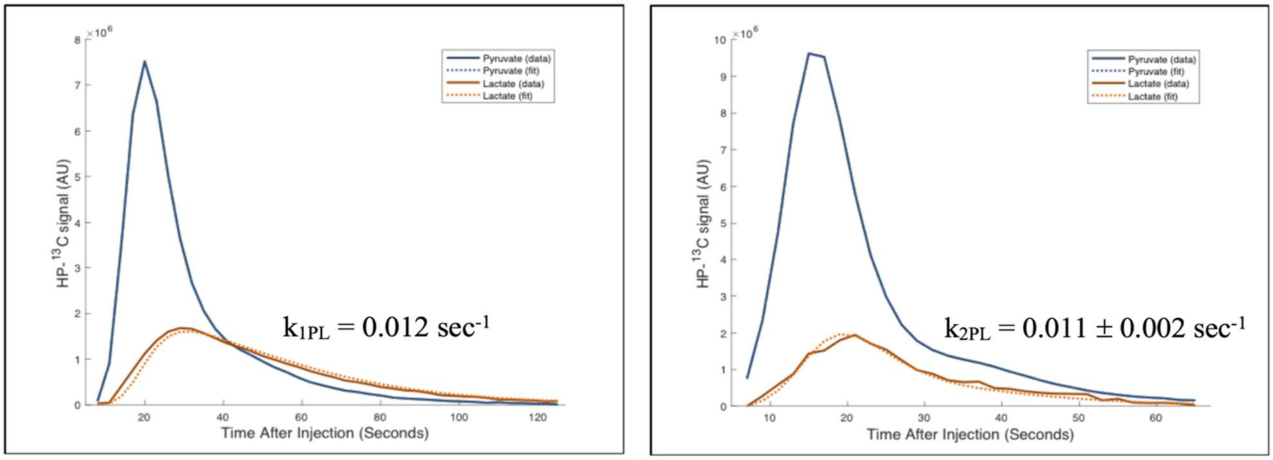

**Figure 4.7:** Plots of $k_{PL}$ analysis demonstrated similar results for a dataset previously acquired with [1-$^{13}$C]pyruvate from a volunteer (left) and [2-$^{13}$C]pyruvate from volunteers acquired in this study, with the mean ± standard error for all 4 volunteers (right).

### 4.3.3 [2-$^{13}$C]Pyruvate $k_{PL}$ Model

Figure 4.7 shows a MATLAB plot of a measured [2-$^{13}$C]pyruvate $k_{PL}$ value from the volunteer studies with calculated mean and standard error of 0.011 ± 0.002 sec$^{-1}$. The values were consistent with prior [1-$^{13}$C]pyruvate $k_{PL}$ values of 0.012 sec$^{-1}$ acquired using a similar setup and non-selective pulse-acquire strategy[8,10]. Identical results of pyruvate to lactate kinetics across a previously processed [1-$^{13}$C]pyruvate dataset and newly acquired [2-$^{13}$C]pyruvate datasets from volunteers lends verification to the robustness and consistency of approach.

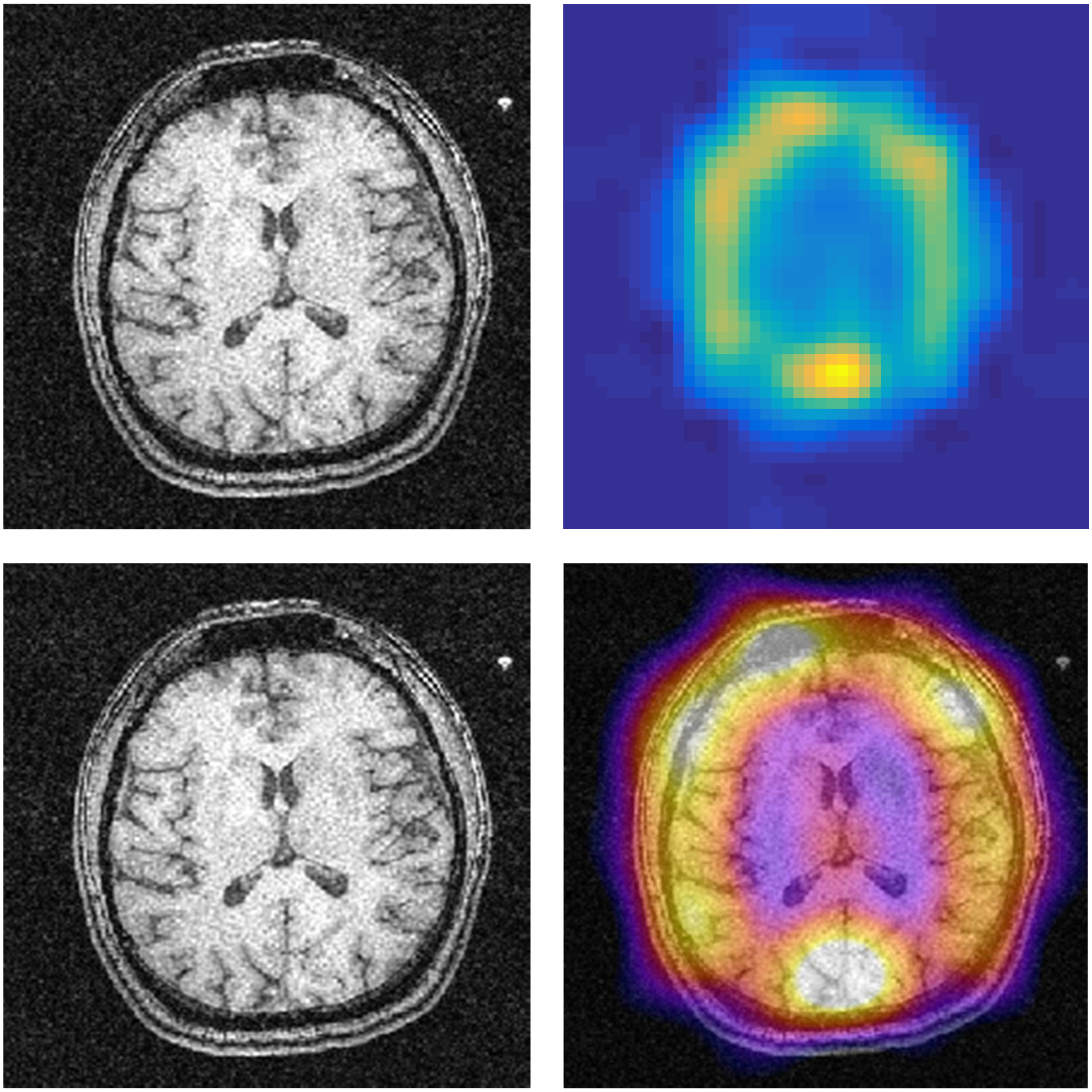

**Figure 4.8**: [2-$^{13}$C]pyruvate signal acquired using a metabolite-specific flip angle schedule and echo planar imaging (EPI) readout overlaid on reference $^{1}$H proton images. The pulse sequence was designed with: resolution = 2.5 x 2.5 cm$^{2}$, slice thickness = 5 cm, bandwidth = 6 kHz, TR = 3 sec, TE = 2.8 sec, $\theta_{Pyr}$ = 10°. Average SNR = 682.

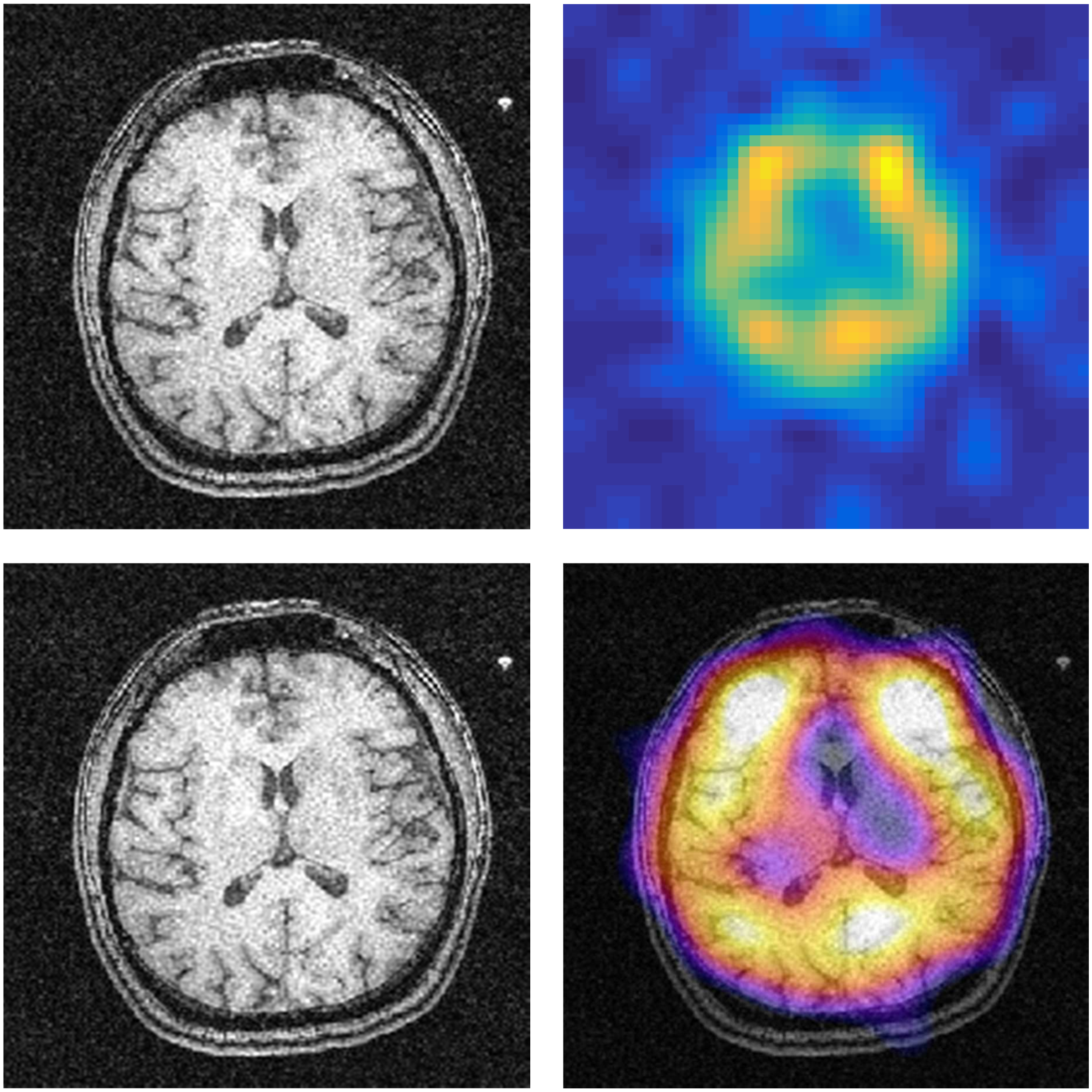

**Figure 4.9**: [5-$^{13}$C]glutamate signal acquired using a metabolite-specific flip angle schedule and echo planar imaging (EPI) readout overlaid on reference $^{1}$H proton images. The pulse sequence was designed with: resolution = 2.5 x 2.5 cm$^{2}$, slice thickness = 5 cm, bandwidth = 6 kHz, TR = 3 sec, TE = 2.8 sec, $\theta_{Glu}$ = 60°. Average SNR = 31.1.

### 4.3.4 Initial Volunteer EPI Studies

Figures 4.8 and 4.9 show initial data and feasibility of HP $^{13}$C imaging of the [2-$^{13}$C]pyruvate conversion to [5-$^{13}$C]glutamate using the specialized $^{13}$C 32-channel head coil. Not only was the uptake of HP [2-$^{13}$C]pyruvate in the human brain observed, but also its metabolic conversion to [2-$^{13}$C]lactate, [5-$^{13}$C]glutamate, and other metabolites, similar to prior animal study results[10].

## 4.4 Discussion & Conclusion

In this study we worked with the ISOTEC Stable Isotope Division of MilliporeSigma, Merck KGaA to develop GMP grade 99% enriched [2-$^{13}$C]pyruvate meeting the purity specifications established for [1-$^{13}$C]pyruvate used in numerous human studies following FDA-IND and IRB approved protocols. Prior to human studies with HP [2-$^{13}$C]pyruvate, we first tested the purity and polarization through *in vitro* NMR analysis and performed a process qualification for testing and demonstrating the sterility of the polarized solution. The NMR spectra in Figure 4.1 and quantitative values in Tables 4.1 and 4.2 demonstrated excellent data repeatability affirming the consistency of the preparation and processing methods. Metabolite ratios and dynamic plots in these initial studies directly reflected the excitation profile of the RF pulse optimized to capture the bandwidth encompassing metabolic byproducts and provided normative values for future human brain HP [2-$^{13}$C]pyruvate NMR studies. Lastly pyruvate to lactate kinetic modeling from these [2-$^{13}$C]pyruvate studies yielded $k_{PL}$ values that were consistent with results from a prior HP [1-$^{13}$C]pyruvate dataset in healthy human brain.

This study demonstrated feasibility and initial normative values for HP [2-$^{13}$C]pyruvate NMR and thus serves as the groundwork for designing new studies of neurological disorders. These future studies would clearly benefit from an imaging approach to investigate HP [2-$^{13}$C]pyruvate MRI variations associated with anatomy and pathology and examine differences using centrality metrics and connectomic analytical methods with HP [1-$^{13}$C]pyruvate MRI[12]. HP metabolic information can also be linked with modalities such as functional and diffusion MRI to build increasingly comprehensive representations of neural function, structure and metabolism[14]. Centrality metrics processing higher-order descriptors of multi-valued metabolite kinetics with advances in machine learning may further elucidate new methods for detecting early stages of neurological disorders[15].

# References

[1] Anderson NM, Mucka P, Kern JG, Feng H. The emerging role and targetability of the TCA cycle in cancer metabolism. Protein Cell. 2018;9(2):216-237. doi:10.1007/s13238-017-0451-1.

[2] Izquierdo-Garcia JL, Viswanath P, Eriksson P, et al. IDH1 Mutation Induces Reprogramming of Pyruvate Metabolism. Cancer Res. 2015;75(15):2999-3009. doi:10.1158/0008-5472.CAN-15-0840.

[3] Park I, Larson PEZ, Gordon JW, et al. Development of methods and feasibility of using hyperpolarized carbon-13 imaging data for evaluating brain metabolism in patient studies. Magn Reson Med. 2018;80(3):864-873. doi:10.1002/mrm.27077.

[4] Marjańska M, Shestov AA, Deelchand DK, Kittelson E, Henry PG. Brain metabolism under different anesthetic conditions using hyperpolarized [1-13C]pyruvate and [2-13C]pyruvate. NMR Biomed. 2018;31(12):e4012. doi:10.1002/nbm.4012.

[5] Bottomley PA, Griffiths JR, et al. Handbook of magnetic resonance spectroscopy in vivo: MRS theory, practice and applications. John Wiley & Sons, 2016.

[6] Autry AW, Gordon JW, Carvajal L, et al. Comparison between 8- and 32-channel phased-array receive coils for in vivo hyperpolarized 13 C imaging of the human brain. Magn Reson Med. 2019;82(2):833-841. doi:10.1002/mrm.27743.

[7] Vareth M, Lupo J, Larson P, Nelson S. A comparison of coil combination strategies in 3D multi-channel MRSI reconstruction for patients with brain tumors [published correction appears in NMR Biomed. 2018 Dec;31(12):e4036]. NMR Biomed. 2018;31(11):e3929. doi:10.1002/nbm.3929.

[8] Larson PEZ, Chen HY, Gordon JW, et al. Investigation of analysis methods for hyperpolarized 13C-pyruvate metabolic MRI in prostate cancer patients. NMR Biomed. 2018;31(11):e3997. doi:10.1002/nbm.3997.

[9] Hyperpolarized MRI Technology Resource Center. Hyperpolarized MRI Toolbox. (2021 December). https://hyperpolarizedmri.ucsf.edu.

[10] Park JM, Josan S, Grafendorfer T, et al. Measuring mitochondrial metabolism in rat brain in vivo using MR Spectroscopy of hyperpolarized [2-$^{13}$C]pyruvate. NMR Biomed. 2013;26(10):1197-1203. doi:10.1002/nbm.2935.

[11] Majumder S, DeMott CM, Burz DS, Shekhtman A. Using singular value decomposition to characterize protein-protein interactions by in-cell NMR spectroscopy. Chembiochem. 2014;15(7):929-933. doi:10.1002/cbic.201400030.

[12] Hagmann P, Cammoun L, Gigandet X, et al. MR connectomics: Principles and challenges. J Neurosci Methods. 2010;194(1):34-45. doi:10.1016/j.jneumeth.2010.01.014.

[13] Brender JR, Kishimoto S, Merkle H, et al. Dynamic Imaging of Glucose and Lactate Metabolism by 13C-MRS without Hyperpolarization. Sci Rep. 2019;9(1):3410. Published 2019 Mar 4. doi:10.1038/s41598-019-38981-1.

[14] Hotz I, Schultz T. Visualization and processing of higher order descriptors for multi-valued data. First ed., Springer Publishing Company, 2015.

[15] Fletcher JM, Wennekers T. From Structure to Activity: Using Centrality Measures to Predict Neuronal Activity. Int J Neural Syst. 2018;28(2):1750013. doi:10.1142/S0129065717500137.

# Chapter 5

# HP [2-$^{13}$C]Pyruvate MR Molecular Imaging with Whole Brain Coverage

*Chung BT, Kim Y, Gordon JW, Chen HY, Autry AW, Lee P, Graham J, Tan CT, Suszczynski C, Chang S, Villaneuva-Meyer J, Bok RA, Larson PEZ, Li Y, Vigneron DB. Hyperpolarized [2-13C]Pyruvate MR Molecular Imaging with Whole Brain Coverage.*

## 5.1 Abstract & Introduction

Hyperpolarized (HP) $^{13}$C Magnetic Resonance Imaging (MRI) was applied for the first time to measure and quantify the uptake and metabolism of [2-$^{13}$C]pyruvate in the normal brain. Intravenously injected HP [2-$^{13}$C]pyruvate was imaged in 5 healthy human volunteers using a specialized spectral-spatial multi-slice echoplanar imaging (EPI) pulse sequence to acquire $^{13}$C-labeled volumetric and dynamic images of [2-$^{13}$C]pyruvate and downstream metabolites [5-$^{13}$C]glutamate and [2-$^{13}$C]lactate. Metabolic ratios and apparent conversion rates of pyruvate-to-lactate ($k_{PL}$) and pyruvate-to-glutamate ($k_{PG}$) were further quantified with whole brain coverage probing glycolytic and oxidative metabolism in a single injection and exam.

Hyperpolarized carbon-13 MR using dissolution Dynamic Nuclear Polarization[1] (dDNP) has been investigated in animals[2,3] since 2006 to provide a unique window into cellular metabolism enabling the quantification of enzyme-catalyzed conversion rates that inform on critical cellular biochemistry in both normal and pathologic conditions[2,3,4]. A first-in-human proof of concept clinical trial of HP [1-$^{13}$C]pyruvate completed in 2013 demonstrated feasibility and safety in patients[5]. The subsequent development of commercial research polarizers enabled new technical developments and initial human studies over the past 5 years in a variety of applications including prostate cancer, brain tumors, renal cancer, cardiac disease, pancreatic cancer, traumatic brain injury and breast cancer[6-23]. Since 2018, studies have investigated cerebral energy metabolism with [1-$^{13}$C]pyruvate in the normal brain and neuro-pathologies[7,14-23], demonstrating novel insights into brain bioenergetics by measuring HP pyruvate conversions to lactate catalyzed by the enzyme lactate dehydrogenase (LDH) and to bicarbonate via pyruvate dehydrogenase (PDH). Technical advances have included new specialized acquisition and analysis for brain studies[18,21]. A variable resolution HP $^{13}$C EPI approach[18] was developed that enables the acquisition of the injected HP [1-$^{13}$C]pyruvate at a higher spatial resolution than its metabolic products lactate and bicarbonate with their lower inherent SNR[18]. Also benefiting this and other studies is the development of a denoising method using a patch-based higher order singular value decomposition (HOSVD) method[21] that was applied for the first time for [2-$^{13}$C]pyruvate HP MRI in this study.

HP $^{13}$C MRI with [2-$^{13}$C]pyruvate has clinical potential to investigate TCA cycle metabolism and assess pyruvate-to-glutamate conversion rates in addition to pyruvate-to-lactate through whole brain signal acquisitions with sufficient signal-to-noise ratio. Although [1-$^{13}$C]pyruvate has successfully been utilized as a primary probe particularly to obtain $k_{PL}$, its metabolism and conversion to $^{13}CO_2$ prevents direct detection of downstream TCA cycle metabolites including [5-$^{13}$C]glutamate. [2-$^{13}$C]pyruvate is also converted to [2-$^{13}$C]lactate in addition to [5-$^{13}$C]glutamate enabling direct detection and calculation of both pyruvate-to-lactate $k_{PL}$ and pyruvate-to-glutamate $k_{PG}$ conversion rates. Glutamate is the most abundant free amino acid in the brain and is at the crossroad between multiple metabolic pathways[24,25]. Also, glutamate is a neurotransmitter that is critical for neuronal signal transmission in the brain and throughout the nerves in the body and plays an important role during brain development, learning and memory[24]. Glutamate has also shown to be decreased in aging and neurodegeneration[25]. The initial first-in-human study[26] using non-localized HP $^{13}$C MR spectroscopy demonstrated the feasibility of obtaining human HP [2-$^{13}$C]pyruvate brain data, but did not provide the ability to image metabolic conversions throughout the brain as is required for detection of both normal and pathologic variations. In this new project multi-slice, dynamic HP [2-$^{13}$C]pyruvate echo-planar imaging (EPI) was developed and applied in healthy volunteer studies with whole brain coverage to investigate its application for human brain studies using HP [2-$^{13}$C]pyruvate.

## 5.2 Methods

Imaging studies were performed on a 3T clinical MR system (MR750, GE Healthcare, Waukesha, WI) using a commercially available 8-channel $^{1}$H / 24-channel $^{13}$C head coil (RAPID Biomedical, Germany) with an integrated $^{13}$C birdcage for RF transmit. The $^{13}$C RF power was calibrated using a head phantom containing natural abundance ethylene glycol prior to the study. Four healthy volunteers were imaged following an IRB-approved protocol. Persons ranging in age from 29-60 years old were imaged at approximately midday with 1 volunteer scanned on two different days yielding a total of 5 datasets.

### 5.2.1 [2-$^{13}$C]Pyruvate Preparation

Hyperpolarization was performed on a 5T SPINlab polarizer (GE Healthcare) operating at 0.8K. Samples containing 1.47g [2-$^{13}$C]pyruvic acid (MilliporeSigma Isotec Stable Isotopes) and 15mM electron paramagnetic agent (AH111501, GE Healthcare) were prepared the morning of the study and polarized for at least two hours. Samples were then rapidly dissolved using superheated water and the electron paramagnetic agent was removed by filtration prior to neutralization with a TRIS-buffered NaOH solution. Prior to injection, the pH, pyruvate and residual EPA concentrations, polarization, and sample temperature were rapidly measured with an integrated quality control (QC) module. In parallel, the integrity of the 0.2 μm sterile filter was tested in agreement with manufacturer specifications prior to injection. After release by the pharmacist, a 0.43 mL/kg dose of 241 ± 7 mM pyruvate (n = 5) was injected at a rate of 5 mL/s, followed by a 20 mL sterile saline flush (0.9% sodium chloride, Baxter Healthcare Corporation).

### 5.2.2 Human MR Imaging Protocol: [2-$^{13}$C]Pyruvate Spectral-Spatial Pulse with EPI

All data were acquired with a variable resolution, metabolite-selective EPI pulse sequence using the RF toolbox available from the Hyperpolarized MRI Toolbox via the Hyperpolarized Technology Resource Center website[28]. The single band spectral-spatial (SPSP) RF pulse (18.1 ms duration) was designed to independently excite [2-$^{13}$C]pyruvate, [5-$^{13}$C]glutamate, and downfield and upfield resonances of [2-$^{13}$C]lactate with minimal off-resonance excitation shown in Figures 5.1 and 5.2. To avoid J-coupling artifacts, the downfield and upfield peaks of [2-$^{13}$C]lactate were acquired independently. Using a multi-resolution approach, [2-$^{13}$C]pyruvate was acquired with in-plane spatial resolution of 7.5 x 7.5 mm$^2$ and 20° tip angle, while the downstream metabolites [5-$^{13}$C]glutamate and the [2-$^{13}$C]lactate doublet were acquired with an in-plane resolution of 22.5 x 22.5 mm$^2$ and 60° tip angle. Five 3-cm slices were acquired with a field of view (FOV) of 24 cm x 24 cm. 20 timeframes were acquired per metabolite with 3 second temporal resolution (TR) for a total scan time of 60 seconds. $T_1$ weighted $^1$H IR-SPGR (spoiled gradient recalled) images were acquired for anatomical reference.

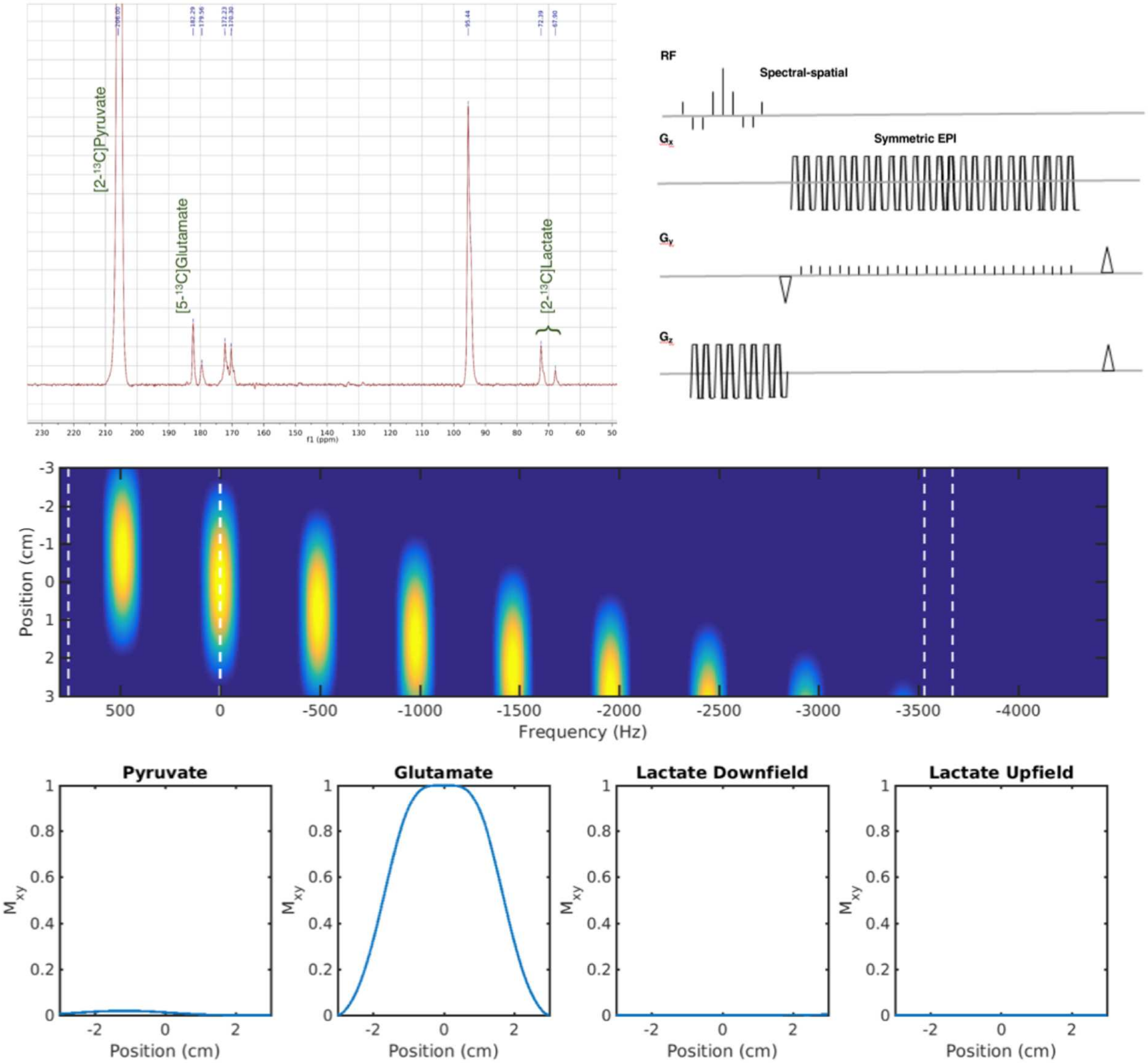

**Figure 5.1:** Optimized spectral-spatial RF pulse and EPI readout showing simulated responses from [2-$^{13}$C]pyruvate, [5-$^{13}$C]glutamate and [2-$^{13}$C]lactate to demonstrate the effectiveness of designed pass & stopbands. Upper left: Representative NMR spectra acquired determining targeted frequencies for [2-$^{13}$C]pyruvate and separation of metabolites. The asymmetry of the lactate doublet is primarily due to the RF excitation band used. Upper right: Sequence diagram illustrating the metabolite-selective EPI acquisition. Lower: The spectral-spatial response of the 2D RF pulse used to selectively excite [2-$^{13}$C]pyruvate (207 ppm), [5-$^{13}$C]glutamate (182 ppm), and the [2-$^{13}$C]lactate doublet (72, 67 ppm) with minimal off-resonance excitation. See Figure 5.2 for frequency responses of the specialized RF pulse when centered on other resonances.

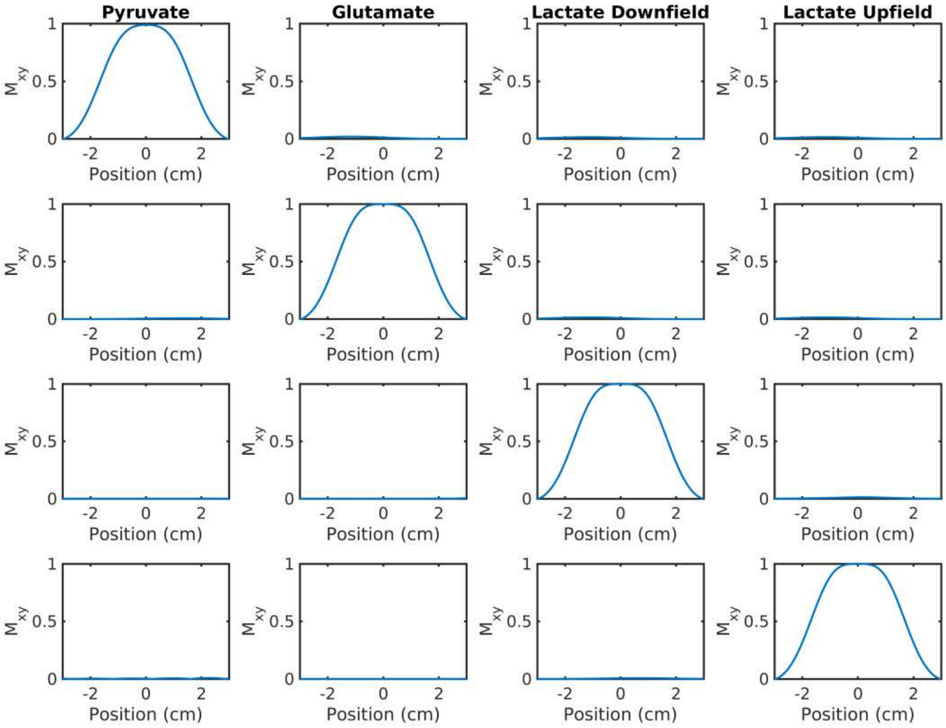

**Figure 5.2:** Simulations of on and off-resonance responses for four frequencies corresponding to metabolites of interest. Independent peak excitations contributed to minimizing both unintended metabolite excitations and J-coupling artifacts resulting from peak proximity in the [2-$^{13}$C]lactate doublet.

### 5.2.3 Data Analysis and Quantitative Post-Processing

Following k-space noise pre-whitening, optimal coil combination techniques[27] were performed across multichannel datasets with [2-$^{13}$C]pyruvate end of scan timeframes serving as signal-less floors to determine noise covariance[21]. Image reconstruction was performed using the Orchestra toolbox (GE Healthcare) in MATLAB. The HP $^{13}$C data was denoised using patch-based higher order singular value decomposition (HOSVD) method[21]. In this study the following parameters were used in denoising all cases: $k_{global}$ = 0.4; $k_{local}$ = 0.8 (scales used to determine thresholds); step = 2. In low-resolution cases: patch size = 3; search window size = 4; and in high-resolution cases: patch size = 5; search window size = 6.

Signal maps for each metabolite were generated by normalizing voxels to global peak pyruvate signal. Maps of [5-$^{13}$C]glutamate to [2-$^{13}$C]pyruvate and [5-$^{13}$C]glutamate to [2-$^{13}$C]lactate ratios were further calculated and analyzed.

Voxel-wise $k_{PG}$ and $k_{PL}$ calculations were performed with two-site exchange models[28] also from the Hyperpolarized MRI Toolbox. For the glutamate-to-lactate conversion ($k_{PG}$) model, similar calculations were performed using the measured pyruvate magnetization as input to fit the glutamate magnetization through a minimization of constrained least-squares difference across estimated and measured signal. Mean parameter values were determined voxel-wise after applying a minimum SNR mask of 0.18. Brain masks used for displaying AUC images overlaid on $^{1}$H images were created using $T_2$-fast spin echo images with thresholds.

## 5.3 Results

### 5.3.1 Hyperpolarized [2-$^{13}$C]Pyruvate MR Imaging

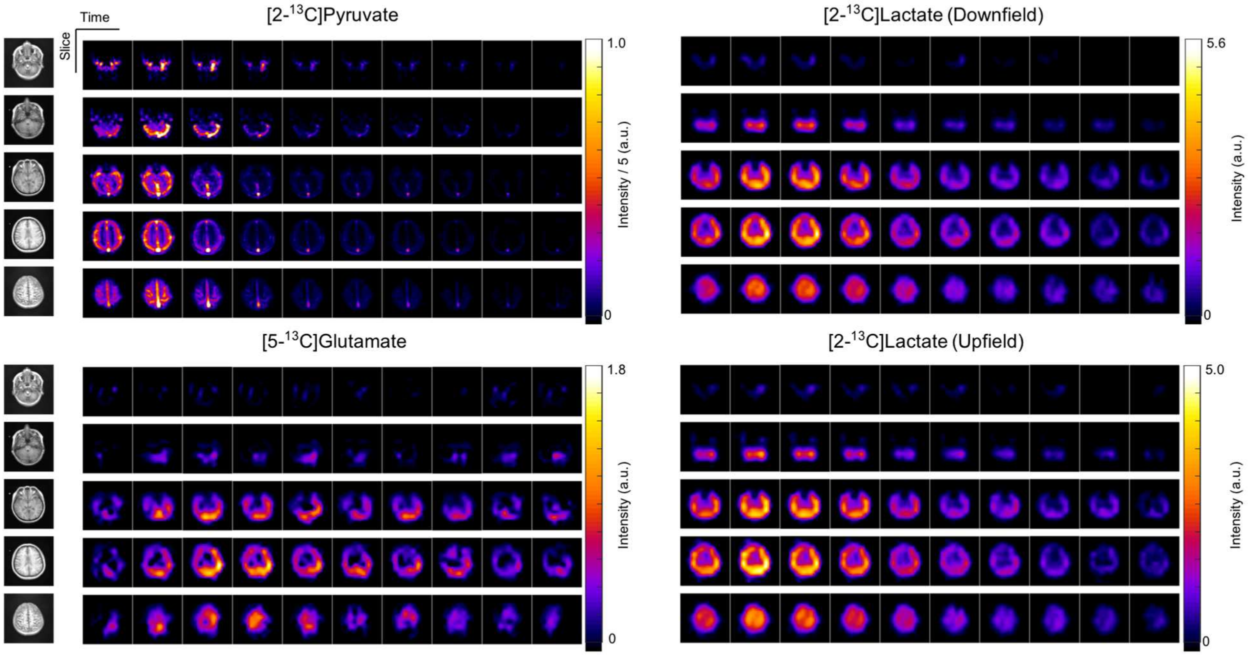

**Figure 5.3:** 3D dynamics of HP [2-$^{13}$C]pyruvate, [5-$^{13}$C]glutamate, [2-$^{13}$C]lactate (downfield peak) and [2-$^{13}$C]lactate (upfield peak) from a human brain volunteer. Displayed images show the first 10 timeframes with TR = 3 seconds for a total of window of 30 seconds following denoising using a patch-based HOSVD method[21]. Shown on the left are $^{1}$H IR-SPGR anatomy images capturing average of slices. Upper window levels for [2-$^{13}$C]pyruvate data were adjusted to 20% of the maximum intensity.

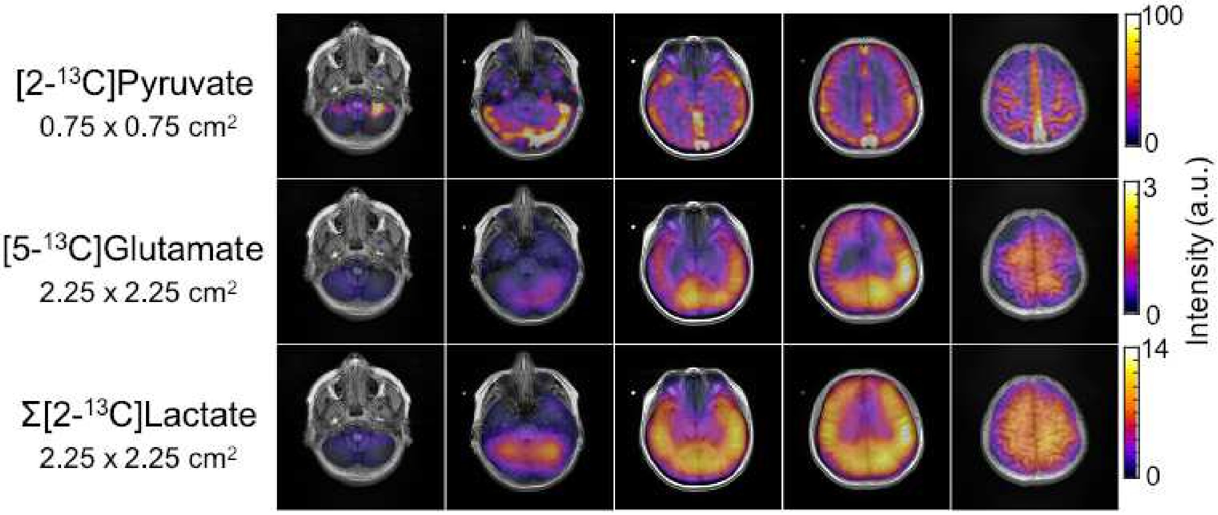

**Figure 5.4:** AUC images from a volunteer summed over 20 timeframes as shown in Figure 5.3 overlaid on $^{1}$H IR-SPGR images. [2-$^{13}$C]lactate images illustrate acquired signal after summing both downfield and upfield peaks. High resolution (0.75 x 0.75 cm$^{2}$) pyruvate data shows strong arterial and venous signal, and a brainmask to reduce the pyruvate signal from muscle high localization and spatial variations of grey and white matter was consequently applied.

Figure 5.3 shows dynamic images of signal from [2-$^{13}$C]pyruvate, [5-$^{13}$C]glutamate, and upfield and downfield [2-$^{13}$C]lactate in the brain of a healthy volunteer. Maximum signal intensity from this volunteer were normalized to the pyruvate signal and demonstrated a SNR gain for pyruvate was 6.6, and 6.3 for glutamate and 4 for lactate.

High resolution [2-$^{13}$C]pyruvate data acquired at 0.75 x 0.75 cm$^{2}$ shows strong arterial and venous signal well separated from surrounding tissue. Courser resolution glutamate and lactate data acquired at 2.25 x 2.25 cm$^{2}$ achieved sufficiently high SNR for whole brain coverage. Area-Under-Curve (AUC) images were composed following a complex summation of data. Figure 5.4 shows AUC images for a volunteer overlaid on $^{1}$H IR-SPGR images.

We observe a good detection of lactate, which is better with [1-$^{13}$C]pyruvate, however at lower fields, the greater chemical shift separation of [2-$^{13}$C]pyruvate and [2-$^{13}$C]lactate can lend practical conveniences and data integrity. Results of separately acquiring two peaks of the lactate doublet agreed with total lactate signal combining downfield and upfield lactate images, and the lactate distribution appeared similarly across images of downfield and upfield signals prior to summation. Artifacts arising from J-coupling were not observed.

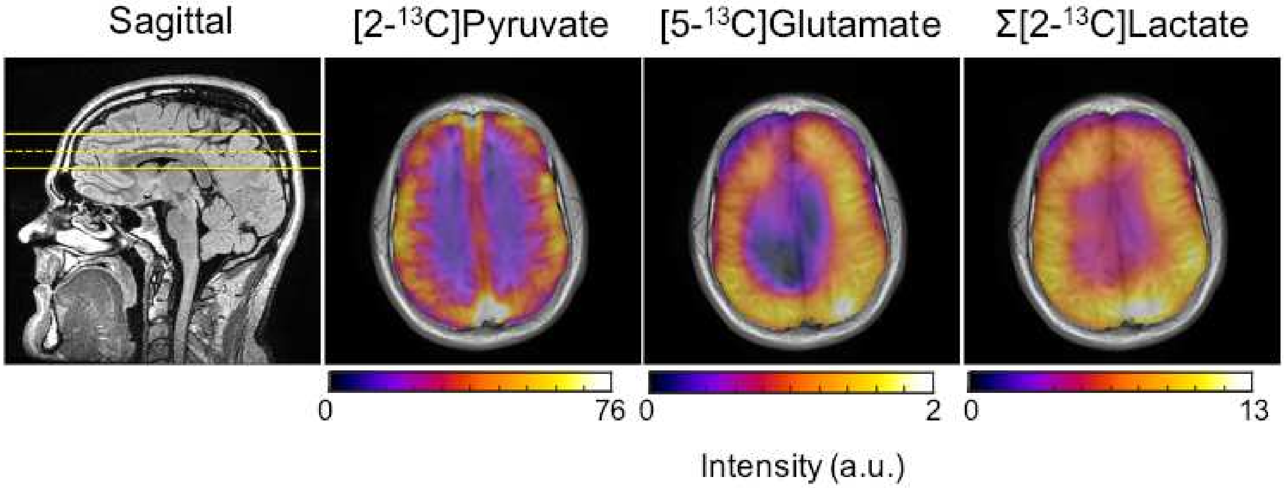

**Figure 5.5:** Sagittal and overlaid mid-slice axial T1-weighted $^{13}$C AUC images for another volunteer with 3 cm slice thickness. AUC images summed across 20 timeframes are shown with intensity scales below for each metabolite in this central slice and the [2-$^{13}$C]pyruvate image at resolution 0.75 x 0.75 cm$^2$ and metabolites at 2.25 x 2.25 cm$^2$.

Figure 5.5 shows representative $^{13}$C area-under-curve (AUC) images of pyruvate, glutamate, and summed lactate (downfield and upfield) from a volunteer. The sagittal image depicts the anatomical position calculated from the DICOM header of the acquired slice. Adjacent signal overlays show the distribution of [2-$^{13}$C]pyruvate and downstream metabolites of [2-$^{13}$C]lactate and [5-$^{13}$C]glutamate.

### 5.3.2 Metabolite Ratios & Kinetic Rates ($k_{PG}$, $k_{PL}$)

Table 5.1 summarizes calculated metabolite ratios, $k_{PG}$, and $k_{PL}$ values for each dataset.

**Table 5.1:** Summary of calculated AUC ratios and apparent kinetic rates for each denoised volunteer dataset zero-filled to match [2-$^{13}$C]pyruvate signal matrix sizes (32 x 32). Mean and standard deviation are reported observing disparities in experimental values.

| Experiment | [5-$^{13}$C]Glu : [2-$^{13}$C]Pyr | [5-$^{13}$C]Glu : ∑[2-$^{13}$C]Lac | $k_{PG}$ (sec$^{-1}$) | $k_{PL}$ (sec$^{-1}$) |
|---|---|---|---|---|
| 1 | 0.039 | 0.31 | 0.0022 | 0.017 |
| 2 | 0.031 | 0.26 | 0.0019 | 0.022 |
| 3 | 0.026 | 0.26 | 0.0013 | 0.022 |
| 4 | 0.036 | 0.39 | 0.0018 | 0.015 |
| 5 | 0.028 | 0.34 | 0.0013 | 0.012 |
| Mean ± S.D. | 0.032 ± 0.005 | 0.31 ± 0.06 | 0.0017 ± 0.0004 | 0.018 ± 0.004 |

## 5.4 Discussion & Conclusion

Hyperpolarized (HP) [1-$^{13}$C]pyruvate is the most widely utilized molecular contrast agent for MR metabolic imaging to characterize abnormal metabolism in patients with tumors, based on the measured glycolytic metabolism of [1-$^{13}$C]pyruvate-to-[1-$^{13}$C]lactate conversion upregulated in tumors. The application of [1-$^{13}$C]pyruvate, however, is limited for assessing the flux of pyruvate to TCA cycle only through pyruvate dehydrogenase (PDH) because the $^{13}$C label is lost as $CO_2$ during the conversion to Acetyl-CoA. Alternatively, labeling the C2 position of pyruvate provides access to the TCA cycle as the labeled carbon is carried over to acetyl-CoA and eventually to the glutamate pool, but is more difficult to image because of a shorter $T_1$, a less sparse spectrum, and peak-splitting due to $J_{CH}$ coupling. The safety and feasibility of using HP [2-$^{13}$C]pyruvate for measuring its conversion to [2-$^{13}$C]lactate and [5-$^{13}$C]glutamate in the brain of healthy volunteers was previously demonstrated with non-localized dynamic $^{13}$C MR spectroscopy[26]. However, these previously published methods were limited and not useful to enable whole brain HP [2-$^{13}$C]pyruvate MRI that is required to study both normal variations and localized pathologic alterations of the metabolic parameters provided using this new HP agent. In this project, multi-slice, dynamic HP [2-$^{13}$C]pyruvate echo-planar imaging (EPI) was developed and applied in healthy volunteer studies with whole brain coverage to investigate its application for human brain studies using HP [2-$^{13}$C]pyruvate. A variable resolution multislice EPI approach[18] to achieve whole brain coverage was utilized enabling the acquisition of glutamate images and a quantification of spatial and temporal distribution for future studies and pathology. Patch-based higher-order singular value decomposition (HOSVD) denoising methods[21] were also applied to datasets leading to further improved visualization of the metabolite signals and quantification of $k_{PL}$ and $k_{PG}$ kinetic conversion rates.

This research project developed a new approach and HP $^{13}$C MR RF pulse sequence improvements for acquiring volumetric and dynamic EPI of HP [2-$^{13}$C]pyruvate metabolism to [5-$^{13}$C]glutamate and to [2-$^{13}$C]lactate probing glycolytic and oxidative metabolism simultaneously. This study demonstrated feasibility and initial results in five normal volunteer studies. The strategy of separately exciting the two peaks of the lactate doublet was shown feasible for imaging metabolites with signal splitting. In combination with a variable resolution approach, the hyperpolarized metabolite signals were utilized for quantifying $k_{PL}$ and $k_{PB}$ throughout the brain of healthy volunteers providing new measures of cerebral energy metabolism. This study quantified the metabolism of hyperpolarized [2-$^{13}$C]pyruvate to [2-$^{13}$C]lactate and [5-$^{13}$C]glutamate in the healthy human brain for the first time. Measuring of spatial localizations of pyruvate-to-lactate and pyruvate-to-glutamate conversions signifies an important step to use HP [2-$^{13}$C]pyruvate to investigate cerebral energy metabolism and potentially characterize brain tumors with isocitrate dehydrogenase (IDH) mutations.

# References

[1] Ardenkjaer-Larsen JH, Fridlund B, Gram A, et al. Increase in signal-to-noise ratio of > 10,000 times in liquid-state NMR. In: Proceedings of the National Academy of Sciences. 2003; 100(18):10158-10163.

[2] Golman K, Ardenkjaer-Larsen JH, Petersson JS, Mansson S, Leunbach I. Molecular imaging with endogenous substances. Proc Natl Acad Sci U S A 100(18):10435-9, 2003. PMCID: PMC193579.

[3] Golman K, Zandt RI, Lerche M, Pehrson R, Ardenkjaer-Larsen JH. Metabolic imaging by hyperpolarized $^{13}C$ magnetic resonance imaging for in vivo tumor diagnosis. Cancer Res 66(22):10855-60, 2006.

[4] Kurhanewicz J, Vigneron D, Bankson J, Brindle K, Cunningham C, Gallagher F, Keshari K, Kjaer A, Laustsen C, Mankoff D, Merritt M, Nelson S, Pauly J, Lee P, Ronen S, Tyler D, Rajan S, Spielman D, Wald L, Zhang X, Malloy C, Rizi R. Hyperpolarized $^{13}C$ MRI: Path to Clinical Translation in Oncology. Neoplasia. 2019; 21(1):1-16. PMCID: PMC6260457.

[5] Nelson SJ, Kurhanewicz J, Vigneron DB, Larson PE, Harzstark AL, Ferrone M, van Criekinge M, Chang JW, Bok R, Park I, Reed G, Carvajal L, Small EJ, Munster P, Weinberg VK, Ardenkjaer-Larsen JH, Chen AP, Hurd RE, Odegardstuen LI, Robb FJ, Tropp J, Murray JA. Metabolic imaging of patients with prostate cancer using hyperpolarized [1-$^{13}C$]pyruvate. Sci Transl Med 5(198):198ra08, 2013. PMCID: PMC4201045.

[6] Granlund KL, Tee SS, Vargas HA, Lyashchenko SK, Reznik E, Fine S, Laudone V, Eastham JA, Touijer KA, Reuter VE, Gonen M, Sosa RE, Nicholson D, Guo YW, Chen AP, Tropp J, Robb F, Hricak H, Keshari KR. Hyperpolarized MRI of Human Prostate Cancer Reveals Increased Lactate with Tumor Grade Driven by Monocarboxylate Transporter 1. Cell Metab. 2020; 31(1):105-114.e3. PMCID: PMC6949382.

[7] Miloushev VZ, Granlund KL, Boltyanskiy R, Lyashchenko SK, DeAngelis LM, Mellinghoff IK, Brennan CW, Tabar V, Yang TJ, Holodny AI, Sosa RE, Guo YW, Chen AP, Tropp J, Robb F, Keshari KR. Metabolic Imaging of the Human Brain with Hyperpolarized $^{13}$C Pyruvate Demonstrates $^{13}$C Lactate Production in Brain Tumor Patients. Cancer Res. 2018; 78(14):3755-3760. PMCID: PMC6050093.

[8] Cunningham CH, Lau JY, Chen AP, Geraghty BJ, Perks WJ, Roifman I, Wright GA, Connelly KA. Hyperpolarized $^{13}$C Metabolic MRI of the Human Heart: Initial Experience. Circ Res. 2016; 119(11):1177-1182. PMCID: PMC5102279.

[9] Abeyakoon O, Latifoltojar A, Gong F, Papoutsaki MV, Chowdhury R, Glaser M, Jeraj H, Awais R, Holt C, Twyman F, Arstad E, Gadian DG, Atkinson D, Comment A, O'Callaghan J, Smith L, Beeston T, Clemente J, Patani N, Stein R, Yuneva M, Szabadkai G, Halligan S, Punwani S. Hyperpolarised $^{13}$C MRI: a new horizon for non-invasive diagnosis of aggressive breast cancer. BJR Case Rep. 2019; 5(3):20190026. PMCID: PMC6750630.

[10] Gallagher FA, Woitek R, McLean MA, Gill AB, Manzano Garcia R, Provenzano E, Riemer F, Kaggie J, Chhabra A, Ursprung S, Grist JT, Daniels CJ, Zaccagna F, Laurent MC, Locke M, Hilborne S, Frary A, Torheim T, Boursnell C, Schiller A, Patterson I, Slough R, Carmo B, Kane J, Biggs H, Harrison E, Deen SS, Patterson A, Lanz T, Kingsbury Z, Ross M, Basu

B, Baird R, Lomas DJ, Sala E, Wason J, Rueda OM, Chin SF, Wilkinson IB, Graves MJ, Abraham JE, Gilbert FJ, Caldas C, Brindle KM. Imaging breast cancer using hyperpolarized carbon-13 MRI. Proc Natl Acad Sci U S A. 2020; 117(4):2092-2098. PMCID: PMC6995024.

[11] Stødkilde-Jørgensen H, Laustsen C, Hansen ESS, Schulte R, Ardenkjaer-Larsen JH, Comment A, Frøkiaer J, Ringgaard S, Bertelsen LB, Ladekarl M, Weber B. Pilot Study Experiences With Hyperpolarized [1-(13) C]pyruvate MRI in Pancreatic Cancer Patients. J Magn Reson Imaging. 2020 Mar;51(3):961-963. doi: 10.1002/jmri.26888. Epub 2019 Aug 1. PMID: 31368215.

[12] Tran M, Latifoltojar A, Neves JB, Papoutsaki MV, Gong F, Comment A, Costa ASH, Glaser M, Tran-Dang MA, El Sheikh S, Piga W, Bainbridge A, Barnes A, Young T, Jeraj H, Awais R, Adeleke S, Holt C, O'Callaghan J, Twyman F, Atkinson D, Frezza C, Årstad E, Gadian D, Emberton M, Punwani S. First-in-human in vivo non-invasive assessment of intra-tumoral metabolic heterogeneity in renal cell carcinoma. BJR Case Rep. 2019; 5(3). pii: 20190003. PMCID: PMC6699984.

[13] Aggarwal R, Vigneron DB, Kurhanewicz J. Hyperpolarized 1-[$^{13}$C]-Pyruvate Magnetic Resonance Imaging Detects an Early Metabolic Response to Androgen Ablation Therapy in Prostate Cancer. Eur Urol. 2017; 72(6):1028-1029. PMCID: PMC5723206.

[14] Park I, Larson PEZ, Gordon JW, Carvajal L, Chen HY, Bok R, Van Criekinge M, Ferrone M, Slater JB, Xu D, Kurhanewicz J, Vigneron DB, Chang S, Nelson SJ. Development of methods and feasibility of using hyperpolarized carbon-13 imaging data for

evaluating brain metabolism in patient studies. Magn Reson Med. 2018; 80(3):864-873. PMCID: PMC5980662.

[15] Autry AW, Gordon JW, Carvajal L, Mareyam A, Chen HY, Park I, Mammoli D, Vareth M, Chang SM, Wald LL, Xu D, Vigneron DB, Nelson SJ, Li Y. Comparison between 8- and 32-channel phased-array receive coils for in vivo hyperpolarized $^{13}$C imaging of the human brain. Magn Reson Med. 2019; 82(2):833-841. PMCID: PMC6612511.

[16] Grist JT, McLean MA, Riemer F, Schulte RF, Deen SS, Zaccagna F, Woitek R, Daniels CJ, Kaggie JD, Matys T, Patterson I, Slough R, Gill AB, Chhabra A, Eichenberger R, Laurent MC, Comment A, Gillard JH, Coles AJ, Tyler DJ, Wilkinson I, Basu B, Lomas DJ, Graves MJ, Brindle KM, Gallagher FA. Quantifying normal human brain metabolism using hyperpolarized [1-13C]pyruvate and magnetic resonance imaging. Neuroimage. 2019 Apr 1;189:171-179. PMCID: PMC6435102.

[17] Autry AW, Gordon JW, Chen HY, LaFontaine M, Bok R, Van Criekinge M, Slater JB, Carvajal L, Villanueva-Meyer JE, Chang SM, Clarke JL, Lupo JM, Xu D, Larson PEZ, Vigneron DB, Li Y. Characterization of serial hyperpolarized $^{13}$C metabolic imaging in patients with glioma. Neuroimage Clin. 2020; 27:102323. PMCID: PMC7334458.

[18] Gordon JW, Autry AW, Tang S, Graham JY, Bok RA, Zhu X, Villanueva-Meyer JE, Li Y, Ohliger MA, Abraham MR, Xu D, Vigneron DB, Larson PEZ. A variable resolution approach for improved acquisition of hyperpolarized $^{13}$C metabolic MRI. Magn Reson Med. 2020; 84(6):2943-2952. PMCID: PMC7719570.

[19] Hackett EP, Pinho MC, Harrison CE, Reed GD, Jeff Liticker, Raza J, Hall RG, Malloy CR, Barshikar S, Madden CJ, Park JM. Imaging acute metabolic changes in mild traumatic

brain injury patients using hyperpolarized [1-$^{13}$C]pyruvate. iScience. 2020; 23(12):101885. iScience. 2020; 23(12):101885. PMCID: PMC7736977.

[20] Autry AW, Park I, Kline C, Chen HY, Gordon JW, Raber S, Hoffman C, Kim Y, Okamoto K, Vigneron DB, Lupo JM, Prados M, Li Y, Xu D, Mueller S. Pilot Study of Hyperpolarized $^{13}$C Metabolic Imaging in Pediatric Patients with Diffuse Intrinsic Pontine Glioma and Other CNS Cancers. Am J Neuroradiol. 2021; 42(1):178-184. PMCID: PMC7814790.

[21] Kim Y, Chen HY, Autry AW, Villanueva-Meyer J, Chang SM, Li Y, Larson PEZ, Brender JR, Krishna MC, Xu D, Vigneron DB, Gordon JW. Denoising of hyperpolarized $^{13}$C MR images of the human brain using patch-based higher-order singular value decomposition. Magn Reson Med. 2021; 86(5):2497-2511. PMCID: PMC8530853.

[22] Li Y, Vigneron DB, Xu D. Current human brain applications and challenges of dynamic hyperpolarized carbon-13 labeled pyruvate MR metabolic imaging. Eur J Nucl Med Mol Imaging. 2021; 48(13):4225-4235. PMCID: PMC8566394.

[23] Chen J, Patel TR, Pinho MC, Choi C, Harrison CE, Baxter JD, Derner K, Pena S, Liticker J, Raza J, Hall RG, Reed GD, Cai C, Hatanpaa KJ, Bankson JA, Bachoo RM, Malloy CR, Mickey BE, Park JM. Preoperative imaging of glioblastoma patients using hyperpolarized $^{13}$C pyruvate: Potential role in clinical decision making. Neurooncol Adv. 2021; 28;3(1):vdab092. PMCID: PMC8331053.

[24] Petroff OA. GABA and glutamate in the human brain. Neuroscientist. 2002 Dec;8(6):562-73. doi: 10.1177/1073858402238515. PMID: 12467378.

[25] Segovia G, Porras A, Del Arco A, Mora F. Glutamatergic neurotransmission in aging: a critical perspective. Mech Ageing Dev. 2001 Jan;122(1):1-29. PMID: 11163621.

[26] Chung BT, Chen HY, Gordon J, Mammoli D, Sriram R, Autry AW, Le Page LM, Chaumeil MM, Shin P, Slater J, Tan CT, Suszczynski C, Chang S, Li Y, Bok RA, Ronen SM, Larson PEZ, Kurhanewicz J, Vigneron DB. First hyperpolarized [2-$^{13}$C]pyruvate MR studies of human brain metabolism. J Magn Reson. 2019; 309:106617. PMCID: PMC6880930.

[27] Zhu Z, Zhu X, Ohliger MA, Tang S, Cao P, Carvajal L, Autry AW, Li Y, Kurhanewicz J, Chang S, Aggarwal R, Munster P, Xu D, Larson PEZ, Vigneron DB, Gordon JW. Coil Combination Methods for Multi-Channel Hyperpolarized $^{13}$C Imaging Data from Human Studies. J Magn Reson. 2019; 301:73-79. PMCID: PMC7170546.

[28] Hyperpolarized MRI Technology Resource Center. Hyperpolarized MRI Toolbox. (2021 December). https://hyperpolarizedmri.ucsf.edu.

# Chapter 6

# Signal Processing for Improved Quantification of HP [2-$^{13}$C]Pyruvate to [5-$^{13}$C]Glutamate Conversion

*Chung BT, Gordon J, Chen HY, Leynes A, Autry AW, Larson PEZ, Vigneron DB. Signal Processing and Singular Value Decomposition (SVD) for Improved Quantification of Hyperpolarized [2-$^{13}$C]Pyruvate to [5-$^{13}$C]Glutamate Conversion. Poster presentation at ISMRM Sedona Workshop on Data Sampling and Image Reconstruction.*

*Mammoli D, Gordon J, Autry A, Larson PEZ, Li Y, Chen HY, Chung B, Shin P, Van Criekinge M, Carvajal L, Slater JB, Bok R, Crane J, Xu D, Chang S, Vigneron DB. Kinetic Modeling of Hyperpolarized Carbon-13 Pyruvate Metabolism in the Human Brain. IEEE Trans Med Imaging. Feb 2020. Doi: 10.1109/TMI.2019.2926437.*

## 6.1 Abstract & Introduction

This technique development project was designed to better quantify [2-$^{13}$C]pyruvate-to-[5-$^{13}$C]glutamate apparent conversion rates ($k_{PG}$) using two-site exchange input-less kinetic models[1]. Previous published work investigated new methods for mapping [1-$^{13}$C]pyruvate-to-[1-$^{13}$C]lactate ($k_{PL}$) and [1-$^{13}$C]pyruvate-to-[1-$^{13}$C]bicarbonate ($k_{PB}$) conversion rates with whole-brain coverage[2]. A data-driven approach was used to select an optimal model for fitting the data as well as determine an appropriate goodness-of-fit metric.

Due to the multitude of downstream metabolites of [2-$^{13}$C]pyruvate, prior kinetic models using two-site exchange are limited in their accuracy of $k_{PG}$ fitting and quantification and are further sensitive to noise from the distribution of magnetization corresponding to signal loss through relaxation and biochemical conversion[1-6]. The goal of this work was to incorporate and investigate a SVD (singular value decomposition) denoising algorithm to enable more repeatable and robust $k_{PG}$ quantification.

Quantitative techniques to resolve artifacts from metabolites with multiple peaks due to J-coupling and splitting from spin-spin interactions similarly utilize density matrix theory to both numerically and analytically derive coherences arising during RF excitation and readout. For the [2-$^{13}$C]lactate doublet in particular, a combination of computer simulations and experiments has been shown in conjunction with a highly narrow RF pulse band to successfully image and improve quantification measuring individual peaks[7]. The inherent low SNR of the [5-$^{13}$C]glutamate singlet in addition to its proximity with other metabolite peaks of interest presents different challenges yet is hypothesized to benefit from a kindred combination of simulations.

## 6.2 Methods

An echo-planar imaging (EPI) MR approach using a spectral-spatial excitation pulse was developed and implemented measuring HP [2-$^{13}$C]pyruvate to [5-$^{13}$C]glutamate conversion in volunteers. Using a specialized $^{13}$C 32-channel head coil[8], the excitation pulse was designed to robustly increase signal from metabolites with known chemical shifts[3,6,9]. Single time point data was further selected for analysis based on SNR with appropriate time windows comparing model results.

$$\begin{aligned} \frac{dP_Z(t)}{dt} &= -R_{1P}P_Z(t) - k_{PL}P_Z(t) + u(t) \\ \frac{dL_Z(t)}{dt} &= -R_{1L}L_Z(t) + k_{PL}P_Z(t) \end{aligned} \tag{6.1}$$

$k_{PG}$ calculations were performed comparing values with "ground-truth" constant delay shifts to account for intermediate conversions. MATLAB models were resolved based on minimization of the constrained least-squares error computed across measured and estimated glutamate using a trust-region-reflective algorithm. Prior $k_{PL}$ methods, implemented in similar studies using HP [1-$^{13}$C]pyruvate, were obtained and modified from the Hyperpolarized MRI Toolbox via the Hyperpolarized Technology Resource Center[10]. SVD signal enhancement was performed following Brender et al. on volunteer datasets using MATLAB and MestReNova[11].

$$\mathbf{M} = \sigma_1 \mathbf{u_1} \mathbf{v}_1^T + \sigma_2 \mathbf{u_2} \mathbf{v}_2^T \cdots \sigma_n \mathbf{u}_n \mathbf{v}_n^T = \mathrm{U}\mathbf{\Sigma}\mathbf{V^T} \tag{6.2}$$

From the SVD theorem (6.2), the signal matrix **M** was decomposed into a linear combination of vectors representing spectra (**u**) and corresponding kinetics (**v**) utilizing the separability of the time-independent chemical shift signal[11]. Piecewise [2-$^{13}$C]pyruvate uptake curve data points and corresponding estimated fits were further analyzed for dynamic chemical shift ranges.

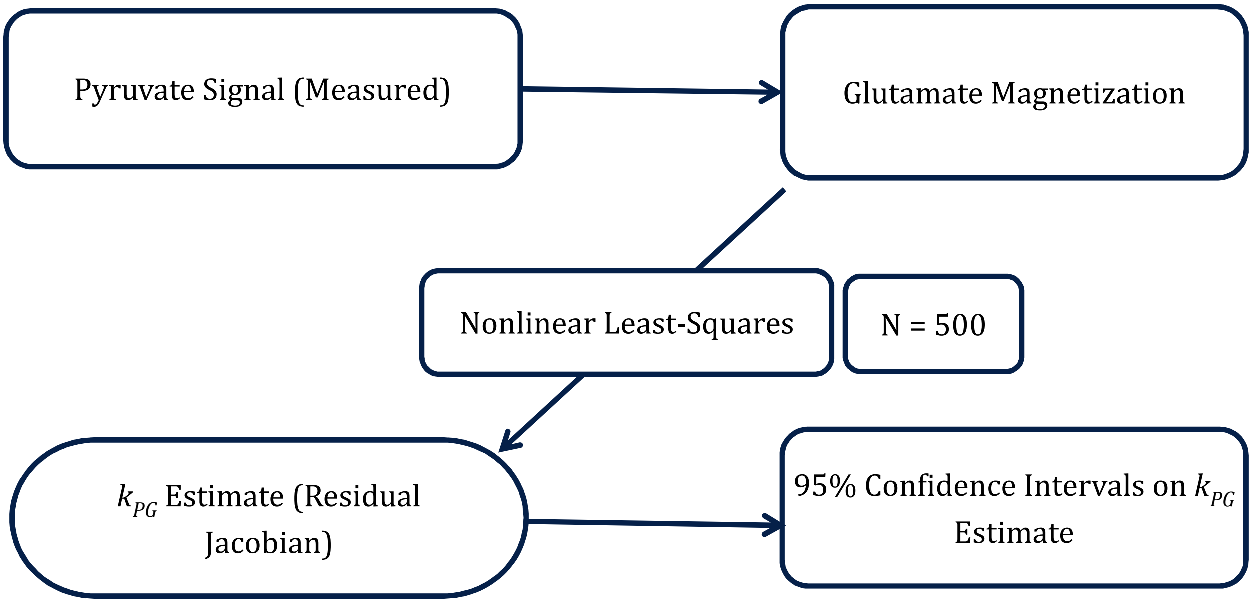

**Figure 6.1:** Input-Less $k_{PG}$ Fit: The measured pyruvate magnetization is the input for the kinetic model at each time point. The glutamate magnetization is then fit using a constrained nonlinear least-squares fit. The benefit to input-less fitting over integral ratios alone includes accounting for variability in delivery times as it is insensitive to bolus delivery using any sampling strategy.

## 6.3 Results

Voxels for improved quantification of $k_{PG}$ rates were compared for highest SNR without spatial or anatomical information. Iterations of centrality metrics detailing inner-voxel kinetics containing anatomical spatial diffusion information utilizing simulation approximations from machine learning training to determine parameters such as ROI boundaries and chemical shift ranges were tested, but not confirmed.

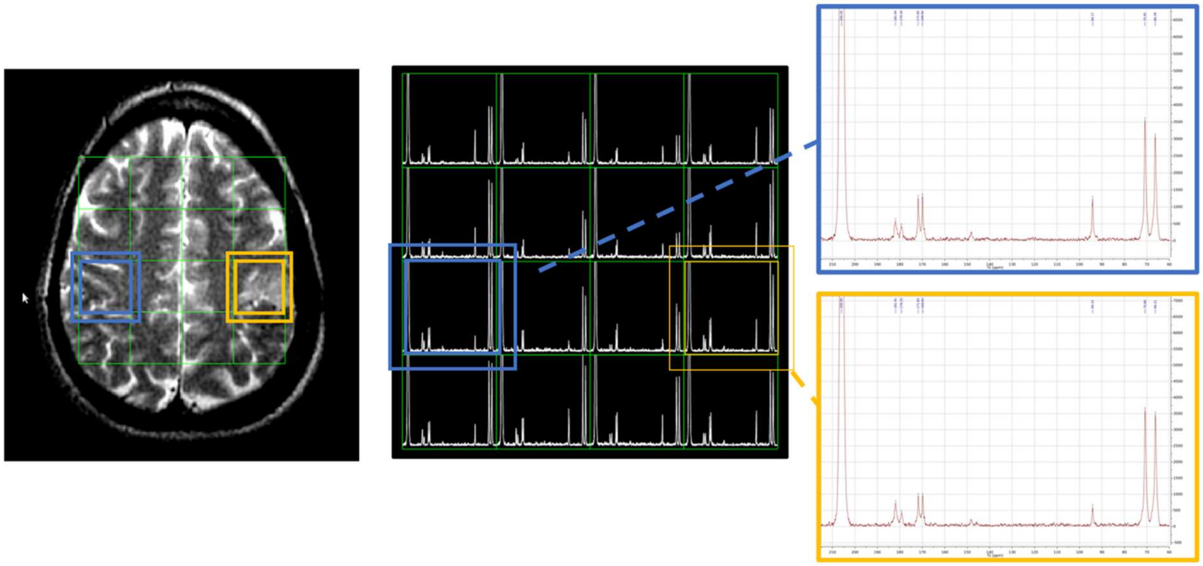

**Figure 6.2:** Voxel comparison of healthy brain (left | up) and tumor (right | down) tissue NMR spectra. Volunteer data acquired using a 32 channel head coil with spectral-spatial excitation: BW = 8 kHz, TR = 20 secs, spatial resolution = 2.5 cm, $\theta_{Pyr}$ = 5°, $\theta_{Mets}$ = 20°.

The $k_{PG}$ values after SVD were found to compare more favorably with AUC ratios. For one model with a constant delay shift of 2 timepoints ( = 4 seconds) with SVD denoising (rank = 10), $k_{PG}$ values were found to increase by a factor of about 1:20, with values ranging from 0.0017 $sec^{-1}$ to 0.0045 $sec^{-1}$. Models also showed similar but not identical inter-subject values. Previously processed and recently acquired [2-$^{13}$C]pyruvate datasets from volunteers showed similar results.

SVD theory indicates a rank approximately equal to the number of metabolite resonances yields ideal noise-free, low-rank approximations. Experimental results demonstrated a slightly greater optimal rank of 10 for low SNR timepoints beyond three $T_1$ decay times.

Figures 6.3 and 6.4 show a representative $k_{PG}$ dataset summed as a linear combination of 10 spectra with greatest SNR before and after SVD with rank = 10. Singular vectors yield dominant noise components. Relative frequency units along the x-axis are shown prior to MestReNova analysis. Figures 6.5 – 6.8 show SVD results using 4 methods: (6.5) No SVD, No Delay ; (6.6) SVD rank = 10, No Delay ; (6.7) No SVD, Delay = 2 seconds ; (6.8) SVD rank = 10, Delay = 2 seconds. Figures 6.9 – 6.12 show corresponding $k_{PG}$ model fits.

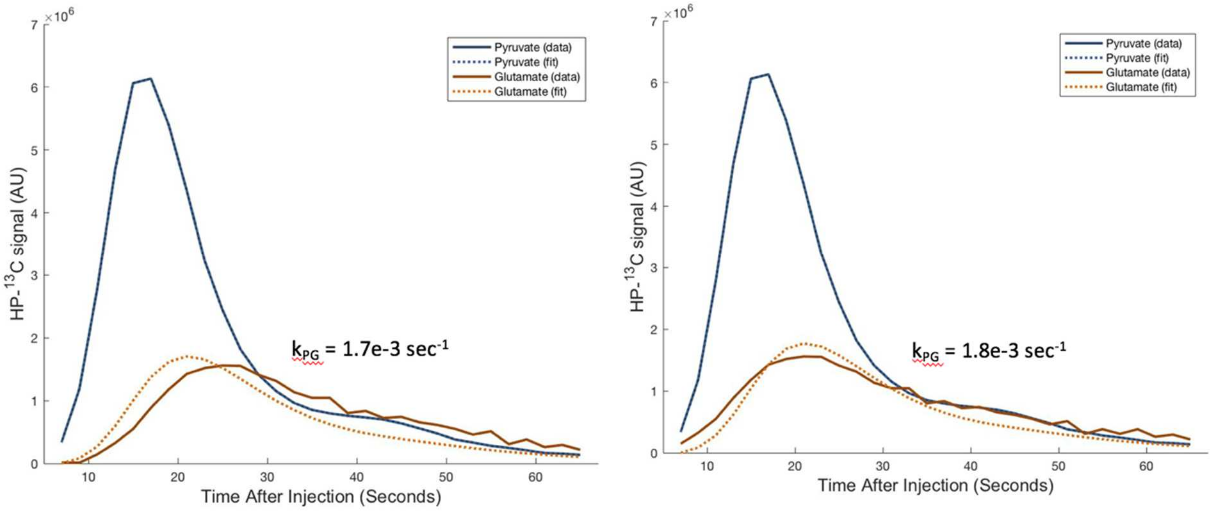

**Figure 6.3:** Representative $k_{PG}$ data and model fits averaged for a volunteer dataset before (left) and after (right) SVD denoising with a constant delay shift of 2 timepoints = 4 seconds.

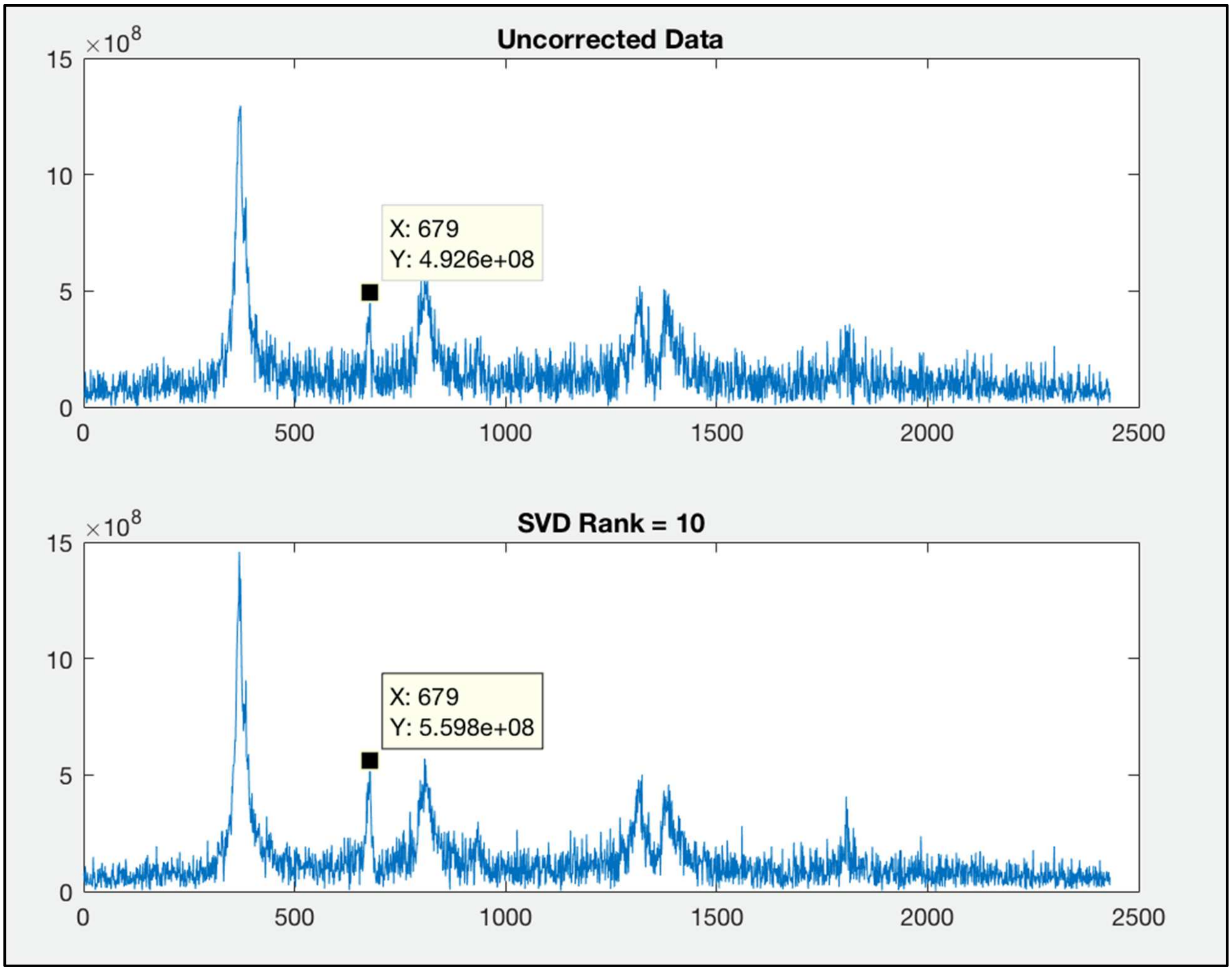

**Figure 6.4:** SVD signal enhancement (rank = 10) performed on a representative summed spectra dataset. This project demonstrated that SVD noise reduction can improve quantification of low-SNR metabolites including HP [5-$^{13}$C]glutamate.

### 6.3.1 Singular Value Decomposition

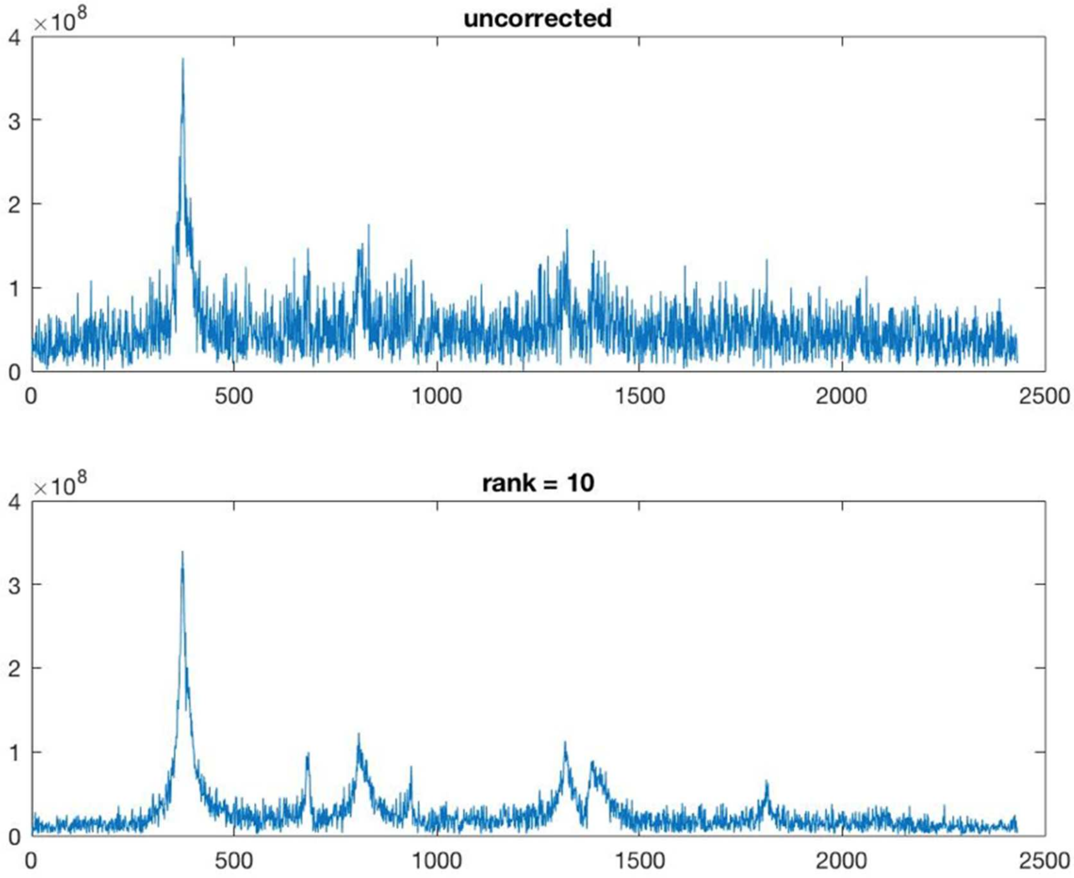

**Figure 6.5:** Method 1 - No SVD, Delay = 0 sec, $k_{PG}$ = 0.0011 sec$^{-1}$

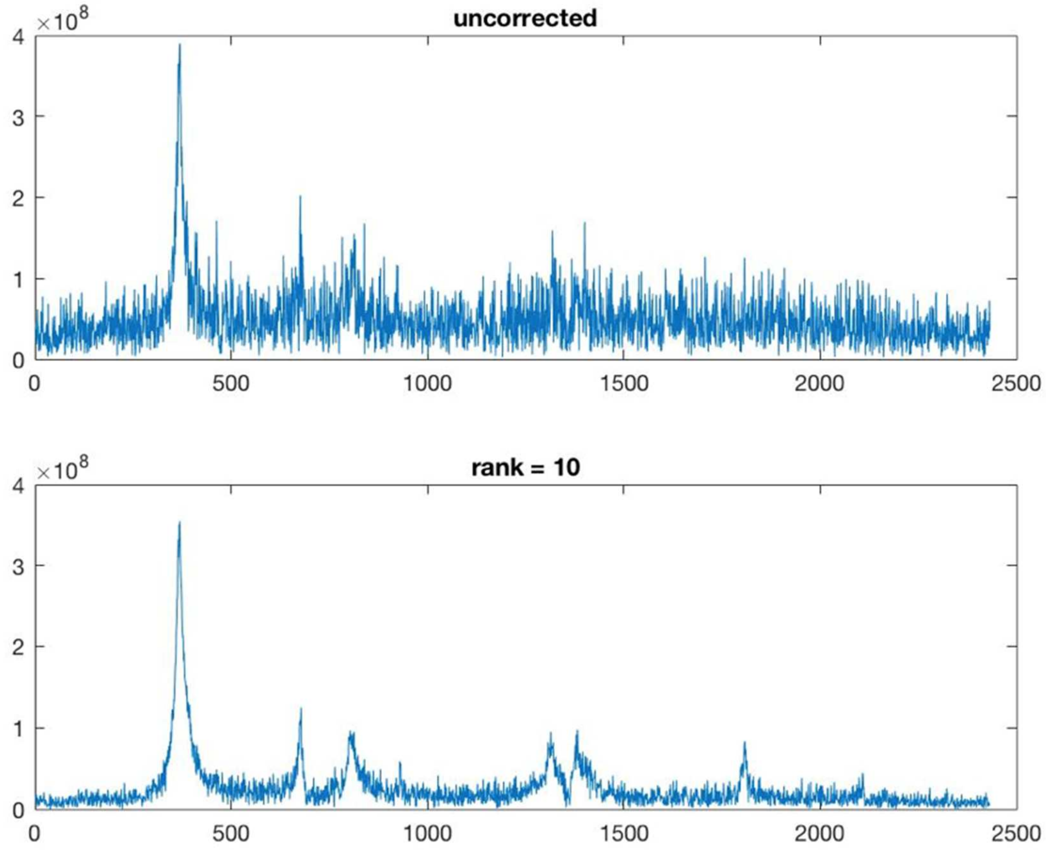

**Figure 6.6:** Method 2 - SVD Rank = 10, Delay = 0 sec, $k_{PG}$ = 0.0011 $sec^{-1}$

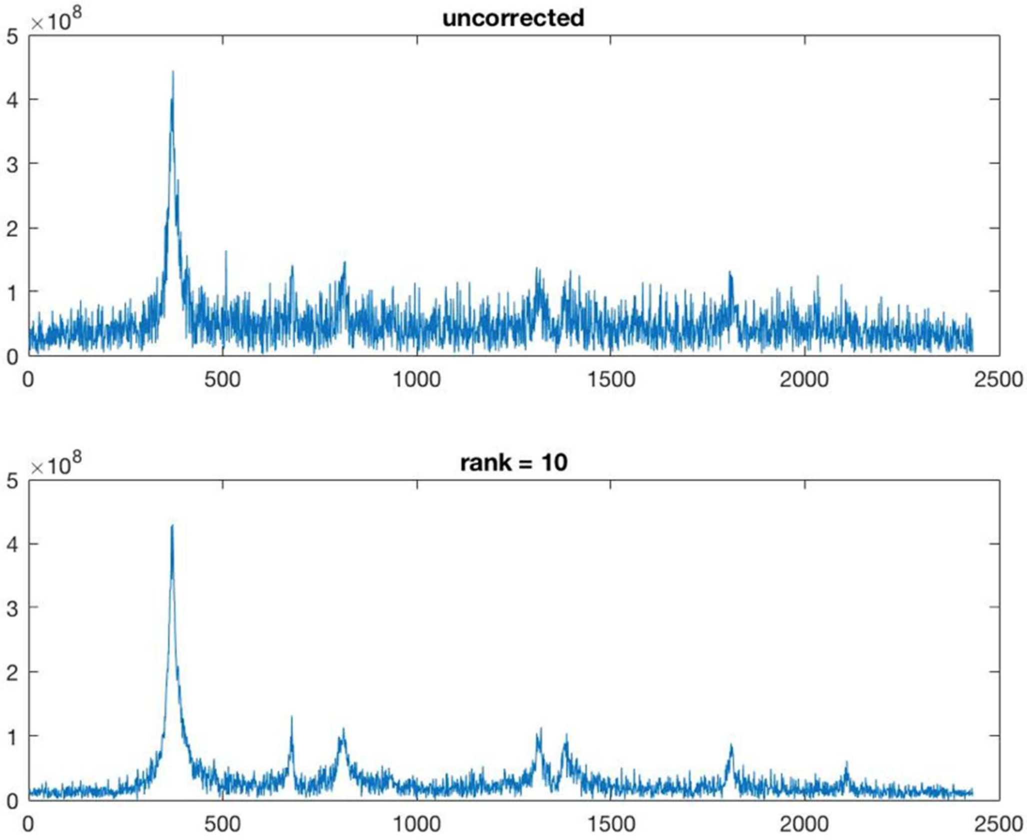

**Figure 6.7:** Method 3 - No SVD, Delay = 4 sec, $k_{PG}$ = 0.0011 sec$^{-1}$

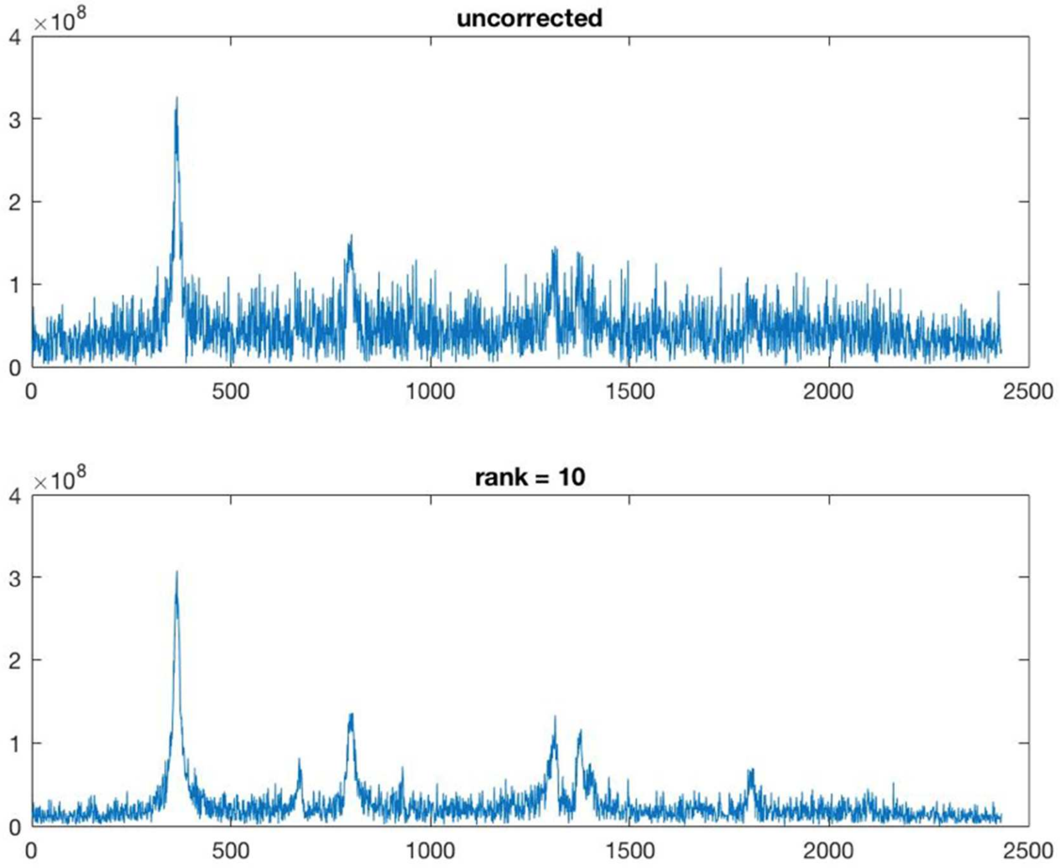

**Figure 6.8:** Method 4 - SVD Rank = 10, Delay = 4 sec, $k_{PG}$ = 0.0012 sec$^{-1}$

### 6.3.2 [2-$^{13}$C]Pyruvate $k_{PG}$ Model Fits

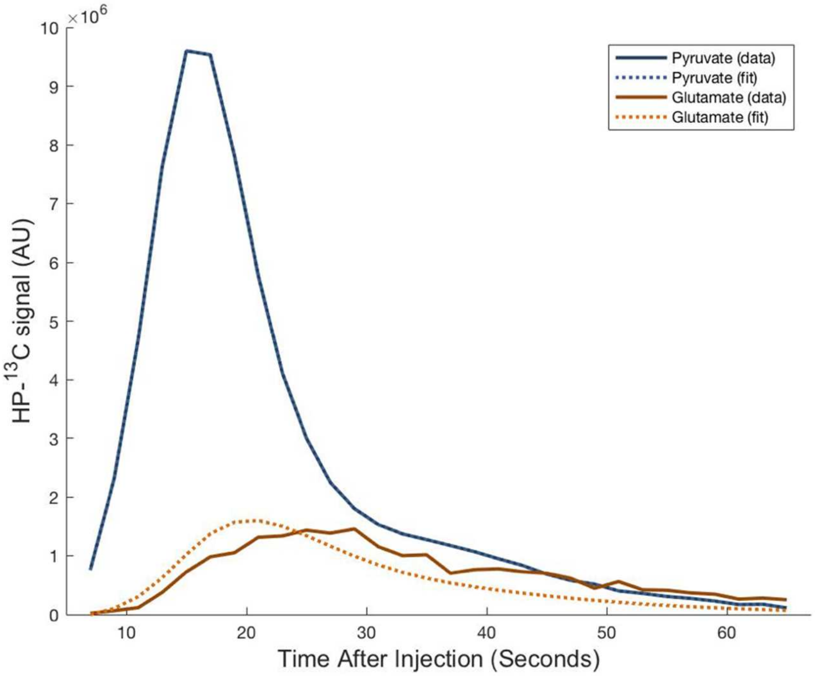

**Figure 6.9:** $k_{PG}$ Fit 1 - No SVD, Delay = 0 sec, $k_{PG}$ = 0.0011 sec$^{-1}$

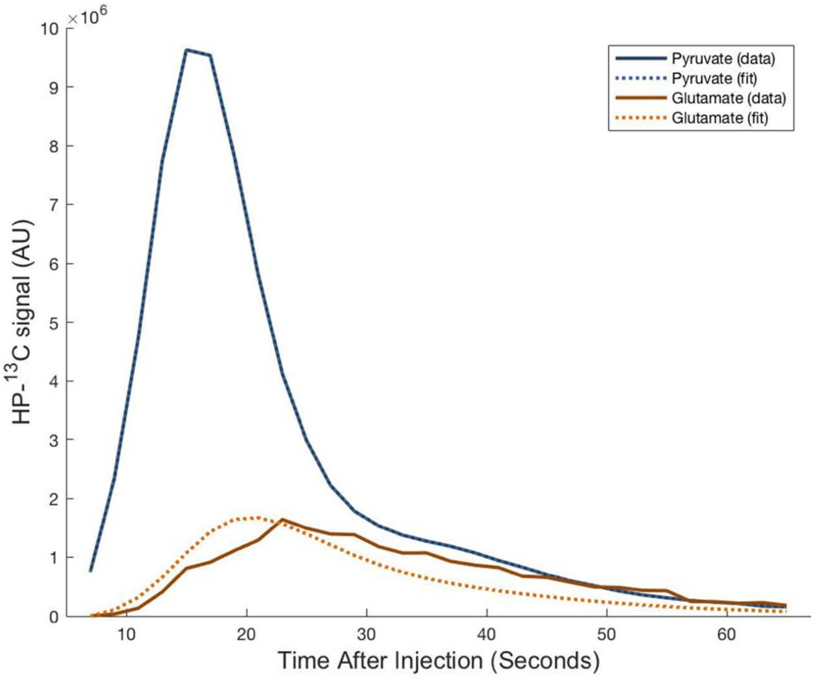

**Figure 6.10:** $k_{PG}$ Fit 2 - SVD Rank = 10, Delay = 0 sec, $k_{PG}$ = 0.0011 sec$^{-1}$

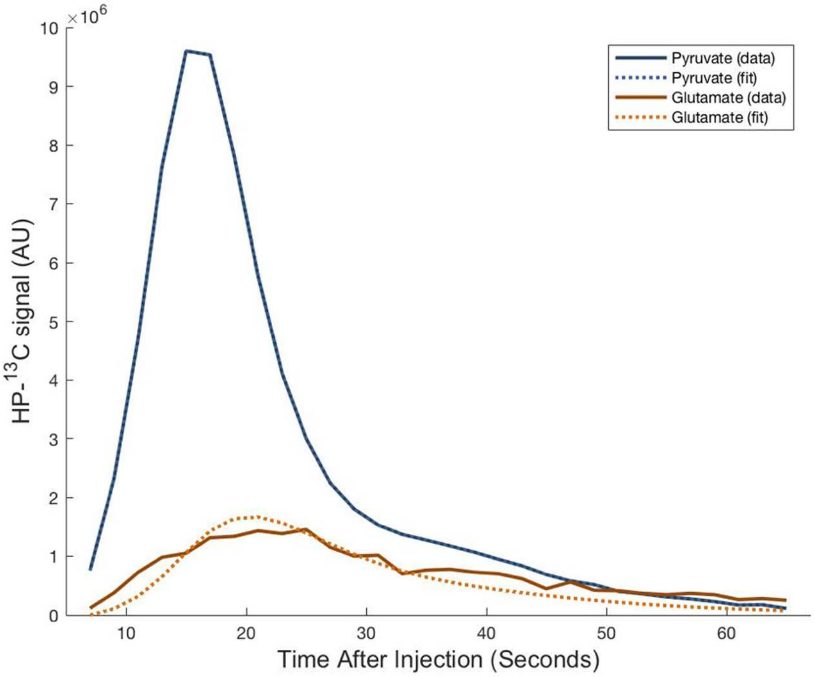

**Figure 6.11:** $k_{PG}$ Fit 3 - No SVD, Delay = 4 sec, $k_{PG}$ = 0.0011 sec$^{-1}$

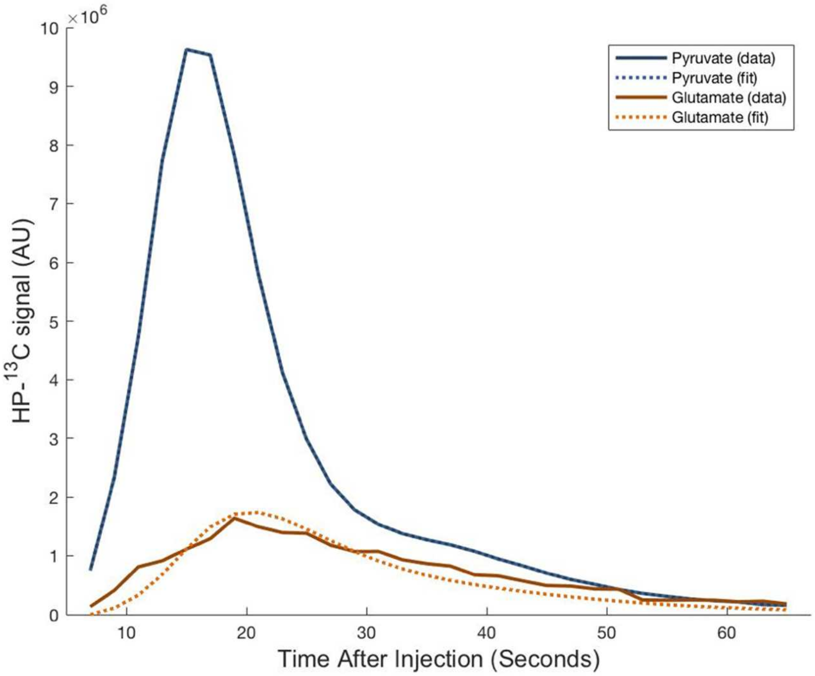

**Figure 6.12:** $k_{PG}$ Fit 4 - SVD Rank = 10, Delay = 4 sec, $k_{PG}$ = 0.0012 sec$^{-1}$

## 6.4 Discussion & Future Directions

Non-invasive detection of alterations in metabolic flux may offer prognostic value and improve monitoring of treatment response[12,13]. In a prior clinical research investigation using HP [1-$^{13}$C]pyruvate[2], a total of 10 brain tumor patients were scanned using an EPI sequence and statistical analysis suggested an input-less model provided the best agreement with data. In addition, post-fitting error criteria to select voxels was found to improve precision than SNR cutoffs alone.

In this work, measured values and calculated mean and standard error across volunteers were consistent within expected ranges. Results were further in agreement with a larger set of data from previous $k_{PL}$ studies using [1-$^{13}$C]pyruvate. Observed noise variations in datasets may be attributed to multiple factors including subject brain volumes and polarization levels. Overall $k_{PG}$ values ranged from 0.0010 sec$^{-1}$ to 0.0045 sec$^{-1}$ with values less than 50% that of average $k_{PL}$ values, and were lower than expected from AUC ratios suggesting further improvements to the kinetic model. Prior conceptions may be challenged to find values close to 75%.

For representative models with SVD rank = 10 and delay = 4 seconds, $k_{PG}$ fits improved with values increasing about 10%. Observed noise variations across datasets may be attributed to multiple factors including subject brain volumes and polarization levels. Experimental results demonstrated an optimal rank of 10 for low SNR timepoints, extending beyond three $T_1$ decay times. Reasons may include low confidence in the separability of the spectra, such that "phantom" eigenvectors in low signal regions may encapsulate valuable signal without appropriate destructive interference. In one comparable study it was found that at higher levels of noise, the metabolite signal possessed a slight tendency to drift towards the kinetics of the stronger pyruvate signal, and a hypothesized origin of error at low SNR stemmed from the 4th and 5th eigenvectors corresponding to a single metabolite[11]. For $[2\text{-}^{13}\mathrm{C}]$pyruvate, the chemical shift range containing TCA cycle intermediates near 180 ppm is particularly challenging to resolve and the low SNR regime is often at risk to even minor phase and baseline corrections[16]. Machine learning with simulated training may seek to further optimize data processing for more accurate peak quantification, with neural network architectures serving to perform these functions[14,19-21].

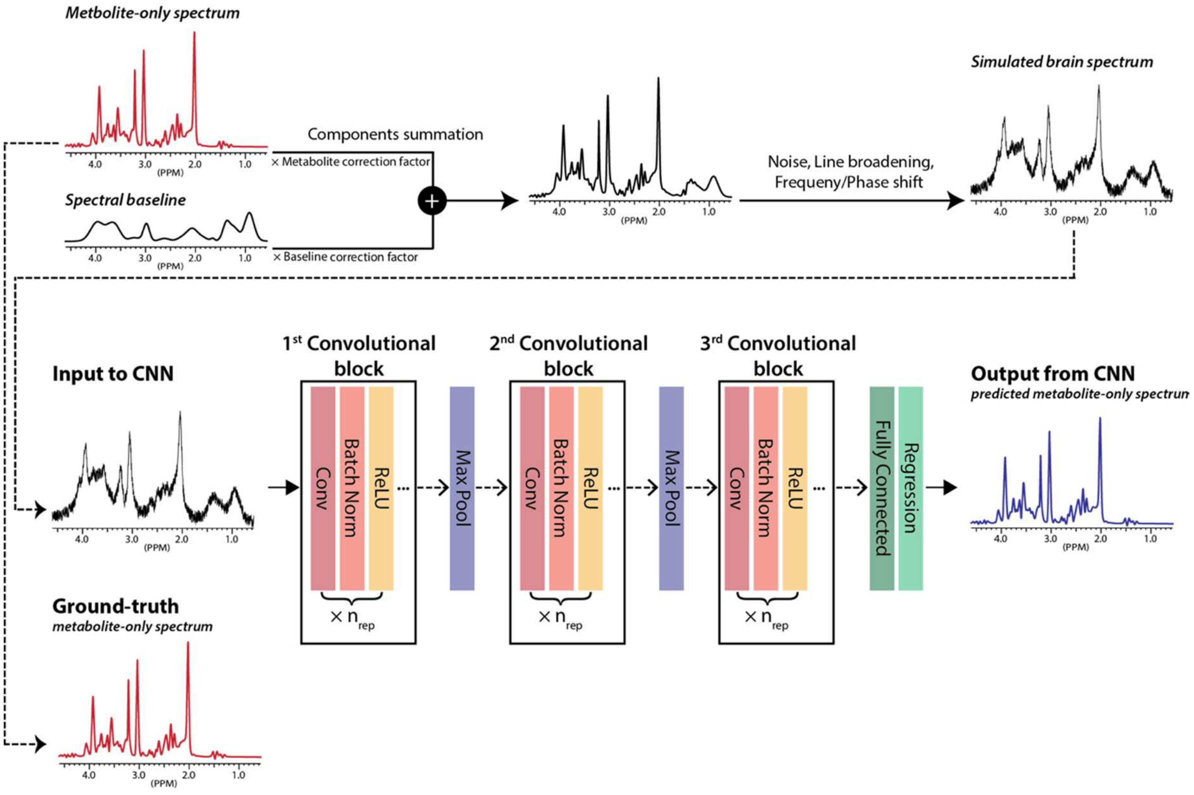

**Figure 6.13:** Schematic of architecture and training using a convolutional neural network (CNN) to simulate spectral brain data for improved quantification. The CNN was trained to improve on data with low SNR while testing misregistered linewidth, phase shift, and spectral baseline limits. Adapted from Lee et al. [14].

In considering complex networks such as those postulated by biologists as landscapes for human metabolism[15,16], centrality metrics seeking to capture and preserve individual nodal characteristics while simultaneously considering neighboring behavior may be considered[17,18]. However self-organization in metabolism may exist only when a forward drive is predictable. Katz centrality has been found the best predictor among several methods for correlating neurons with firing rates given a neural network structure, including for purely excitatory and excitatory-inhibitory networks, with either homogeneous connections or small-world structure[17].

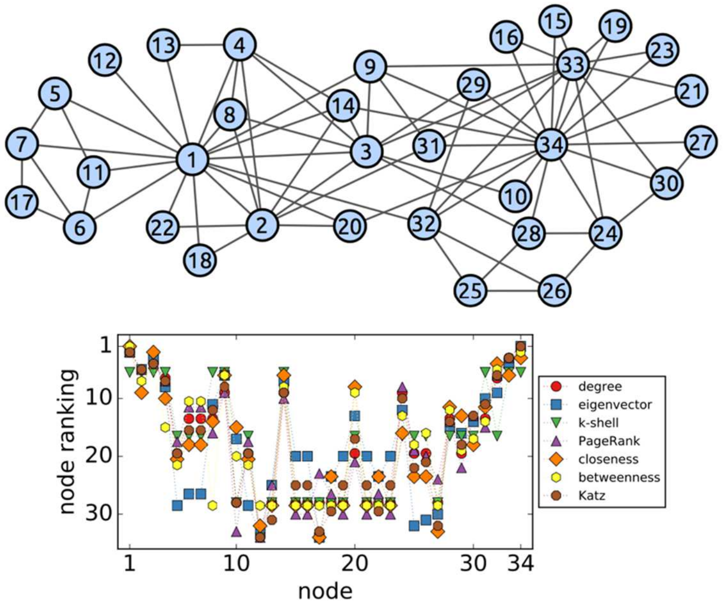

**Figure 6.14:** Nodal ranking methods using centrality metrics illustrating disparate characterizations through vector representations of this often-studied network with 34 nodes and 78 links. Adapted from Liao et al. [17].

In Figure 6.14 multiple independent methods may be used to order or rank a network. Both the network structure, with features such as connectedness and path length, and the nodal ranking method considered, including eigenvector and PageRank, affects nodal relationships through measured activity and influence[17].

While a multitude of engineering advancements benefit from phenomenological symmetries in nature through mathematics, complex systems with examples ranging from discrete Markov chains to non-uniform diffusion to economic markets feature “broken” symmetries of heterogeneous interacting parts. One traditional approach to discern patterns in complex systems is to investigate remnant local symmetries to serve as potential building blocks if remaining functional – another approach is to assume no symmetries and identify common behavior from uniform prior knowledge[22].

Further improvements extending beyond the two-site model include dynamic delay times employing Bayesian statistics linking enzymatic activity with uptake rates through bolus tracking. In one experiment design, a Bayesian inference forward model may approximate dynamics by Brownian diffusion in configuration space and update damping voxel ranking parameters with AUC trends.

## 6.5 Summary

Novel methods were investigated and compared to improve quantification of HP [2-$^{13}$C]pyruvate to [5-$^{13}$C]glutamate in human brain volunteer data. By incorporating SVD denoising and signal processing techniques with delay shifts, $k_{PG}$ values ranging from 0.0017 sec$^{-1}$ to 0.0045 sec$^{-1}$ were calculated and found to favorably compare with AUC ratios. These methods may be utilized for future studies of localized metabolic kinetic rates, such as to investigate manifested effects of poor sleep quality on neurometabolism.

# References

[1] Larson PEZ, Chen HY, Gordon JW, et al. Investigation of analysis methods for hyperpolarized 13C-pyruvate metabolic MRI in prostate cancer patients. NMR Biomed. 2018;31(11):e3997. doi:10.1002/nbm.3997.

[2] Mammoli D, Gordon J, Autry A, et al. Kinetic Modeling of Hyperpolarized Carbon-13 Pyruvate Metabolism in the Human Brain. IEEE Trans Med Imaging. 2020;39(2):320-327. doi:10.1109/TMI.2019.2926437.

[3] Chung BT, Chen HY, Gordon J, et al. First hyperpolarized [2-13C]pyruvate MR studies of human brain metabolism. J Magn Reson. 2019;309:106617. doi:10.1016/j.jmr.2019.106617.

[4] Anderson NM, Mucka P, Kern JG, Feng H. The emerging role and targetability of the TCA cycle in cancer metabolism. Protein Cell. 2018;9(2):216-237. doi:10.1007/s13238-017-0451-1.

[5] Kim AY, Baik EJ. Glutamate Dehydrogenase as a Neuroprotective Target Against Neurodegeneration. Neurochem Res. 2019;44(1):147-153. doi:10.1007/s11064-018-2467-1.

[6] Park JM, Josan S, Grafendorfer T, et al. Measuring mitochondrial metabolism in rat brain in vivo using MR Spectroscopy of hyperpolarized [2-$^{13}$C]pyruvate. NMR Biomed. 2013;26(10):1197-1203. doi:10.1002/nbm.2935.

[7] Datta K, Spielman D. MRI of [2-13C]Lactate without J-coupling artifacts. Magn Reson Med. 2021;85(3):1522-1539. doi:10.1002/mrm.28532.

[8] Autry AW, Gordon JW, Carvajal L, et al. Comparison between 8- and 32-channel phased-array receive coils for in vivo hyperpolarized 13 C imaging of the human brain. Magn Reson Med. 2019;82(2):833-841. doi:10.1002/mrm.27743.

[9] Bottomley PA, Griffiths JR, et al. Handbook of magnetic resonance spectroscopy in vivo: MRS theory, practice and applications. John Wiley & Sons, 2016.

[10] Hyperpolarized MRI Technology Resource Center. Hyperpolarized MRI Toolbox. (2021 December). https://hyperpolarizedmri.ucsf.edu.

[11] Brender JR, Kishimoto S, Merkle H, et al. Dynamic Imaging of Glucose and Lactate Metabolism by 13C-MRS without Hyperpolarization. Sci Rep. 2019;9(1):3410. Published 2019 Mar 4. doi:10.1038/s41598-019-38981-1.

[12] Milshteyn E, von Morze C, Reed GD, et al. Development of high resolution 3D hyperpolarized carbon-13 MR molecular imaging techniques. Magn Reson Imaging. 2017;38:152-162. doi:10.1016/j.mri.2017.01.003.

[13] Sriram R, Kurhanewicz J, Vigneron DB. Hyperpolarized Carbon-13 MRI and MRS Studies. Encyclopedia of Magnetic Resonance. J. Griffiths and P. Bottomley. eMagRes. 3: 1-14. John Wiley & Sons, 2014. doi: 10.1002/9780470034590.emrstm1253.

[14] Lee HH, Kim H. Intact metabolite spectrum mining by deep learning in proton magnetic resonance spectroscopy of the brain. Magn Reson Med. 2019;82(1):33-48. doi:10.1002/mrm.27727.

[15] Morice S, Pincebourde S, Darboux F, Kaiser W, Casas J. Predator-prey pursuit-evasion games in structurally complex environments. Integr Comp Biol. 2013;53(5):767-779. doi:10.1093/icb/ict061.

[16] Lee CY, Soliman H, Geraghty BJ, et al. Lactate topography of the human brain using hyperpolarized 13C-MRI. Neuroimage. 2020;204:116202. doi:10.1016/j.neuroimage.2019.116202.

[17] Liao H, Mariani MS, Medo M, Zhang YC, Zhou MY. Ranking in evolving complex networks. Physics Reports. 2017;689:1-54. doi:10.1016/j.physrep.2017.05.001.

[18] Fletcher JM, Wennekers T. From Structure to Activity: Using Centrality Measures to Predict Neuronal Activity. Int J Neural Syst. 2018;28(2):1750013. doi:10.1142/S0129065717500137.

[19] Lan L, You L, Zhang Z, et al. Generative Adversarial Networks and Its Applications in Biomedical Informatics. Front Public Health. 2020;8:164. Published 2020 May 12. doi:10.3389/fpubh.2020.00164.

[20] Sun L, Wang J, Huang Y, Ding X, Greenspan H, Paisley J. An Adversarial Learning Approach to Medical Image Synthesis for Lesion Detection. IEEE J Biomed Health Inform. 2020;24(8):2303-2314. doi:10.1109/JBHI.2020.2964016.

[21] Alex V, Mohammed Safwan KP, Chennamsetty SS, Krishnamurthi G. Generative adversarial networks for brain lesion detection. SPIE Medical Imaging, International Society for Optics and Photonics, 2017.

[22] Hassanien AE, Grosan C, et al. Applications of intelligent optimization in biology and medicine. Springer; 2016. pp. 289–307.

# Chapter 7

# Utilizing [2-$^{13}$C]Pyruvate Developments for the Design of Neuropathologies and Sleep Studies

*Adam Autry, Brian Chung, Hsin-Yu Chen, Jeremy Gordon, Marisa Lafontaine, Susan Chang, Javier Villanueva-Meyer, Peder Larson, Daniel Vigneron, Yan Li, CBMT-36. INITIAL EXPERIENCE WITH HYPERPOLARIZED [2-$^{13}$C]PYRUVATE MR IMAGING IN PATIENTS WITH IDH-MUTANT GLIOMA, Neuro-Oncology, Volume 21, Issue Supplement 6, Nov 2019. https://doi.org/10.1093/neuonc/noz175.158.*

## 7.1 Application: IDH-Mutant Glioma

The following section summarizes the initial patient experience of using HP [2-$^{13}$C]pyruvate to acquire brain tumor MR HP $^{13}$C spectroscopic imaging data in patients with IDH-mutant gliomas measuring both aerobic glycolysis ([2-$^{13}$C]lactate) and oxidative metabolism ([5-$^{13}$C]glutamate) for rapid application. Isocitrate dehydrogenase (IDH) is an essential enzyme that catalyzes the oxidative decarboxylation of isocitrate and plays a key role in TCA cycle metabolism[1]. However, many brain tumors exhibit a mutation in this enzyme resulting in the production of 2-hydroxyglutarate (2HG) instead of glutamate[28].

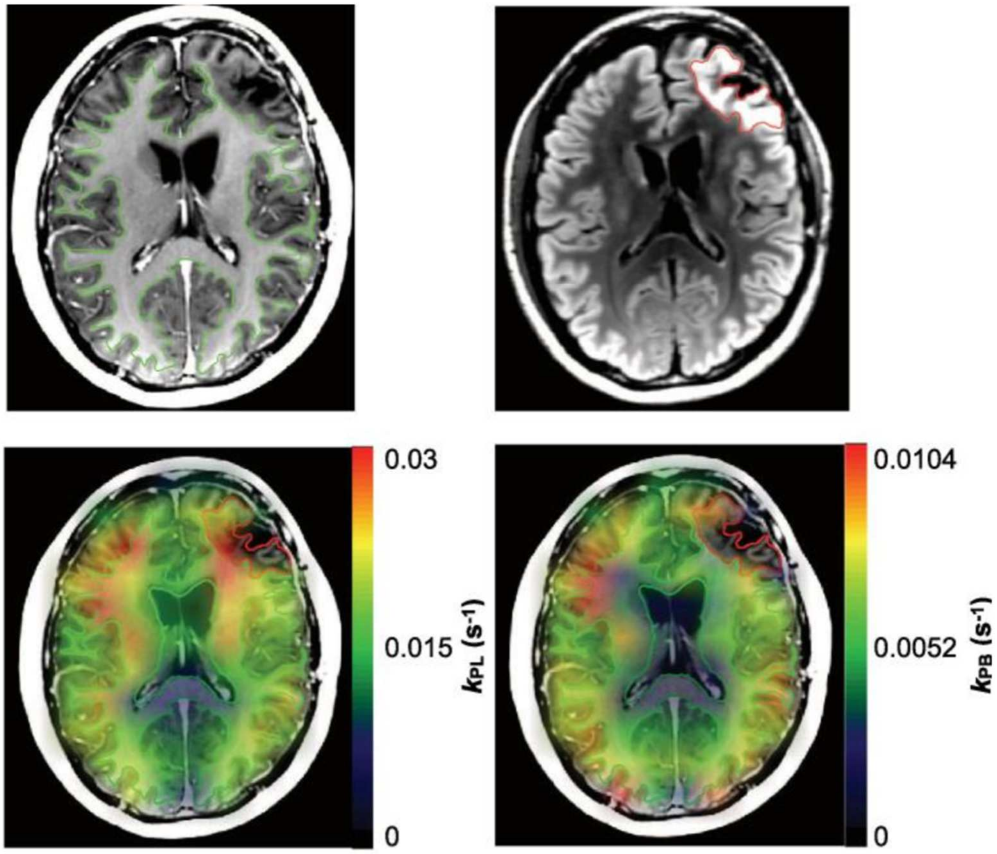

**Figure 7.1:** T$_1$-weighted images and overlaid maps of $k_{PL}$ and $k_{PB}$ based on kinetic modeling dynamic HP $^{13}$C EPI data acquiring [1-$^{13}$C]pyruvate, [1-$^{13}$C]lactate and [1-$^{13}$C]bicarbonate signal. Adapted from Autry et al. [2].

An initial imaging study of [1-$^{13}$C]pyruvate metabolism in normal-appearing white matter (NAWM) compared volunteers and patients to evaluate variation across exams and assess metabolism in tumor lesions for alterations relative to NAWM[2]. Figure 7.1 shows images and maps used to characterize serial dynamic HP $^{13}$C images with a kinetic modeling approach in healthy volunteers and glioma patients who received treatment. Serial measures of HP [1-$^{13}$C]pyruvate metabolism displayed consistency in the NAWM of healthy volunteers and patients. Both $k_{PL}$ and $k_{PB}$ values were globally elevated following bevacizumab treatment while progressive disease demonstrated elevated $k_{PL}$ in gadolinium-enhancing and non-enhancing lesions[2].

Prior $^{13}$C metabolic flux analysis suggested IDH1-mutant cells exhibit increased oxidative TCA cycle and suppressed glutamine metabolism[3]. It was hypothesized HP [2-$^{13}$C]pyruvate could provide additional information to HP [1-$^{13}$C]pyruvate investigating altered metabolism in IDH-mutant gliomas.

Two patients who presented with IDH-mutant gliomas (43 year-old male, grade II astrocytoma, RT/TMZ; 33 year-old female, grade III oligodendroglioma, no RT/TMZ) were considered radiologically stable post resection and imaged using a 2D MR spectroscopic imaging (MRSI) sequence (spatial resolution = 15.6 cm$^3$ – 18.8 cm$^3$, acquisition time = 20 sec) following injection of 0.43mL/kg of 250mM HP [2-$^{13}$C]pyruvate. Proton MRI exams revealed no gadolinium enhancing lesions.

HP [2-$^{13}$C]pyruvate, [5-$^{13}$C]glutamate and [2-$^{13}$C]lactate resonances were quantified within a lesion voxel and contralateral normal-appearing voxel. Proton images were aligned to HP data enabling quantification of apparent diffusion coefficients (ADC), perfusion peak height (PH), and MR spectroscopy choline-to-N-acetyl-aspartate indices (CNI). ADC (nADC) and PH (nPH) values were normalized by the median value in NAWM.

For the T2-hyperintense lesion (T2L) in Patient#1/Patient#2: volume T2L = 18.4/4.2cc; median ADC T2L = 1.86/1.64; max CNI T2L = 3.2/6.5; 90th percentile nPH T2L = 1.09/2.11.

HP data displayed maximum signal-to-noise ratios (SNR) for [2-$^{13}$C]pyruvate, [5-$^{13}$C]glutamate, and [2-$^{13}$C]lactate of 1360, 44 and 400 respectively. HP CSI data for Patient #1/Patient#2 contained 15.9/13.7 (%T2L); 15.1/4.1 (%NAWM); 15.7/22.0 (%GM) in selected lesion voxels while contralateral voxels 100 (%NAWM).

Lesions demonstrated reduced HP glutamate/pyruvate ratios [#1: 0.0089/0.0102 (lesion/normal voxel); #2: 0.0170/0.0269] and elevated HP glutamate-to-glutamine ratios in both patients [#1: 0.81/0.66; #2: 0.84/0.66].

In summary initial patient experience with HP [2-$^{13}$C]pyruvate showed adequate SNR for quantifying HP [2-$^{13}$C]pyruvate, [5-$^{13}$C]glutamate and [2-$^{13}$C]lactate resonances. Future studies will optimize imaging protocols and expand patient cohorts to further evaluate aberrant metabolic reprogramming related to IDH-mutant tumors.

## 7.2 Early-Stage Neurodisorders

Metabolic changes are increasingly recognized as key players in neurodisorders, with energetic imbalance and aberrant metabolism implicated in most neurodegenerative disease including Alzheimer’s, Parkinson’s, Huntington’s diseases and multiple sclerosis[8,13,28]. Similar to upregulated enzymatic activity in cancer, multiple causes of metabolic alterations from normal activity may occur directly or indirectly to the brain tissue itself or from systemic modifications[10]. Recently sleep and wakefulness have been found to produce distinct plasticity effects on neuronal networks in keeping with *predictive coding* - the brain contains a representation of the reality used during wakefulness for unconscious inference[11].

Studies have shown norepinephrine levels are correlated with total REM duration and enhanced fatty acid oxidation through increased flux of acetyl-CoA. Norepinephrine may also induce processing of the sole residual mismatch between external information and inner model linked via a dramatic improvement in energy efficiency[28,30]. Similar to pseudo-progression in tumors resulting from allergic reaction inflammation, early-stage neurodisorders may be misregistered threats.

### 7.2.1 Schizophrenia

Associated with elevations in glutamatergic metabolites across several brain regions, a recent analysis of $^1$H MRS studies totaling 1686 schizophrenic patients and 1451 healthy individuals found significant elevations of glutamate in the basal ganglia of schizophrenic patients, however no region showed reduction of glutamate[4]. Secondary analyses revealed that elevated medial frontal levels were evident in individuals at high risk for schizophrenia but not in those with first-episode psychosis or chronic schizophrenia. Elevated glutamate and glutamine in the medial temporal lobe was seen with chronic schizophrenia but not in high-risk or first-episode groups[4]. In another study schizophrenic patients with different outcomes entered with similar putamen and caudate nucleus volumes[29]. Putaminal but not caudal volumes were significantly smaller at the time of follow-up, hence the rate of decline in volumes of the putamen were greatest in patients with poor outcomes. Caudate volumes were lower in schizophrenia patients than healthy subjects, both at baseline and follow-up.

Further imaging studies have initially suggested general hypometabolism resulting from mitochondrial enzyme deficiencies, with increased activity of dehydrogenases in later sections of the TCA cycle potentially reflecting a compensatory response to reduced earlier activity[5,12].

### 7.2.2 Bipolar Disorder

Bipolar disorder and schizophrenia share common clinical features with family, twin and adoption studies showing a genetic correlation of around 0.6 substantiating evidence for partial overlap of genetic influences[6].

A recent review for post-mortem, pharmacological, fMRI and molecular imaging studies of dopamine function in bipolar disorder that a state of hyperdopaminergia underlies manic phases and increased dopamine transporter levels underlies depressive phases, but changes in other aspects of dopaminergic function were inconsistent leading to speculation a failure of dopamine receptor and transporter homoeostasis may underlie the pathophysiology of this disorder[7].

Dopamine and glutamate systems cross-talk at multiple levels such as the postsynaptic density, a structural and functional protein mesh implicated in dopamine and glutamate-mediated synaptic plasticity[28]. Brain pyruvate, lactate and glutamate levels are elevated in bipolar disorder[9].

## 7.3 Anesthesia

Brain activity during wakefulness is frequently associated with high metabolic rates for supporting information processing and memory encoding. During sleep, cerebral aerobic glycolysis and lactate concentration is reduced, while neuronal TCA metabolism may be correlated with sleep-state dependent sympathetic activation in the brain stem and spinal cord[14].

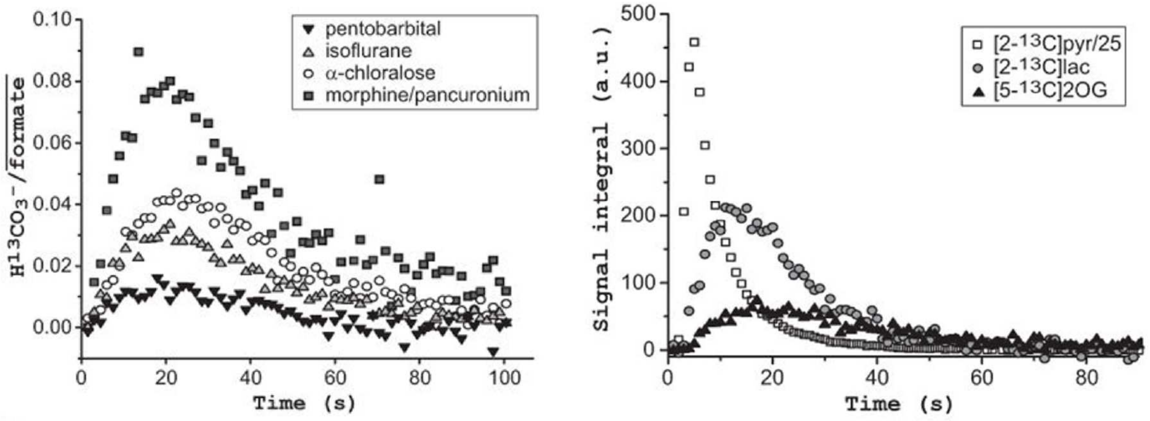

**Figure 7.2:** *In vivo* time courses measured in rats after injection of HP [1-$^{13}$C]pyruvate to bicarbonate (left) and HP [2-$^{13}$C]pyruvate to [2-$^{13}$C]lactate and [5-$^{13}$C]2-oxoglutarate (right) into femoral vein under different anesthesia. TR = 1.5 second (left) and 1 second (right). Adapted from Marjańska et al. [15].

Figure 7.2 shows a recent study using HP [1-$^{13}$C]pyruvate and HP [2-$^{13}$C]pyruvate measuring brain metabolism in two rats during anesthetized sleep[15]. Single-shot $^{1}$H decoupled $^{13}$C spectra were acquired following injection of HP solution into the femoral veins under anesthesia at the same time point from beginning of injection. For HP [1-$^{13}$C]pyruvate, time courses show integrals of bicarbonate signal following administration of four types of anesthesia demonstrating varying levels of sensitivity. HP [2-$^{13}$C]pyruvate time courses under morphine show significantly increased detection of downstream [5-$^{13}$C]2-oxoglutarate, another name for α-ketoglutarate, and citrate, another TCA cycle intermediate.

Extended sleep disruption may lead to a state of sustained microglia activation and perhaps increase the brain's susceptibility to other forms of damage[20-22]. Experimental evidence supports a cerebral metabolic shift taking place during sleep suppressing aerobic glycolysis[16]. While it is unknown whether or how astrocytes regulate reciprocal neuronal activity to promote sleep and wake cycles, a recent study showed within the lateral hypothalamus a glutamate transporter mainly present on astrocytes (GLT1) distinctly modulates excitatory transmission in a cell-type-specific manner and according to sleep history[20]. Rapid and substantial decreases in glucose tolerance have been found to suggest neuronal activity during slow wave sleep (SWS) may be an important determinant of glucose homeostasis, independently of sleep duration[17].

In a 2016 positron emission tomography (PET) imaging study, young narcoleptic patients presented hypometabolism in the right mid-frontal lobe and angular gyrus, and hypermetabolism in the olfactory lobe, hippocampus, parahippocampus, amygdala, fusiform, left inferior parietal lobe, left superior temporal lobe, striatum, basal ganglia, thalamus, right hypothalamus, and pons compared to controls[18].

Brain concentration of lactate varies as a function of sleep state, and similar to slow wave activity (SWA) in the electroencephalogram (EEG) it increases as a function of time spent awake or in rapid eye movement sleep and declines as a function of time spent in slow wave sleep (SWS). These distinct temporal dynamics render the hypothesis that SWA is a direct function of lactate concentration untenable: lactate concentration approaches asymptote values within less than an hour whether increasing or decreasing, while SWA drive continues to build over periods of hours of wakefulness[19].

## 7.4 Study Designs

In healthy volunteers following sleep disruption or poor quality of sleep, we may observe increased TCA cycle metabolism particularly in the basal ganglia if there is compensatory behavior to account for lack of SWS. This increase in TCA cycle metabolism may be noticeable in the mornings and exacerbated in the afternoons.

In one study design, a cohort of healthy volunteers ranging in age and gender may self-report quality of sleep and seek metabolic imaging in the same 24-hours and repeat scans the following day. Student populations in the United States may volunteer as available initial cohorts representing diverse backgrounds and lifestyles with a potentially lower likelihood for previously diagnosed neurodisorders.

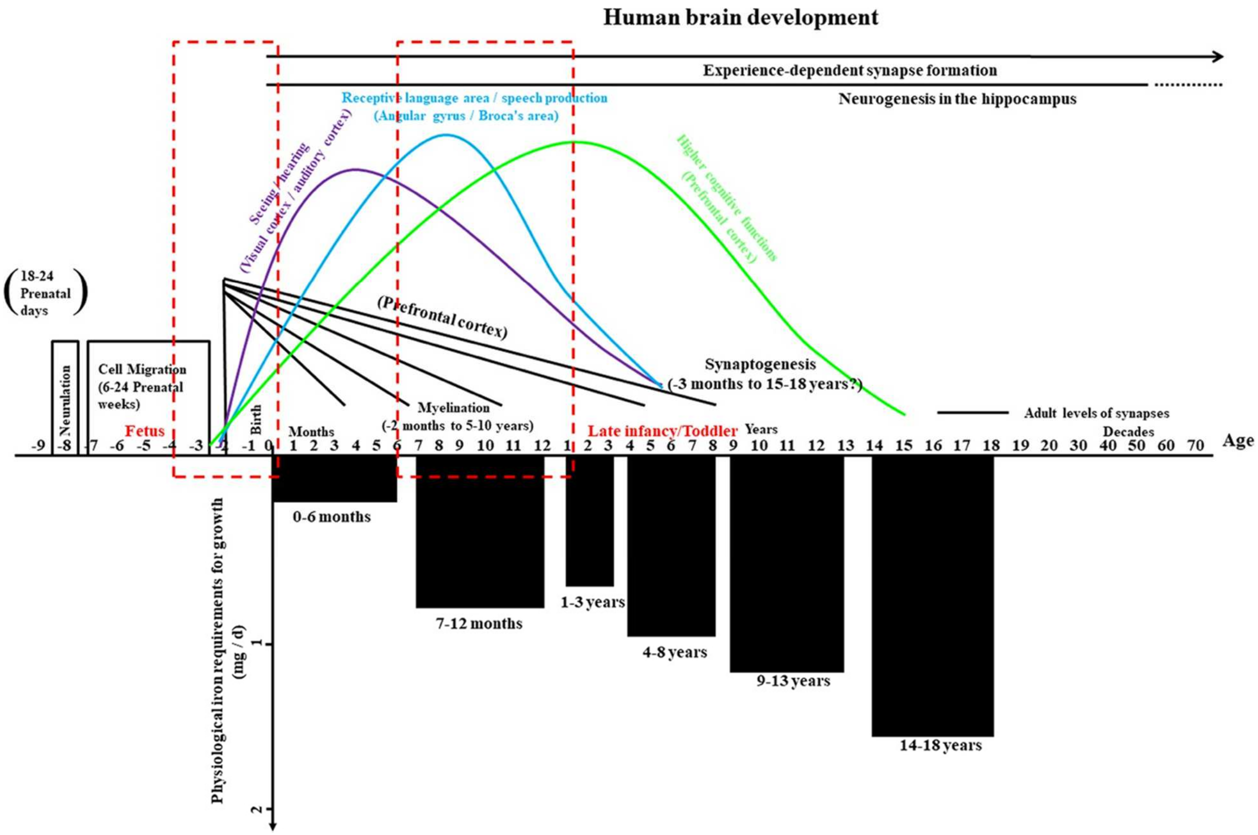

**Figure 7.3:** Overview of human brain development and physiological requirement of iron for growth in infancy and childhood. The upper part illustrates important prenatal events and the lower shows physiological requirements for growth in different stages during infancy and childhood. Similar study designs may seek to qualify stages of development measuring TCA cycle metabolism and quality of sleep. Adapted from Wang et al. [22].

Cognitive routine, physiological development and similar potential indicators for continued growth may be noted as more or less adaptive for a given age and pertinent to critical claims in developmental neuroscience of brain development as a lifelong process[23]. Several lines of evidence support a hypothesis that eating patterns reducing or eliminating nighttime eating and prolonging nightly fasting intervals may result in sustained improvements to human health[25,26]. Such studies investigating physiological mechanisms leading to improved health outcomes may elucidate imperative appetite and sleep connectedness via circadian biology compared with diverse gut microbiomes or modifiable lifestyle behaviors.

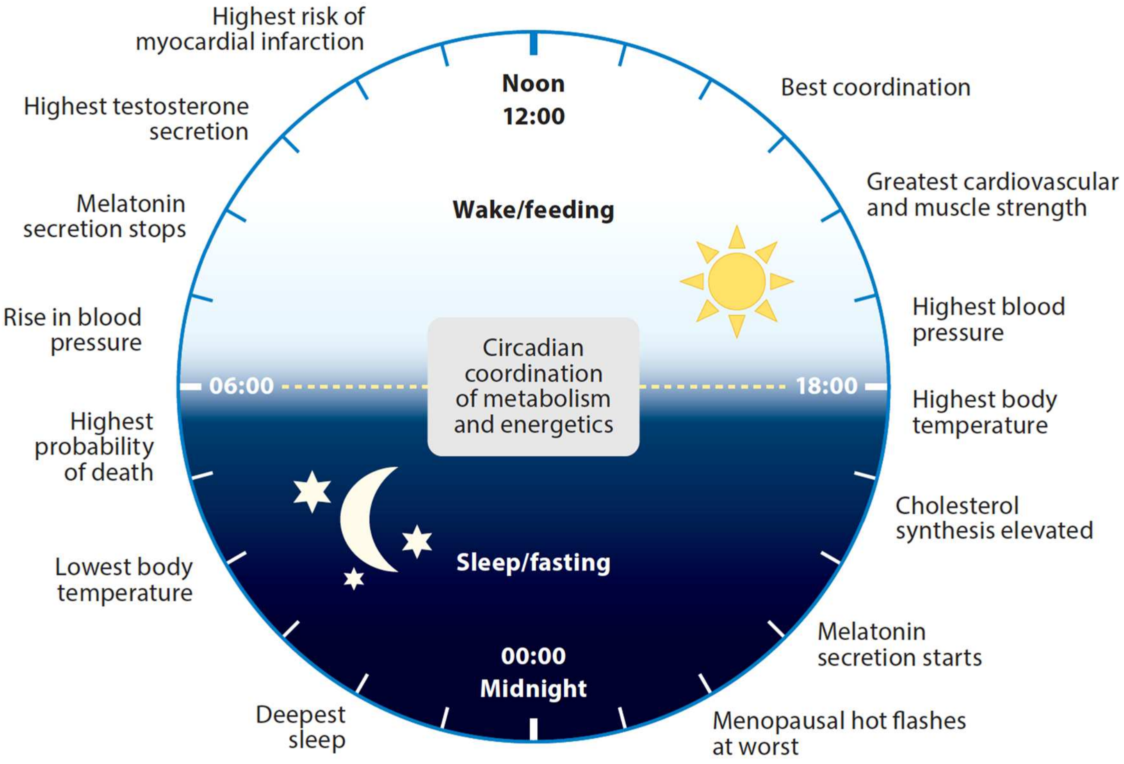

**Figure 7.4:** Circadian regulation of behaviors, hormones, physiology, metabolism, and energetics. Adapted from Patterson et al. [24].

ROIs for HP [2-$^{13}$C]pyruvate sleep studies may include the cerebellum (brain stem), basal ganglia (corpus callosum) and corona radiata (cortical gray matter or deep NAWM)[27]. If relatively high $k_{PG}$ in the brain stem is observed, it may indicate a greater sleep stage differential with a volunteer more likely to report dreams. Machine learning simulations with hyperparameters from self-reported data may motivate healthy and deductive sleep pattern recognition. Experimental controls may be thought at risk in the sense a subject can possibly be affected or features a strong resemblance, however a natural perception of creative experimentation is to dismiss prior notions and explore new ideas.

Metabolic imaging quantitatively measures how a human body converts, transports, and uses molecules for energy, with appetite and diet embroiled as significant and diverse inputs. The burgeoning research in food and nutritional science including fasting benefits future metabolic imaging studies as overall directedness toward improved, healthier lifestyles increases with investigations in sleep and relations for mental health.

# References

[1] Han S, Liu Y, Cai SJ, et al. IDH mutation in glioma: molecular mechanisms and potential therapeutic targets. Br J Cancer. 2020;122(11):1580-1589. doi:10.1038/s41416-020-0814-x.

[2] Autry AW, Gordon JW, et al. Characterization of serial hyperpolarized 13C metabolic imaging in patients with glioma. Neuroimage Clin. 2020;27:102323. doi:10.1016/j.nicl.2020.102323.

[3] Grassian AR, Parker SJ, Davidson SM, et al. IDH1 mutations alter citric acid cycle metabolism and increase dependence on oxidative mitochondrial metabolism. Cancer Res. 2014;74(12):3317-3331. doi:10.1158/0008-5472.CAN-14-0772-T.

[4] Merritt K, Egerton A, Kempton MJ, Taylor MJ, McGuire PK. Nature of Glutamate Alterations in Schizophrenia: A Meta-analysis of Proton Magnetic Resonance Spectroscopy Studies. JAMA Psychiatry. 2016;73(7):665-674. doi:10.1001/jamapsychiatry.2016.0442.

[5] Bubber P, Hartounian V, Gibson GE, Blass JP. Abnormalities in the tricarboxylic acid (TCA) cycle in the brains of schizophrenia patients. Eur Neuropsychopharmacol. 2011;21(3):254-260. doi:10.1016/j.euroneuro.2010.10.007.

[6] Cardno AG, Owen MJ. Genetic relationships between schizophrenia, bipolar disorder, and schizoaffective disorder. Schizophr Bull. 2014;40(3):504-515. doi:10.1093/schbul/sbu016.

[7] Ashok AH, Marques TR, Jauhar S, et al. The dopamine hypothesis of bipolar affective disorder: the state of the art and implications for treatment. Mol Psychiatry. 2017;22(5):666-679. doi:10.1038/mp.2017.16.

[8] Procaccini C, Santopaolo M, Faicchia D, et al. Role of metabolism in neurodegenerative disorders. Metabolism. 2016;65(9):1376-1390. doi:10.1016/j.metabol.2016.05.018.

[9] Shen J, Tomar JS. Elevated Brain Glutamate Levels in Bipolar Disorder and Pyruvate Carboxylase-Mediated Anaplerosis. Front Psychiatry. 2021;12:640977. Published 2021 Feb 23. doi:10.3389/fpsyt.2021.640977.

[10] Le Page LM, Guglielmetti C, Taglang C, Chaumeil MM. Imaging Brain Metabolism Using Hyperpolarized 13C Magnetic Resonance Spectroscopy. Trends Neurosci. 2020;43(5):343-354. doi:10.1016/j.tins.2020.03.006.

[11] Sterzer P, Adams RA, Fletcher P, et al. The Predictive Coding Account of Psychosis. Biol Psychiatry. 2018;84(9):634-643. doi:10.1016/j.biopsych.2018.05.015.

[12] Gupta S, Roy A, Dwarakanath BS. Metabolic Cooperation and Competition in the Tumor Microenvironment: Implications for Therapy. Front Oncol. 2017;7:68. Published 2017 Apr 12. doi:10.3389/fonc.2017.00068.

[13] Camandola S, Mattson MP. Brain metabolism in health, aging, and neurodegeneration. EMBO J. 2017;36(11):1474-1492. doi:10.15252/embj.201695810.

[14] DiNuzzo M, Nedergaard M. Brain energetics during the sleep-wake cycle. Curr Opin Neurobiol. 2017;47:65-72. doi:10.1016/j.conb.2017.09.010.

[15] Marjańska M, Shestov AA, Deelchand DK, Kittelson E, Henry PG. Brain metabolism under different anesthetic conditions using hyperpolarized [1-13 C]pyruvate and [2-13 C]pyruvate. NMR Biomed. 2018;31(12):e4012. doi:10.1002/nbm.4012.

[16] DiNuzzo M, Nedergaard M. Brain energetics during the sleep-wake cycle. Curr Opin Neurobiol. 2017;47:65-72. doi:10.1016/j.conb.2017.09.010.

[17] Tasali E, Leproult R, Ehrmann DA, Van Cauter E. Slow-wave sleep and the risk of type 2 diabetes in humans. Proc Natl Acad Sci U S A. 2008;105(3):1044-1049. doi:10.1073/pnas.0706446105.

[18] Huang YS, Liu FY, Lin CY, Hsiao IT, Guilleminault C. Brain imaging and cognition in young narcoleptic patients. Sleep Med. 2016;24:137-144. doi:10.1016/j.sleep.2015.11.023.

[19] Rempe MJ, Wisor JP. Cerebral lactate dynamics across sleep/wake cycles. Front Comput Neurosci. 2015;8:174. Published 2015 Jan 14. doi:10.3389/fncom.2014.00174.

[20] Briggs C, Hirasawa M, Semba K. Sleep Deprivation Distinctly Alters Glutamate Transporter 1 Apposition and Excitatory Transmission to Orexin and MCH Neurons. J Neurosci. 2018;38(10):2505-2518. doi:10.1523/JNEUROSCI.2179-17.2018.

[21] Bellesi M, de Vivo L, Chini M, Gilli F, Tononi G, Cirelli C. Sleep Loss Promotes Astrocytic Phagocytosis and Microglial Activation in Mouse Cerebral Cortex. J Neurosci. 2017;37(21):5263-5273. doi:10.1523/JNEUROSCI.3981-16.2017.

[22] Wang Y, Wu Y, Li T, Wang X, Zhu C. Iron Metabolism and Brain Development in Premature Infants. Front Physiol. 2019;10:463. Published 2019 Apr 25. doi:10.3389/fphys.2019.00463.

[23] Thompson RA, Nelson CA. Developmental science and the media. Early brain development. Am Psychol. 2001;56(1):5-15. doi:10.1037/0003-066x.56.1.5.

[24] Patterson RE, Sears DD. Metabolic Effects of Intermittent Fasting. Annu Rev Nutr. 2017;37:371-393. doi:10.1146/annurev-nutr-071816-064634.

[25] Hider RC, Kong X. Iron: effect of overload and deficiency. Met Ions Life Sci. 2013;13:229-294. doi:10.1007/978-94-007-7500-8_8.

[26] Georgieff MK, Innis SM. Controversial nutrients that potentially affect preterm neurodevelopment: essential fatty acids and iron. Pediatr Res. 2005;57(5 Pt 2):99R-103R. doi:10.1203/01.PDR.0000160542.69840.0F.

[27] Godlewska BR, Masaki C, Sharpley AL, Cowen PJ, Emir UE. Brain glutamate in medication-free depressed patients: a proton MRS study at 7 Tesla. Psychol Med. 2018;48(10):1731-1737. doi:10.1017/S0033291717003373.

[28] Sadock BJ, Sadock VA, Ruiz P. Kaplan & Sadock's synopsis of psychiatry: Behavioral sciences/clinical psychiatry (Eleventh edition.). Wolters Kluwer, Philadelphia, 2019.

[29] Mitelman SA, Canfield EL, Chu KW, et al. Poor outcome in chronic schizophrenia is associated with progressive loss of volume of the putamen. Schizophr Res. 2009;113(2-3):241-245. doi:10.1016/j.schres.2009.06.022.

[30] McCutcheon RA, Krystal JH, Howes OD. Dopamine and glutamate in schizophrenia: biology, symptoms and treatment. World Psychiatry. 2020;19(1):15-33. doi:10.1002/wps.20693.

## Publishing Agreement

It is the policy of the University to encourage open access and broad distribution of all theses, dissertations, and manuscripts. The Graduate Division will facilitate the distribution of UCSF theses, dissertations, and manuscripts to the UCSF Library for open access and distribution. UCSF will make such theses, dissertations, and manuscripts accessible to the public and will take reasonable steps to preserve these works in perpetuity.

I hereby grant the non-exclusive, perpetual right to The Regents of the University of California to reproduce, publicly display, distribute, preserve, and publish copies of my thesis, dissertation, or manuscript in any form or media, now existing or later derived, including access online for teaching, research, and public service purposes.

DocuSigned by:
4E927E6DEAE641A...
Author Signature

12/15/2021
Date